Dissertations, Master's Theses and Master's Reports

2021

Superresolution Enhancement with Active Convolved Illumination

Anindya Ghoshroy
Michigan Technological University, aghoshro@mtu.edu

SUPERRESOLUTION ENHANCEMENT WITH ACTIVE CONVOLVED

ILLUMINATION

By

Anindya Ghoshroy

A DISSERTATION

Submitted in partial fulfillment of the requirements for the degree of

DOCTOR OF PHILOSOPHY

In Electrical Engineering

MICHIGAN TECHNOLOGICAL UNIVERSITY

2021

This dissertation has been approved in partial fulfillment of the requirements for the Degree of DOCTOR OF PHILOSOPHY in Electrical Engineering.

Department of Electrical and Computer Engineering

Dissertation Advisor: *Dr. Durdu Guney*

Committee Member: *Dr. Jeremy Bos*

Committee Member: *Dr. Zhaohui Wang*

Committee Member: *Dr. Miguel Levy*

Department Chair: *Dr. Glen Archer*

Dedication

To my parents

for their love, guidance, and wisdom.

Contents

Preface

The main content of this dissertation comprises of the five published journal articles in Chapters 2-6. Additionally, one section of a review article containing a rich summary of the problem statement has been reproduced in Chapter 1. The necessary permissions required to reproduce these articles have been obtained from each publisher. All correspondence including letters of permission are in Appendix A.

The main contribution of the author to the overall research and body of knowledge are:

1. The theoretical formulation and associated simulations of a loss compensation and resolution enhancement technique for coherent, near-field, superresolution imaging systems.

2. The physical implementation and verification of the proposed technique with hyperbolic metamaterials and lossy Plasmonic superlenses.

3. The extensive mathematical derivation of the working principles and physics of the technique with the greater scope of developing a noise-resistant imaging theory, applicable to diverse problems in various fields pertaining to noisy linear systems.

4. Identifying and exploring the possibility of extending the resolution enhancement technique in fields such as terahertz time domain spectroscopy, imaging through atmospheric turbulence and high-resolution biomedical imaging.

5. Assistance during the experimental demonstration of the above concept with incoherent light and fabrication of a micro-coil wire hyperbolic metamaterial for a future experiment with coherent light.

The individual contributions for each chapter are as follows:

[1] Chapter 2: A. Ghoshroy formulated the theory, performed numerical modeling and developed the data analysis code for the primary results presented in the paper. A. Ghoshroy wrote the paper, W. Adams, X. Zhang and D. Guney provided technical comments and D. Guney edited the manuscript.

[2] Chapter 3: A. Ghoshroy designed the metamaterial system, performed numerical modeling and developed the data analysis code for the primary results presented in the paper. A. Ghoshroy wrote the paper, W. Adams, X. Zhang and D. Guney provided technical comments and D. Guney edited the manuscript.

---

[1]A. Ghoshroy, W. Adams, X. Zhang, and D. O. Guney, "Active plasmon injection scheme for subdiffraction imaging with imperfect negative index flat lens," J. Opt. Soc. Am. B **34**, 1478 (2017).
[2]A. Ghoshroy, W. Adams, X. Zhang, and D. Guney, "Hyperbolic metamaterial as a tunable near-field spatial filter to implement active plasmon-injection loss compensation," Phys. Rev. App. **10**, 024018 (2018).

[3]Chapter 4: A. Ghoshroy performed the numerical modeling and data analysis to obtain the main results in the paper. A. Ghoshroy organized and wrote the paper,. W. Adams, X. Zhang, and D. Guney provided technical comments and D. Guney edited the manuscript.

[4]Chapter 5: A. Ghoshroy and D. Guney developed the mathematical model and theory and core derivations. A. Ghoshroy wrote the data analysis code to obtain the main results in the paper. A. Ghoshroy organized and wrote the paper. W. Adams and D. Güney provided technical comments. D. Guney edited the manuscript.

[5] Chapter 6: A. Ghoshroy, and D. Guney formulated and researched extensions of the core concepts to other domains. A. Ghoshroy and D. Guney organized and wrote the paper. W. Adams provided technical comments.

---

[3]A. Ghoshroy, W. Adams, X. Zhang, and D. Guney, "Enhanced superlens imaging with loss-compensating hyperbolic near-field spatial filter," Opt. Lett. **43**, 1810 (2018).
[4]A. Ghoshroy, W. Adams, and D. Guney, "Theory of coherent active convolved illumination for superresolution enhancement," J. Opt. Soc. Am. B **37**, 2452 (2020).
[5]A. Ghoshroy, W. Adams, and D. Guney, "Super-resolution enhancement with active convolved illumination and correlations," SPIE **11081**, 1108128 (2020).

Acknowledgments

Finishing a PhD was quite a challenge but at the same time, infinitely more rewarding than I could have ever imagined. None of the experiences I have had over the past five years would have been possible without my advisor Dr. Durdu O. Guney, and I am eternally grateful to him for supporting me throughout the last five years. I have had the opportunity of engaging in countless insightful discussions about our research. I sincerely thank him for all the time he invested on me throughout the duration of my studies and the wisdom he has shared. His display of enthusiasm and energy in the relentless pursuit of scientific research has definitely influenced me in more ways than I can articulate and I hope that I may be able to command an audience and conduct research with the same standards someday.

I would also like to acknowledge the past and current members of Dr. Guney's research group for their exemplary enthusiasm and natural curiosity in their commitment to academic research. A sincere acknowledgement is reserved for Dr. Wyatt Adams, Dr. Xu Zhang and James Davis with whom I have not only spent countless hours brainstorming but also in fruitful discussions, commentary and critique. I would also like to thank the Office of Naval Research (N00014-15-1-2684) for sponsoring my research throughout the duration of my studies.

I would like to thank Dr. Jeremy Bos, Dr. Zhaohui Wang, and Dr. Miguel Levy for agreeing to serve on my dissertation committee and for their valuable feedback throughout my studies. Additionally I wish to thank all the faculty at Michigan Tech who have assisted me with their invaluable expertise throughout my courses. Special thanks is reserved for Dr. George Semouchkin, Dr. Elena Semouchkina for their invaluable guidance during my first few semesters as a graduate student. I also owe a deep debt of gratitude to my family for their unconditional love and care and I sincerely thank them for all the advice and support.

This dissertation and my achievements in academic research can be easily described as the grandest outcome of my life thus far. I would like to conclude by thanking everyone here at Michigan Tech and specially Graduate School, firstly for enrolling me into their community of graduate students and secondly for the amazing support system they have implemented, without which this dissertation would certainly not be possible.

Abstract

The first two decades of the 21st century witnessed the emergence of "metamaterials". The prospect of unrestricted control over light-matter interactions was a major contributing factor leading to the realization of new technologies and advancement of existing ones. While the field certainly does not lack innovative applications, widespread commercial deployment may still be several decades away. Fabrication of sophisticated 3d micro and nano structures, specially for telecommunications and optical frequencies will require a significant advancement of current technologies. More importantly, the effects of absorption and scattering losses will require a robust solution since this renders any conceivable application of metamaterials impracticable.

In this dissertation, a new approach, called Active Convolved Illumination (ACI), is formulated to address the problem of optical losses in metamaterials and plasmonics. An active implementation of ACI's predecessor the Π scheme formulated to provide compensation for arbitrary spatial frequencies. The concept of "selective amplification" of spatial frequencies is introduced as a method of providing signal amplification with suppressed noise amplification. Pendry's non-ideal negative index flat lens is intentionally chosen as an example of a stringent and conservative test candidate.

A physical implementation of ACI is presented with a plasmonic imaging system. The superlens integrated with a tunable near-field spatial filter designed with a layered metal-dielectric system exhibiting hyperbolic dispersion. A study of the physical generation of the auxiliary shows how selective amplification via convolution, is implemented by a lossy metamaterial functioning as a near-field spatial filter. Additionally the preservation of the mathematical formalism of ACI is presented by integrating the hyperbolic metamaterial with the previously used plasmonic imaging system.

A comprehensive mathematical exposition of ACI is developed for coherent light. This provides a rigorous understanding of the role of selective spectral amplification and correlations during the loss compensation process. The spectral variance of noise is derived to prove how an auxiliary source, which is firstly correlated with the object field, secondly is defined over a finite spectral bandwidth and thirdly, provides amplification over the selected bandwidth can significantly improve the spectral signal-to-noise ratio and consequently the resolution limit of a generic lossy plasmonic superlens.

Chapter 1

Introduction

1.1 An era of metamaterials

In the year 1959, Richard Feynman gave a lecture at the annual American Physical
Society meeting at Caltech. Inspired by developments in synthetic chemistry at the
time, Feynman considered the possibility of direct manipulation of the structural
composition of matter on an atomic or molecular level. He envisioned a dramatic
expansion of the range of obtainable properties which could be obtained with natural
materials at the time [1]. Feynman's speech predated important discoveries such
as the scanning tunneling microscope and it failed to inspire the greater scientific
community at the time. Interestingly, the paradigm of metamaterials, now considered

one of the most active areas of modern physics would not become fashionable for almost fifty years.

The science of metamaterials deals with engineering material properties on demand. In principle, a material's electromagnetic, thermodynamic or acoustic properties can be engineered by carefully controlling various subwavelength structural parameters, composition and other degrees of freedom including, but is not limited to, geometry, arrangement and alignment of resonations or inclusions, shape, size, density and periodicity of constituent elements. Therefore, metamaterials can be thought of as a platform enabling the realization of countless devices and technologies, beyond what nature can offer very much like the vision Feynman had conceived in 1959. Since the onset of the twenty-first century, when the term metamaterial was first conceived, an unprecedented series of milestones were made in a stunningly short span of time [2, 3]. Metamaterials have also impacted fundamental physics by fostering the observation of new physical phenomena such as the experimental discovery of toroidal dipole response in electrodynamics and the observation of the anapole [4].

However, the promise of such limitless possibilities came with a sizable share of challenges and despite the remarkable successes and milestones spanning almost two decades of research, widespread deployment of metamaterials in commercial and industrial environments is still lacking. Several challenges such as design and fabrication for telecommunications or visible wavelengths, fully three-dimensional unit cells

to approach the bulk 3D limit and mitigation of losses require robust solutions before metamaterials can transition from a scientific finding to a real-world usable material. However, these challenges should not discourage popular interest in the subject since the field is still somewhat young. For example, the industrial deployment of optical fibers and the growth of the optical telecommunications industry in the late 1970s was spurred after Bell Laboratories developed a vapor deposition process to mass-produce a low-loss optical fiber, almost 60 years after Henry Round at Marconi Labs and Oleg Vladimirovich Losev independently discovered the phenomenon of light emission from a semiconductors in the 1920s.

1.2   Problem Statement and Goals[1]

The problem of overcoming optical losses in metamaterials and plasmonics is perhaps the greatest fundamental challenge, rendering many of the proposed applications not viable in real world scenarios. Progress towards the development of a robust solution has been sluggish even after nearly two decades of efforts. Soukoulis and Wegener noted the gravity of this problem and the desired improvement any potential solution must hope to achieve, especially at optical frequencies [5]. Meanwhile, multiple strategies were proposed including gain medium [6], optical parametric amplification

---

[1]Reprinted from A. Ghoshroy, Ş. K. Özdemir and D. Guney, "Loss compensation in metamaterials and plasmonics with virtual gain [Invited]," *Opt. Mater. Express* 10, 1862 (2020); with permission from ©The Optical Society.

[7], geometric tailoring and optimization [8], and metasurfaces [9]. Although not eliminated completely, with many new devices metasurface approach substantially minimized the attenuation suffered by bulk metamaterials. Alternative low-loss materials such as high-index dielectrics, nitrides [10], oxides [11], and two-dimensional (2D) materials such as graphene, hexagonal boron nitride (h-BN) [12, 13], and their 2D analogue transition metal dichalcogenides (TMDCs) [14] have been considered as potential replacements for metals.

The early years of metamaterial research were primarily centered around sub-wavelength metallic resonators. However, the desired strong field enhancement and confinement resulting from the metallic free electron response is accompanied by non-radiative Ohmic losses. Geometric tailoring and optimization [8] of the underlying current distribution within the resonator permits limited reduction of losses.

Replacement of metallic resonators with high-index dielectric resonators exhibiting Mie resonances [15] in silicon [16], germanium, gallium phosphide, and certain per-ovskites has been considered to be a promising route for overcoming losses [17]. Dielectric resonators with strong displacement currents from bound electron oscillations are free from Ohmic losses. This enables low-loss non-plasmonic metamaterials [18, 19] and metasurfaces [20] having a plethora of exotic optical properties and light-matter interactions [21] including linear [22] and nonlinear [23, 24] effects. Loss-free negative index dielectric metamaterial was demonstrated at microwaves based on resonant

4

forward scattering [25]. However, this was achieved only for radiative losses using lossless dielectrics. Material losses have been shown to increase at larger operation frequencies, and available maximum range of refractive index is limited [17]. The latter renders dielectric resonators diffraction limited with moderate local field enhancement and makes it unsuitable for applications requiring small-mode volumes and large electric field enhancements, such as surface enhanced Raman spectroscopy [26] and deep sub-wavelength miniaturization [27]. Hydrogenated amorphous silicon (a-Si:H) appears as a relatively good candidate as a low-loss dielectric material for visible spectrum [28]. A difficulty often encountered in the visible spectrum is the fabrication of high aspect ratio dielectric resonators for phase control applications [20, 29, 30, 31]. This difficulty arises from two competing processes: Minimizing losses in the visible requires the use of larger bandgap materials. However, materials with larger bandgap have smaller refractive index for the same wavelength, significantly limiting the field confinement. In short, the fundamental problem of simultaneous suppression of material losses while preserving field enhancement remains elusive across the electromagnetic spectrum [26].

The use of gain materials involving pumped semiconductor quantum dots and dye molecules in epoxy resins was also originally thought as a promising strategy for active compensation of losses [6]. However, problems with the pump requirement, stability, gain saturation [32], intense noise generation near the field enhancement regions [33, 34, 35], causality [34, 35], and maintenance [32] have posed stringent

5

constraints and raised fundamental questions about the viability of this approach.

In recent years, graphene, h-BN, 2D TMDCs, and layered oxides have fostered significant interest towards low loss optoelectronics and nanophotonics. 2D TMDCs [36] are nanomaterials with a single plane of transition metal atoms (such as Mo, W, Ta etc.) sandwiched (X-M-X) between two planes of chalcogen atoms (such as Se, S, Te, etc.). Individual atomic planes are ambitiously used as building blocks for artificially stacked materials to obtain the desired combined functionality [36]. The sandwich structure provides unique opportunities to directly control material properties by inserting guest species at the van der Waals gap through intercalation [37]. Recently, the possibility of extremely low optical losses with TaS_2 was shown and 2D TDMC-halide structures with engineered band structures and density of states were proposed as alternative plasmonic materials with greatly suppressed intrinsic losses [14]. Similarly, plasmonic and phonon-polaritonic properties exhibiting very low optical losses have been demonstrated [12, 13, 38] for h-BN. However, problems associated with thermodynamic stability, control of surface construction with low defect densities, charge transfers, and built-in electric fields in heterostructures impose cumbersome fabrication and design challenges for 2D materials [39]. Additionally, continuous or pulsed laser induced thermal or non-thermal damage to the crystal structure is a serious concern [39]. Energetic phonons, hot electrons due to electron-electron and electron-phonon interactions have been shown to damage the crystal structure through ionization and Coulombic explosion process [40, 41]. Laser

induced damage strongly depends on the underlying defect density [39]. High quality atomic layers fabricated with chemical vapor deposition have higher damage thresholds than other processes such as liquid-phase exfoliation due to their relatively low defect densities [42, 43, 44].

It is also worth mentioning the numerous attempts made to find alternative low-loss plasmonic materials especially in the optical regime. Candidates such as alkali-noble intermetallics [45, 46], and transition metal nitrides [10], doped semiconductors and transparent conducting oxides [47] were proposed for infrared and optical frequencies. However, the performance of these materials is still lower than that of the noble metal counterparts.

Fortunately, finding the elusive "metal" [48] with losses several orders of magnitude less than naturally occurring noble metals is not the only hope for transitioning plasmonics and metamaterials into a practical field from a purely research enterprise. From a perspective of light-matter interactions, the above research enterprises can be broadly classified under the engineering of "matter" based solutions to obtain a more favorable interaction with incident light compared to naturally occurring noble metals. The research presented in this dissertation considers the prospect of engineering a "light" based solution to mitigate the effects of a lossy interaction with the metamaterial. In principle, the concept has some commonalities with more recent efforts on "virtual gain" particularly in the compensation of losses in metamaterials

and plasmonics. Virtual gain, here, is fundamentally different than traditional approaches and is defined as the result of an amplification in a medium acquired with no intrinsic gain mechanism (i.e., optical gain from parametric, nonlinear, luminescence, fluorescence, or emission processes is not involved). A very recent review on the latter can be found in [26]. The term was coined for the first time in [49] and has been adopted and expanded here with the hope of initiating discussions of alternative explorations in a broader context.

In 2015, Sadatgol et al. proposed employing an coherent optical amplification technique, called plasmon-injection (Π or PI) scheme, to amplify the field inside a lossy metamaterial through coherent superposition [50]. Coherent amplification, has been used to provide gain to mode-locked laser pulses inside a passive optical cavity through constructive interference with a secondary source [51, 52]. To the best of our knowledge, this was the first application of coherent amplification to loss compensation in metamaterials. The Π scheme uses an auxiliary source to amplify the domestic field in a lossy metamaterial giving the illusion of suppressed material losses with enhanced transmission. Theoretical implementations of the Π scheme with near-field imaging systems involving negative index materials (NIMs) [53], superlenses [54], and hyperlenses [55, 56] showed a resolution enhancement. Additionally, the auxiliary source was shown to emulate linear deconvolution [53].

This dissertation generalizes the Π scheme to the more encompassing active convolved

illumination (ACI) and brings the concept closer virtual gain, within the context of a loss compensation technique which is not simply restricted to plasmons. The distinctive features of ACI, such as selective spectral amplification and correlations, are developed along with a rigorous mathematical study for coherent light. A greater objective of this dissertation is twofold. Firstly, this dissertation develops a noise-resistant imaging theory and generalizes the use of ACI in a wide range of problems related to noisy linear systems, for example, those in atmospheric imaging [57, 58, 59, 60], time-domain spectroscopy [61, 62], optical communications [63, 64, 65, 66]. A second objective, which is briefly touched and is left as a potential future work, introduces the idea of active spectrum and correlation manipulation for applications involving $\mathcal{PT}$ symmetric non-Hermitian photonics [67, 68], and even quantum computing [60, 69, 70]. ACI has also been experimentally demonstrated for a far-field imaging system with incoherent light and a second complementary experimental demonstration for coherent light is also planned as a future work.

1.3   Summary of Research

Chapter 2 introduces the first active implementation of the Π scheme in the presence of noise with Pendry's non-ideal negative index flat lens adopted as a stringent test candidate. The concept of the auxiliary source is expanded beyond traditional deconvolution based inverse filtering methods. The keyword active emphasizes the use of

external physical energy even though linear transmission through passive materials is considered. The principal concept is that a physically convolved auxiliary source can restore weak signals while countering adverse noise amplification effects by selective amplification of high spatial frequency features deep within the subwavelength regime. The selective amplification approach also enables recovery of high spatial frequencies previously buried within the noise. Consequently, the resolution limit of the lossy metamaterial lens can be substantially extended thus enabling ultrahigh-resolution imaging. This chapter therefore establishes the theoretical formalism of the active compensation process and convolution is used as a means to correlate the auxiliary source to the original signal whose enhanced transmission is desired.

Chapter 3 presents a proof-of-principle physical implementation of the compensation scheme with an experimentally demonstrated plasmonic lens. A $50nm$ thick Ag film functioning as a lossy plasmonic lens at wavelength $\lambda = 365nm$ is selected since it is incapable of resolving subwavelength apertures separated by one-sixth of the illumination wavelength ($\lambda/6$). The apertures are assumed to be illuminated by a normally incident plane wave and the auxiliary source is generated by integrating a hyperbolic metamaterial, functioning as a near-field spatial filter, between the lens and the apertures. A high-intensity illumination above $1\ mW/\mu m^2$ is used to generate the desired auxiliary source and the restoration of previously undetectable Fourier components of the image spectrum with minor noise amplification is illustrated. Consequently, this allows the perfect reconstruction of three apertures separated by ($\lambda/6$) with the

10

integrated system which was previously not achievable by the plasmonic lens alone.

Chapter 4 presents a detailed discussion of the physical generation of the auxiliary source. A hyperbolic metamaterial (HMM), designed with a multilayered aluminium-dielectric structure, and functioning as a near-field spatial filter is used to present and verify the physical generation of a functioning auxiliary source. Selective amplification is implemented by carefully selecting the structural parameters of the layered system such that the HMM has a relatively high-transmission peak at a tunable center frequency and low transmission on either side. The layered structure is intentionally selected to exploit its shift invariance property. This ensures the physical implementation of a convolution operation necessary to correlate the auxiliary source to the original signal. With the aid of numerical simulations, this chapter presents the physical implementation of the mathematical abstractions developed in Chapter 2, where the idea of selective amplification with auxiliary source is first introduced. The idea of scaling selective amplification with the controlled amplitude of illumination is also presented and verified.

Chapter 5 formulates a comprehensive theoretical framework of ACI for coherent light. The underlying model specifically highlights the distinctive features of ACI and provides a rigorous mathematical analysis of the process. ACI's auxiliary source is designed with three essential characteristics. Firstly, it is correlated with the object field. Second, it is defined over a finite spectral bandwidth. Third, it is amplified

over that selected bandwidth. These features are achieved by an auxiliary source coherently superimposed with the object field. The noise variance in the Fourier domain is derived to prove that utilizing the auxiliary source with the above properties can significantly improve the spectral signal-to-noise ratio and resolution limit.

Chapter 6 presents potential implementations and extensions of ACI with various systems. Even though concept of ACI was first numerically demonstrated as a loss compensation method, it later rapidly evolved into a scheme for the mitigation of information loss in noisy and lossy linear systems. The ACI has since turned into a scheme for spectrum manipulation using selective amplification and correlations. Therefore, in chapter 6 a brief study of the potential implementation of ACI in imaging through scattering and random media, THz time domain spectroscopy, and quantum computing is considered. The factors which limit the performance of each system are briefly discussed followed by an argument on how the limits can be potentially extended using selective amplification with ACI.

References

[1] Richard P Feynman. There's plenty of room at the bottom. *California Institute of Technology, Engineering and Science magazine*, 1960.

[2] Nikolay I. Zheludev. The road ahead for metamaterials. *Science*, 328(5978):582–583, 2010.

[3] Nikolay I. Zheludev. Obtaining optical properties on demand. *Science*, 348(6238):973–974, 2015.

[4] Nikolay I Zheludev. Metamaterials at the university of southampton and beyond. *Journal of Optics*, 19(8):084009, 2017.

[5] Costas M Soukoulis and Martin Wegener. Past achievements and future challenges in the development of three-dimensional photonic metamaterials. *Nature Photonics*, 5(9):523–530, 2011.

[6] Shumin Xiao, Vladimir P Drachev, Alexander V Kildishev, Xingjie Ni, Uday K

Chettiar, Hsiao-Kuan Yuan, and Vladimir M Shalaev. Loss-free and active optical negative-index metamaterials. *Nature*, 466(7307):735–738, 2010.

[7] Alexander K Popov and Vladimir M Shalaev. Compensating losses in negative-index metamaterials by optical parametric amplification. *Optics Letters*, 31(14):2169–2171, 2006.

[8] Durdu Ö Güney, Thomas Koschny, and Costas M Soukoulis. Reducing ohmic losses in metamaterials by geometric tailoring. *Physical Review B*, 80(12):125129, 2009.

[9] Patrice Genevet, Federico Capasso, Francesco Aieta, Mohammadreza Khorasaninejad, and Robert Devlin. Recent advances in planar optics: from plasmonic to dielectric metasurfaces. *Optica*, 4(1):139–152, 2017.

[10] Gururaj V Naik, Jeremy L Schroeder, Xingjie Ni, Alexander V Kildishev, Timothy D Sands, and Alexandra Boltasseva. Titanium nitride as a plasmonic material for visible and near-infrared wavelengths. *Optical Materials Express*, 2(4):478–489, 2012.

[11] Gururaj V Naik, Jongbum Kim, and Alexandra Boltasseva. Oxides and nitrides as alternative plasmonic materials in the optical range. *Optical Materials Express*, 1(6):1090–1099, 2011.

[12] S Dai, Z Fei, Q Ma, AS Rodin, M Wagner, AS McLeod, MK Liu, W Gannett,

W Regan, K Watanabe, et al. Tunable phonon polaritons in atomically thin van der waals crystals of boron nitride. *Science*, 343(6175):1125–1129, 2014.

[13] Achim Woessner, Mark B Lundeberg, Yuanda Gao, Alessandro Principi, Pablo Alonso-González, Matteo Carrega, Kenji Watanabe, Takashi Taniguchi, Giovanni Vignale, Marco Polini, et al. Highly confined low-loss plasmons in graphene–boron nitride heterostructures. *Nature Materials*, 14(4):421–425, 2015.

[14] Morten N Gjerding, Mohnish Pandey, and Kristian S Thygesen. Band structure engineered layered metals for low-loss plasmonics. *Nature Communications*, 8(1):1–8, 2017.

[15] Qian Zhao, Ji Zhou, Fuli Zhang, and Didier Lippens. Mie resonance-based dielectric metamaterials. *Materials Today*, 12(12):60–69, 2009.

[16] Andrey B Evlyukhin, Carsten Reinhardt, Andreas Seidel, Boris S Luk'yanchuk, and Boris N Chichkov. Optical response features of si-nanoparticle arrays. *Physical Review B*, 82(4):045404, 2010.

[17] Denis G Baranov, Dmitry A Zuev, Sergey I Lepeshov, Oleg V Kotov, Alexander E Krasnok, Andrey B Evlyukhin, and Boris N Chichkov. All-dielectric nanophotonics: the quest for better materials and fabrication techniques. *Optica*, 4(7):814–825, 2017.

[18] Mark S Wheeler, J Stewart Aitchison, and Mohammad Mojahedi. Three-dimensional array of dielectric spheres with an isotropic negative permeability at infrared frequencies. *Physical Review B*, 72(19):193103, 2005.

[19] Jon A Schuller, Rashid Zia, Thomas Taubner, and Mark L Brongersma. Dielectric metamaterials based on electric and magnetic resonances of silicon carbide particles. *Physical Review Letters*, 99(10):107401, 2007.

[20] Amir Arbabi, Yu Horie, Mahmood Bagheri, and Andrei Faraon. Dielectric metasurfaces for complete control of phase and polarization with subwavelength spatial resolution and high transmission. *Nature Nanotechnology*, 10(11):937, 2015.

[21] RS Savelev, SV Makarov, AE Krasnok, and PA Belov. From optical magnetic resonance to dielectric nanophotonics (a review). *Optics and Spectroscopy*, 119(4):551–568, 2015.

[22] Yuan Hsing Fu, Arseniy I Kuznetsov, Andrey E Miroshnichenko, Ye Feng Yu, and Boris Luk'yanchuk. Directional visible light scattering by silicon nanoparticles. *Nature Communications*, 4(1):1–6, 2013.

[23] Maxim R Shcherbakov, Dragomir N Neshev, Ben Hopkins, Alexander S Shorokhov, Isabelle Staude, Elizaveta V Melik-Gaykazyan, Manuel Decker, Alexander A Ezhov, Andrey E Miroshnichenko, Igal Brener, et al. Enhanced third-harmonic generation in silicon nanoparticles driven by magnetic response. *Nano Letters*, 14(11):6488–6492, 2014.

[24] Denis G Baranov, Sergey V Makarov, Valentin A Milichko, Sergey I Kudryashov, Alexander E Krasnok, and Pavel A Belov. Nonlinear transient dynamics of photoexcited resonant silicon nanostructures. *Acs Photonics*, 3(9):1546–1551, 2016.

[25] SeokJae Yoo, Suyeon Lee, and Q-Han Park. Loss-free negative-index metamaterials using forward light scattering in dielectric meta-atoms. *ACS Photonics*, 5(4):1370–1374, 2018.

[26] Alex Krasnok and Andrea Alu. Active nanophotonics. *Proceedings of the IEEE*, 108(5):628–654, 2020.

[27] Xu Zhang, James E Davis, and Durdu Ö Güney. Ultra-thin metamaterial beam splitters. *Applied Sciences*, 10(1):53, 2020.

[28] Gwanho Yoon, Jaehyuck Jang, Jungho Mun, Ki Tae Nam, and Junsuk Rho. Metasurface zone plate for light manipulation in vectorial regime. *Communications Physics*, 2(1):1–8, 2019.

[29] Carsten Stock, Thomas Siefke, and Uwe Zeitner. Metasurface-based patterned wave plates for vis applications. *JOSA B*, 36(5):D97–D102, 2019.

[30] Robert C Devlin, Mohammadreza Khorasaninejad, Wei Ting Chen, Jaewon Oh, and Federico Capasso. Broadband high-efficiency dielectric metasurfaces for the visible spectrum. *Proceedings of the National Academy of Sciences*, 113(38):10473–10478, 2016.

[31] Tong Li, Xiaobin Hu, Huamin Chen, Chen Zhao, Yun Xu, Xin Wei, and Guofeng Song. Metallic metasurfaces for high efficient polarization conversion control in transmission mode. *Optics Express*, 25(20):23597–23604, 2017.

[32] Allan D Boardman, Volodymyr V Grimalsky, Yuri S Kivshar, Svetlana V Koshevaya, Mikhail Lapine, Natalia M Litchinitser, Vadim N Malnev, Mikhail Noginov, Yuriy G Rapoport, and Vladimir M Shalaev. Active and tunable metamaterials. *Laser & Photonics Reviews*, 5(2):287–307, 2011.

[33] Costas M Soukoulis and Martin Wegener. Optical metamaterials—more bulky and less lossy. *Science*, 330(6011):1633–1634, 2010.

[34] Mark I Stockman. Criterion for negative refraction with low optical losses from a fundamental principle of causality. *Physical Review Letters*, 98(17):177404, 2007.

[35] Paul Kinsler and MW McCall. Causality-based criteria for a negative refractive index must be used with care. *Physical review letters*, 101(16):167401, 2008.

[36] Andre K Geim and Irina V Grigorieva. Van der waals heterostructures. *Nature*, 499(7459):419–425, 2013.

[37] Judy J Cha, Kristie J Koski, Kevin CY Huang, Ken Xingze Wang, Weidong Luo, Desheng Kong, Zongfu Yu, Shanhui Fan, Mark L Brongersma, and Yi Cui. Two-dimensional chalcogenide nanoplates as tunable metamaterials via chemical intercalation. *Nano Letters*, 13(12):5913–5918, 2013.

[38] Alexander J Giles, Siyuan Dai, Igor Vurgaftman, Timothy Hoffman, Song Liu, Lucas Lindsay, Chase T Ellis, Nathanael Assefa, Ioannis Chatzakis, Thomas L Reinecke, et al. Ultralow-loss polaritons in isotopically pure boron nitride. *Nature Materials*, 17(2):134–139, 2018.

[39] Shaoliang Yu, Xiaoqin Wu, Yipei Wang, Xin Guo, and Limin Tong. 2d materials for optical modulation: challenges and opportunities. *Advanced Materials*, 29(14):1606128, 2017.

[40] M Lenner, A Kaplan, and RE Palmer. Nanoscopic coulomb explosion in ultrafast graphite ablation. *Applied Physics Letters*, 90(15):153119, 2007.

[41] Chen Cheng, Ruiyun He, Carolina Romero, Javier R Vázquez de Aldana, and Feng Chen. Spontaneous micro-modification of single-layer graphene induced by femtosecond laser irradiation. *Applied Physics Letters*, 111(24):241901, 2017.

[42] Zhipei Sun, Tawfique Hasan, Felice Torrisi, Daniel Popa, Giulia Privitera, Fengqiu Wang, Francesco Bonaccorso, Denis M Basko, and Andrea C Ferrari. Graphene mode-locked ultrafast laser. *ACS Nano*, 4(2):803–810, 2010.

[43] Han Zhang, Qiaoliang Bao, Dingyuan Tang, Luming Zhao, and Kianping Loh. Large energy soliton erbium-doped fiber laser with a graphene-polymer composite mode locker. *Applied Physics Letters*, 95(14):141103, 2009.

[44] Qiaoliang Bao, Han Zhang, Jia-xiang Yang, Shuai Wang, Ding Yuan Tang, Rajan

Jose, Seeram Ramakrishna, Chwee Teck Lim, and Kian Ping Loh. Graphene–polymer nanofiber membrane for ultrafast photonics. *Advanced Functional Materials*, 20(5):782–791, 2010.

[45] Matthew D Arnold and Martin G Blaber. Optical performance and metallic absorption in nanoplasmonic systems. *Optics Express*, 17(5):3835–3847, 2009.

[46] MG Blaber, MD Arnold, and MJ Ford. Designing materials for plasmonic systems: the alkali–noble intermetallics. *Journal of Physics: Condensed Matter*, 22(9):095501, 2010.

[47] Gururaj V Naik, Vladimir M Shalaev, and Alexandra Boltasseva. Alternative plasmonic materials: beyond gold and silver. *Advanced Materials*, 25(24):3264–3294, 2013.

[48] Jacob B Khurgin and Greg Sun. In search of the elusive lossless metal. *Applied Physics Letters*, 96(18):181102, 2010.

[49] Huanan Li, Ahmed Mekawy, Alex Krasnok, and Andrea Alù. Virtual parity-time symmetry. *Physical Review Letters*, 124(19):193901, 2020.

[50] Mehdi Sadatgol, Şahin K Özdemir, Lan Yang, and Durdu Ö Güney. Plasmon injection to compensate and control losses in negative index metamaterials. *Physical Review Letters*, 115(3):035502, 2015.

[51] R Jason Jones and Jun Ye. Femtosecond pulse amplification by coherent addition in a passive optical cavity. *Optics Letters*, 27(20):1848–1850, 2002.

[52] Eric O Potma, Conor Evans, X Sunney Xie, R Jason Jones, and Jun Ye. Picosecond-pulse amplification with an external passive optical cavity. *Optics Letters*, 28(19):1835–1837, 2003.

[53] Wyatt Adams, Mehdi Sadatgol, Xu Zhang, and Durdu Ö Güney. Bringing the 'perfect lens' into focus by near-perfect compensation of losses without gain media. *New Journal of Physics*, 18(12):125004, dec 2016.

[54] Wyatt Adams, Anindya Ghoshroy, and Durdu Ö Güney. Plasmonic superlens image reconstruction using intensity data and equivalence to structured light illumination for compensation of losses. *Journal of Optical Society of America B*, 34(10):2161–2168, 2017.

[55] Xu Zhang, Wyatt Adams, Mehdi Sadatgol, and Durdu Ö Güney. Enhancing the resolution of hyperlens by the compensation of losses without gain media. *Progress In Electromagnetics Research C*, 70:1–7, 2016.

[56] Xu Zhang, Wyatt Adams, and Durdu Ö Güney. Analytical description of inverse filter emulating the plasmon injection loss compensation scheme and implementation for ultrahigh-resolution hyperlens. *Journal of Optical Society of America B*, 34(6):1310–1318, 2017.

[57] Mohamed E Hanafy, Michael C Roggemann, and Durdu Ö Güney. Detailed

effects of scattering and absorption by haze and aerosols in the atmosphere on the average point spread function of an imaging system. *Journal of Optical Society of America A*, 31(6):1312–1319, 2014.

[58] Mohamed E Hanafy, Michael C Roggemann, and Durdu Ö Güney. Estimating the image spectrum signal-to-noise ratio for imaging through scattering media. *Optical Engineering*, 54(1):013102, 2015.

[59] Mohamed E Hanafy, Michael C Roggemann, and Durdu Ö Güney. Reconstruction of images degraded by aerosol scattering and measurement noise. *Optical Engineering*, 54(3):033101, 2015.

[60] Durdu Ö Güney, Wyatt Adams, and Anindya Ghoshroy. Super-resolution enhancement with active convolved illumination and correlations. In *Active Photonic Platforms XI*, volume 11081, page 1108128. International Society for Optics and Photonics, 2019.

[61] Hichem Guerboukha, Kathirvel Nallappan, and Maksim Skorobogatiy. Toward real-time terahertz imaging. *Advances in Optics and Photonics*, 10(4):843–938, 2018.

[62] Kiarash Ahi. A method and system for enhancing the resolution of terahertz imaging. *Measurement*, 138:614–619, 2019.

[63] Greg Gbur and Emil Wolf. Spreading of partially coherent beams in random media. *Journal of Optical Society of America A*, 19(8):1592–1598, 2002.

[64] Aristide Dogariu and Stefan Amarande. Propagation of partially coherent beams: turbulence-induced degradation. *Optics Letters*, 28(1):10–12, 2003.

[65] Greg Gbur. Partially coherent beam propagation in atmospheric turbulence. *Journal of Optical Society of America A*, 31(9):2038–2045, 2014.

[66] Milo W Hyde. Controlling the spatial coherence of an optical source using a spatial filter. *Applied Sciences*, 8(9):1465, 2018.

[67] Francesco Monticone, Constantinos A Valagiannopoulos, and Andrea Alù. Parity-time symmetric nonlocal metasurfaces: all-angle negative refraction and volumetric imaging. *Physical Review X*, 6(4):041018, 2016.

[68] Ramy El-Ganainy, Mercedeh Khajavikhan, Demetrios N Christodoulides, and Sahin K Ozdemir. The dawn of non-hermitian optics. *Communications Physics*, 2(1):1–5, 2019.

[69] Amor Gueddana, Peyman Gholami, and Vasudevan Lakshminarayanan. Can a universal quantum cloner be used to design an experimentally feasible near-deterministic cnot gate? *Quantum Information Processing*, 18(7):221, 2019.

[70] Amor Gueddana and Vasudevan Lakshminarayanan. Toward the universal quantum cloner limit for designing compact photonic cnot gate. *arXiv preprint arXiv:1906.06547*, 2019.

Chapter 2

Active plasmon injection scheme for subdiffraction imaging with imperfect negative index flat lens[1]

2.1 Introduction

Controlling the interaction of photons and electrons at the sub-wavelength electromagnetic regime has led to a wide variety of novel optical materials and applications in the territory of metamaterials and plasmonics relevant to computing, communications, defense, health, sensing, imaging, energy, and other technologies [1, 2, 3, 4, 5, 6, 7, 8, 9, 10, 11, 12, 13, 14, 15, 16, 17, 18, 19, 20, 21, 22, 23, 24, 25, 26, 27, 28, 29, 30, 31, 32, 33, 34, 35, 36, 37, 38]. The prospect of circumventing Rayleigh's diffraction limit, thereby allowing super-resolution imaging has regained tremendous ground since Pendry theorized that a slab of negative (refractive) index material (NIM) can amplify and focus evanescent fields which contain information about the sub-wavelength features of an object [39]. A recent review of super-resolution imaging in the context of metamaterials is given in [40].

However, a perfect NIM does not exist in nature and although recent developments in metamaterials have empowered their realization, a fundamental limitation exists. The presence of material losses in the near infrared and visible regions is significant [41, 42, 43]. This compromises the performance of the theoretical perfect lens [44, 45] since a significant portion of evanescent fields is below the noise floor of the detector and is indiscernible. Therefore, new efforts were directed towards the compensation of losses in metamaterials [46, 47, 48]. Among the schemes that were developed, gain

media to compensate intrinsic losses gained popularity [49, 50]. However, Stockman [51] demonstrated that the use of gain media involved a fundamental limitation. Using the Kramers-Kronig relations, they developed a rule based on causality which makes loss compensation with gain media difficult to realize.

Recently, a new compensation scheme, called plasmon injection or Π scheme [52], was proposed. The Π scheme was conceptualized with surface plasmon driven NIMs [53] and achieves loss compensation by coherently superimposing externally injected surface plasmon polaritons (SPPs) with local SPPs. Therefore, absorption losses in the NIM could be removed without a gain medium or non-linear effects. Although the Π scheme was originally envisioned for plasmonic metamaterials [52, 54, 55], the idea is general and can be applied to any type of optical modes. In [56] Adams, et. al used a post processing technique equivalent to this method. They demonstrated that the process can indeed be used to amplify the attenuated Fourier components and thereby accurately resolve an object with sub-wavelength features.

Although this form of passive inverse filter provides compensation for absorption losses, it is also prone to noise amplification [56]. This is illustrated in figure 2.1 which shows an object with three Gaussian features separated by $\lambda_o/4$, where λ_o is the free space wavelength. Noise is prominent in the Fourier spectra beyond $\frac{k_y}{k_o} = 2.5$ as seen in figure 2.2. However, the compensated image is still reasonably well resolved. Consider now the object shown in figure 2.3, which has four Gaussians separated by
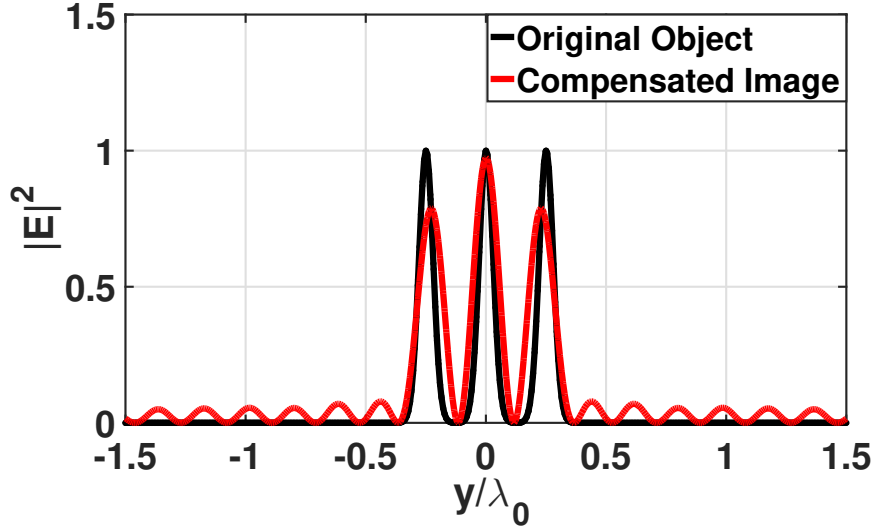
Figure 2.1: Electric field magnitude squared $[Vm^{-1}]^2$ distribution in the object and image planes for an object with features separated by $\lambda_o/4$ with $\lambda_o = 1\mu m$. The compensated image is reasonably well resolved with the equivalent inverse filter post-processing technique.

Figure 2.2: Fourier spectra $[Vm^{-1}]$ of the three Gaussians and the compensated image in figure 2.1, and the raw image obtained without loss compensation. The compensation filter is the inverse of the transfer function. The compensated image spectrum is obtained simply by multiplying the raw image spectrum with the compensation filter. Notice that the noise can be seen for high spatial frequencies which is amplified by the compensation.
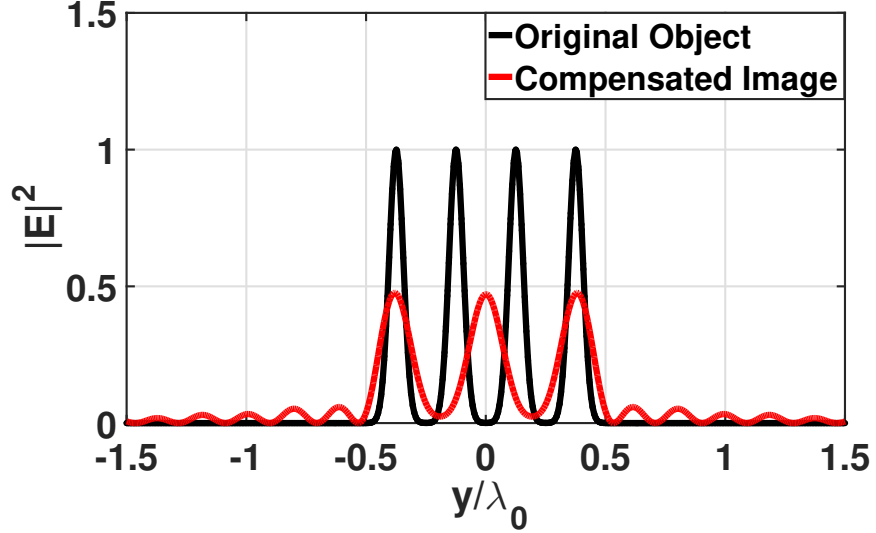
Figure 2.3: Electric field magnitude squared $[Vm^{-1}]^2$ for the four Gaussians, in the object and image planes, separated by $\lambda_o/4$ with $\lambda_o = 1\mu m$. The compensated image is very poorly resolved with one of the Gaussians missing.

$\lambda_o/4$. The Fourier spectra of the raw image, shown in figure 2.4, demonstrates how the feature at $\frac{k_y}{k_o} = 2$ is not distinguishable under the noise. The final compensated image, when subject to the same compensation scheme, is poorly resolved. We define a ***feature*** as any spatial Fourier component that has substantial contribution to the shape of the object. It is clear that the Fourier components beyond $\frac{k_y}{k_o} = 2$ have a significant contribution to the four Gaussians and must be recovered from the image spectrum in order to accurately resolve the object. Therefore, noise presents a limitation which must be overcome to make the Π scheme versatile.

In the present work, we demonstrate how the Π scheme can be significantly improved with the use of a physical auxiliary source to recover high spatial frequency features that are buried under the noise. We show that by using a convolved auxiliary source
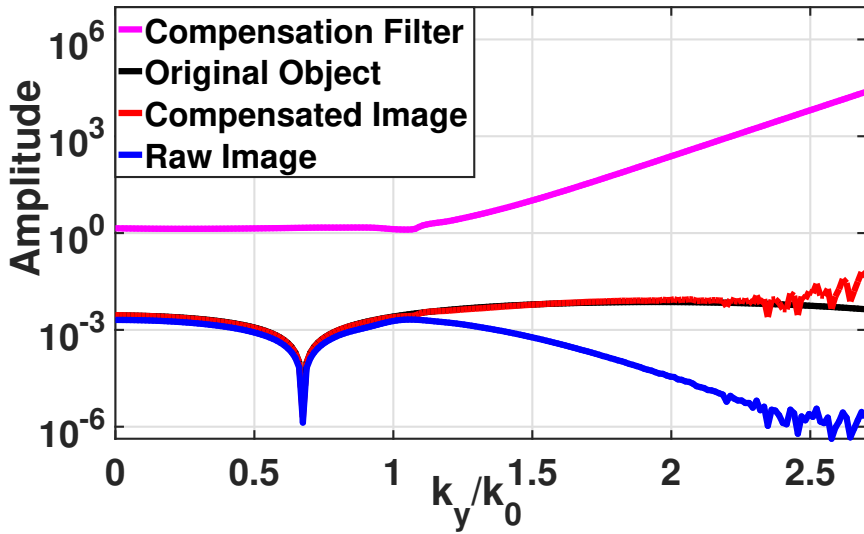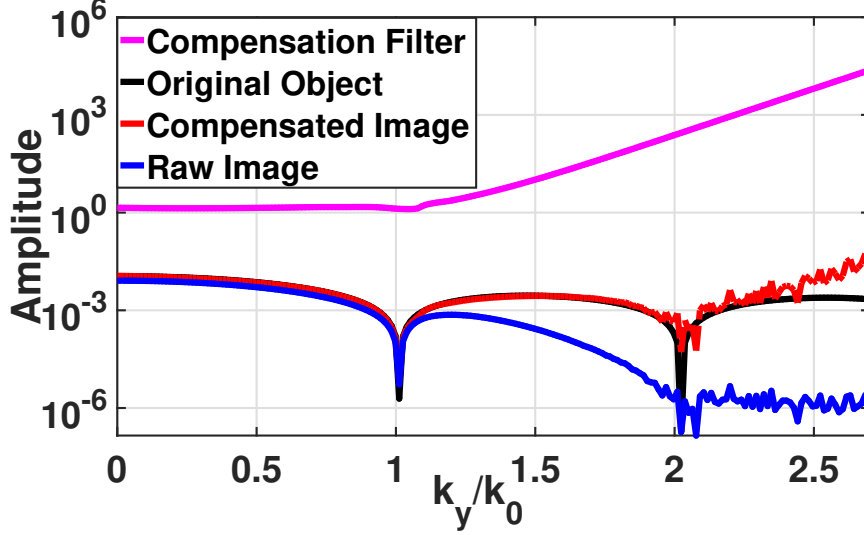
Figure 2.4: Fourier spectra $[Vm^{-1}]$ of the four Gaussians and the compensated image in figure 2.3, and the raw image along with the compensation filter. Notice that the feature at $\frac{k_y}{k_o} = 2$ is not discernable under the noise and cannot be recovered well with the compensation.

we can amplify the object spectrum in the frequency domain. The amplification makes the Fourier components that are buried in the noise distinguishable. This allows for the recovery of the previously inaccessible object features by adjusting the amount of compensation from the Π scheme.

The technique presented in this paper is based on the same negative index flat lens (NIFL) as in [56]. We use the words **"passive"** and **"active"** to distinguish between the compensation schemes applied in [56] and in this work, respectively. Therefore, the inverse filter post processing used in [56] and figures 2.1-2.4 to emulate the physical compensation of losses can be called passive Π scheme, since no external physical auxiliary is actively involved as opposed to the active Π scheme here, where the direct physical implementation using an external auxiliary source as originally envisioned in

[52] is sought. The active compensation scheme allows us to control noise amplifica-
tion and hence extend the applicability of the Π scheme to higher spatial frequencies.

2.2 Theory

We define the optical properties of the NIFL with the relative permittivity and per-
meability expressed as $\epsilon_r = \epsilon' + i\epsilon''$ and $\mu_r = \mu' + i\mu''$, where $\epsilon' = -1$ and $\mu' = -1$.
COMSOL Multiphysics, the finite element method based software package that we
use here, assumes $exp(j\omega t)$ time dependence. Therefore, the imaginary parts of ϵ_r
and μ_r are negative for passive media. In this paper we have used 0.1 as the imaginary
parts of both ϵ_r and μ_r which is a reasonable value given currently fabricated meta-
material structures [57, 58, 59]. The geometry used to numerically simulate the NIFL
in COMSOL is given in figure 2.5. The first step is characterizing the NIFL with a
transfer function. For a detailed discussion on the geometry setup and transfer func-
tion calculations, the reader is referred to [56]. Here, we present a brief mathematical
description of the compensation scheme.

The spatial Fourier transforms of the electric fields in the object and image planes
are related by the passive transfer function, $T_P(k_y)$ of the imaging system, which can
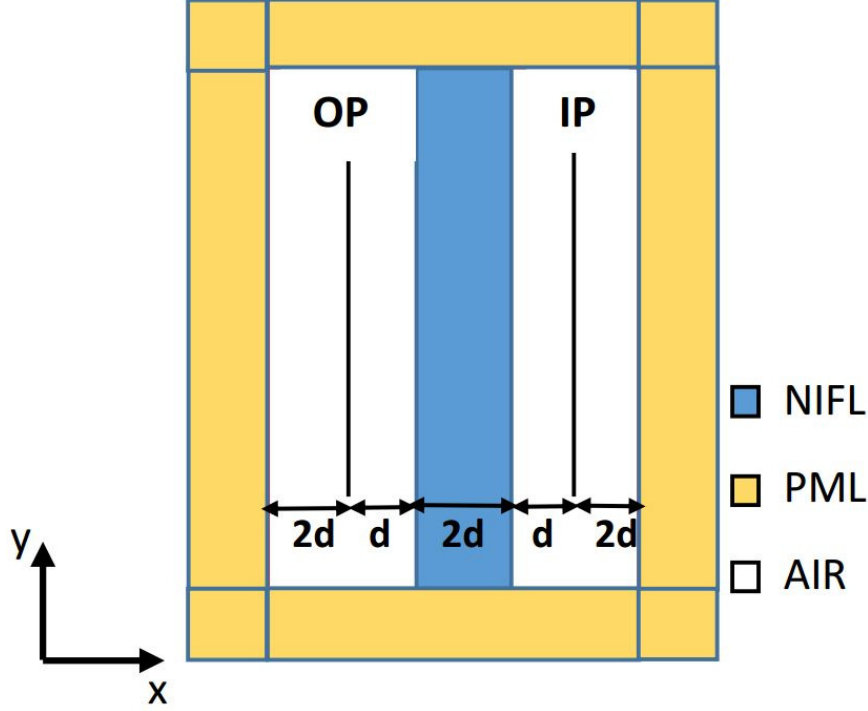
Figure 2.5: The geometry built in COMSOL to perform numerical simulations (not to scale). OP and IP are the object and image planes, respectively. Electric field is polarized along the z-axis (pointing out of plane). The object is defined as an electric field distribution $[E_z(y)]$ on the object plane. The operating wavelength is $\lambda_o = 1\mu m$ and $2d = 0.5\mu m$. Blue, white, and orange regions are the NIFL, air, and perfectly matched layer (PML), respectively.

be calculated with COMSOL. This is expressed mathematically as

$$I(k_y) = T_P(k_y)O(k_y). \tag{2.1}$$

Here $O(k_y) = \mathcal{F}\{O(y)\}$ and $I(k_y) = \mathcal{F}\{I(y)\}$, where $O(y)$ and $I(y)$ are the spatial

distribution of the electric fields in the object and image planes, respectively, and

$\mathcal{F}$ is the Fourier transform operator. According to [56] the passive compensation

is defined by the inverse of the transfer function. Hence, the loss compensation is

achieved by multiplying the raw image spectrum in Eq. 2.1 with the inverse of the

transfer function given by

$$C_P(k_y) = \left[T_P(k_y) \right]^{-1}.$$ (2.2)

For "*active*" compensation we first define a mathematical expression given by

$$A(k_y) = 1 + P(k_y),$$ (2.3)

$$P(k_y) = P_o exp\left[-\frac{(\frac{k_y}{k_o} - k_c)^2}{2\sigma^2} \right],$$ (2.4)

where P_o is a constant. k_c controls the center frequency of the Gaussian, $k_o = \frac{2\pi}{\lambda}$ is the free space wave number and σ controls the full width at half maximum (FWHM) of the Gaussian. We convolve $A(y) = \mathcal{F}^{-1}\{A(k_y)\}$ with the object $O(y)$ in the spatial domain and denote the new object by $O'(y)$. This is expressed as

$$O'(y) = \int\limits_{-\infty}^{\infty} O(y)A(y - \alpha)d\alpha.$$ (2.5)

We shall refer to this convolved object as the *total object*. Since convolution in the spatial domain is equivalent to multiplication in the spatial frequency domain, the Fourier spectrum of the total object $O'(k_y) = \mathcal{F}\{O'(y)\}$, is related to the original object by

$$O'(k_y) = O(k_y) + O(k_y)P(k_y).$$ (2.6)

The second term on the RHS will be referred to as the "*auxiliary source*," where P_o in

Eq. 2.4 defines its amplitude at the center frequency k_c. Note that this term, which is a convolution of $O(y)$ with $P(y) = \mathcal{F}^{-1}\{P(k_y)\}$, represents amplification in the spatial frequency domain provided that $P(k_y) > 1$. Even though the auxiliary source is object dependent, as we will discuss later, the external field to generate auxiliary source does not require prior knowledge about the object. Now, the Fourier transform of the fields in the object and image planes are related to each other by the transfer function of the NIFL as defined by Eq. 2.1. Therefore, in response to the total object, the new field distribution in the image plane, expressed as $I'(y) = \mathcal{F}^{-1}\{I'(k_y)\}$, is transformed as

$$I'(k_y) = T_P(k_y)O'(k_y), \tag{2.7}$$

where we can plug in the value of $O'(k_y)$ from Eq. 2.6 to obtain the convolved image

$$I'(k_y) = T_P(k_y)O(k_y) + T_P(k_y)O(k_y)P(k_y). \tag{2.8}$$

The second term on the RHS of Eq. 2.8 is a measure of the residual amplification which managed to propagate to the image plane. Therefore, by controlling P_o, from the object plane, we can tune the necessary amplification of high spatial frequency features to raise the desired frequency spectrum above the noise floor in the image plane. This process is illustrated in figure 2.6 for different auxiliary amplitudes.
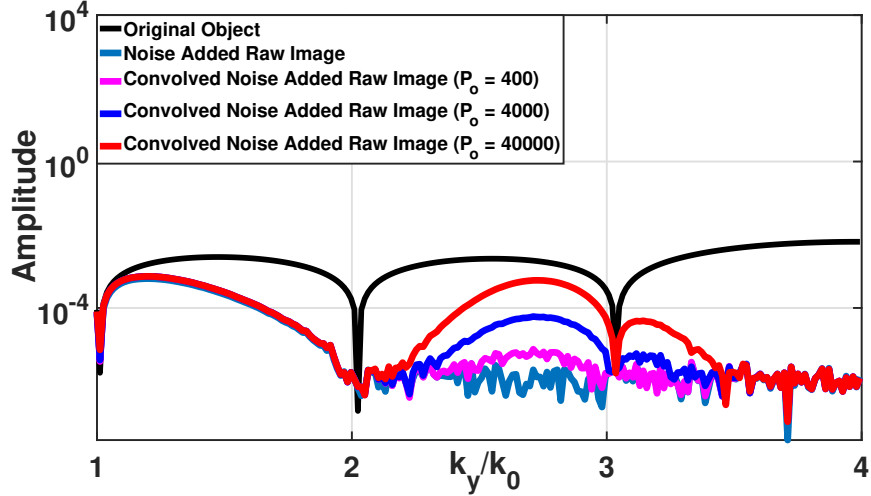
Figure 2.6: Fourier spectra $[Vm^{-1}]$ of an arbitrary object illustrating how the auxiliary amplitude can be tuned from the object plane to raise the image spectrum above the noise floor by controlling the amplification. $P(k_y)$ is centered at $k_c = \frac{k_y}{k_o} = 3$ with $\sigma = 0.13$.

The new "active" loss compensation scheme must consider the extra power that is now available in the image spectrum. We distinguish the compensation scheme from Eq. 2.2 with the subscript "A". We start by defining the active transfer function of the NIFL as

$$T_A(k_y) = \frac{I^{'}(k_y)}{O(k_y)}. \tag{2.9}$$

The numerator of Eq. 2.9 is the image of the total object which is given by Eq. 2.8. This transfer function is called "active" because it considers the auxiliary to be a part of the imaging system. Plugging in the value of $I^{'}(k_y)$ from Eq. 2.8 into Eq. 2.9 we obtain the following expression for the active transfer function,

$$T_A(k_y) = T_P(k_y) + T_P(k_y)P(k_y). \tag{2.10}$$

The active compensation filter is simply defined as the inverse of the active transfer function and is expressed mathematically by

$$C_A(k_y) = \left[T_P(k_y) + T_P(k_y)P(k_y) \right]^{-1}. \tag{2.11}$$
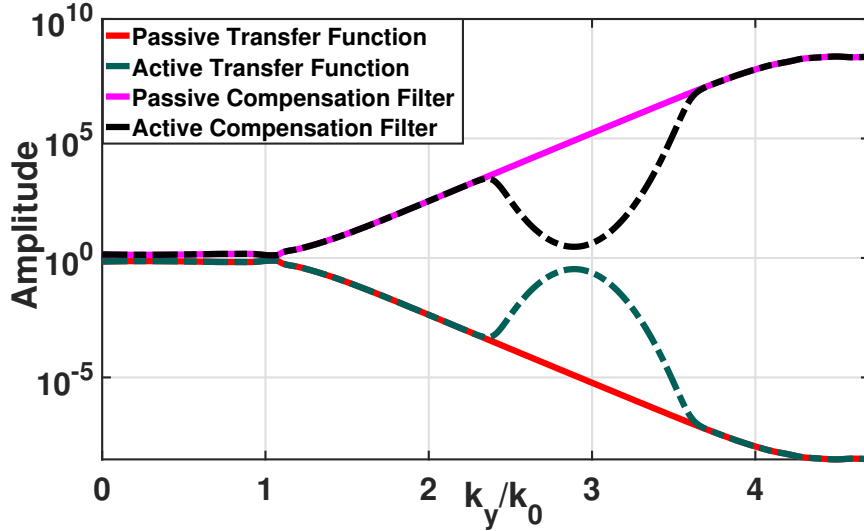
Figure 2.7: Comparisons of the passive transfer function $T_P(k_y)$ and compensation filter $C_P(k_y)$ with the active transfer function $T_A(k_y)$ and compensation filter $C_A(k_y)$. $P(k_y)$ incorporated into the active compensation filter is centered at $k_c = \frac{k_y}{k_o} = 3$ with $\sigma = 0.13$.

Figure 2.7 illustrates the active and passive transfer functions and the corresponding loss compensation schemes. The amount of active compensation drops within $2.5 < \frac{k_y}{k_o} < 3$. This indicates that in this region the auxiliary source is expected to provide compensation to the image. Therefore, the greater the auxiliary power, the lower is the required compensation through inverse filter within that region of spatial frequencies. It is interesting to note at this point the similarity of the active transfer functions in figure 2.7 and those in [60]. In the latter, however, highly stringent

conditions are imposed on the negative index lens to obtain such a transfer function.

2.3 Noise Characterization

The active compensation scheme will be applied to an NIFL imaging system affected by noise where the noise process is a circular Gaussian random variable. Although there are many different sources of noise, they can be broadly classified into, "signal-dependent" (SD) and "signal-independent" (SI). The random nature of noise manifests itself in the form of an uncertainty in the level of the desired signal. This uncertainty is quantified by the standard deviation σ_n. The actual distortion can be thought of as a random selection from an infinite set of values and the selection process obeys a probability distribution function. The standard deviation describes the range of values which have the greatest likelihood of being selected. When the underlying signal is distorted by multiple independent sources of noise, each characterized by Gaussian distributions, then the variance (σ_n^2) of the total noise is the sum of the variances of individual noise sources [61].

SD noise, as the name implies, is characterized by a σ_n that is intricately related to spatial (or temporal) variations in the incoming signal intensity. The magnitude of the signal distortion therefore also increases with the signal strength. Sources of

SD noise in an imaging system can be present on the detector side or the transmission medium. For example, the statistical nature of photons manifests itself as noise which has Poissonian statistics. In radiographic detection equipment, such sources of noise are called quantum mottle or quantum noise [62, 63]. Another source of SD noise originates from roughness of the transmission media, which in sub-wavelength imaging systems can be for example, surface roughness of the NIFL. One can think of surface irregularities as electromagnetic scatterers which radiate in different directions, distorting the propagating wave. Previous experiments on the impact of surface roughness [64, 65, 66] showed that increasing material losses in the NIFL improved the image resolution of the perfect lens for relatively large surface roughness. Although this may seem counter-intuitive, it can be explained if roughness is modelled as a source of scattering. Adding material loss is equivalent to lowering the power transmission of the lens. This lowers the magnitude of the excitation field responsible for scattering effects and in turn reduces the magnitude of the scattered field. If material losses are kept constant, the scattering process will be proportional to the intensity of illumination provided to the object. Therefore, such kind of noise is amplified as the illumination intensity is increased. On the other hand, the SI noise is quantified by a standard deviation which is not a function of the incoming signal. Therefore, the random nature of the noise will be visible only when the incoming signal amplitude is comparable to the distortions due to the SI noise. A good example of this is "dark noise", which affects a CCD sensor even in the absence of illumination [67].

A well known model [68] used to describe the spatial distribution of a signal that has been distorted with both SD and SI sources of noise is

$$r(y) = s(y) + f(s(y))N_1(y) + N_2(y), \tag{2.12}$$

where $s(y)$ is the noiseless or ideal signal and $r(y)$ is the noisy version. $N_1(y)$ and $N_2(y)$ are two statistically independent random noise processes with zero mean and Gaussian probabilities with standard deviations σ_{n1} and σ_{n2}, respectively. The noise processes $N_1(y)$ and $N_2(y)$ are signal independent. The signal dependent nature of noise is modelled by modulating $N_1(y)$ using the function $f(s(y))$. Generally, $f(s(y))$ is a non-linear function of the ideal signal itself which is chosen based on the system which Eq. 2.12 is attempting to describe. For example, $f(s(y))$ is usually considered to be the photographic density which is unitless when modelling signal-dependent film grain noise. Therefore, $f(s(y))N_1(y)$ represents the effective signal dependent noise term. We can re-write the expression in Eq. 2.12 as

$$r(y) = s(y) + N_{SD}(y) + N_{SI}(y), \tag{2.13}$$

where the standard deviation of $N_{SD}(y)$ is $f(s(y))\sigma_{n1}$ and the subscripts SD, SI distinguish between the sources of noise. The noise model of Eq. 2.12, referred to as the *signal modulated noise model*, is used for signal estimation purposes with the Wiener filter. A detailed discussion on this can be found in [68, 69, 70, 71]. However,

we will use Eq. 2.13 in this paper for mathematical convenience to analyse the relative contributions of SD and SI noise.

In the NIFL imaging system which we consider, the ideal signal $s(y)$ will be the electric field distribution on the image plane, that is $I(y)$ and $I'(y)$ for passive and active schemes, respectively. In [60], Chen, et. al adopted a $60dB$ signal to noise ratio (SNR) in their negative index lens considering an experimental imaging system detector [72]. This corresponds to a SD standard deviation of $10^{-3}I(y)$. In this work, we adopt the same standard for the SD noise. Additionally, we assume a SI noise process in the imaging system by adopting a spatially invariant standard deviation of $10^{-3}[V/m]$. This means that even in the absence of illumination, there is a constant background noise of the order of $1\ mV/m$ in the detector. Although the value of the SI noise is chosen arbitrarily, this does not limit the results discussed in this paper, since the SI noise can be easily suppressed by additional auxiliary power.

By taking into consideration the SNR standard used by Chen, et. al [60] and the mathematical form of Eq. 2.13 we can frame the equations for the noisy images as

$$I_N(y) = I(y) + N_{SD}(y) + N_{SI}(y) \tag{2.14}$$

and

$$I'_N(y) = I'(y) + N'_{SD}(y) + N'_{SI}(y) \tag{2.15}$$

corresponding to the ideal images described by Eqs. 2.1 and 2.8, respectively. The subscript N indicates the noisy image. The standard deviations of the noise processes are

$$\sigma_{n(SD)} = 10^{-3} I(y), \tag{2.16}$$

$$\sigma'_{n(SD)} = 10^{-3} I'(y) \tag{2.17}$$

and

$$\sigma_{n(SI)} = \sigma'_{n(SI)} = 10^{-3} \ V/m. \tag{2.18}$$

Eqs. 2.16 - 2.18 fully describe the random variables that are used to construct the SI and SD noise terms in Eqs. 2.14 and 2.15.
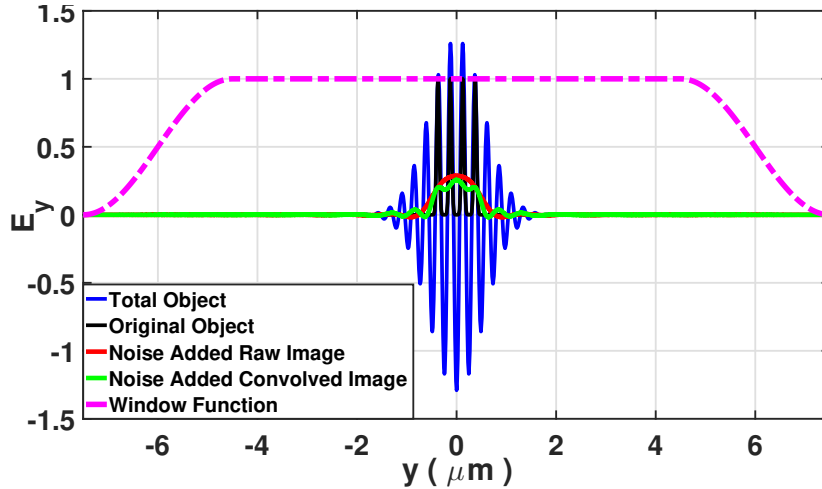
Figure 2.8: Electric field $[Vm^{-1}]$ distributions in the object and image planes. The fields on the image planes are multiplied by the window function to reduce the errors in the Fourier transform. The total object has been scaled down by $\approx 10^4$.

41

2.4 Results

Having described how both SD and SI noise are added to the system, the next step is to evaluate the performance of active-compensation and compare with the passive version. We will attempt to image the previously exemplified object comprising four Gaussian features, separated by $\frac{\lambda_o}{4}$ with $\lambda_o = 1\mu m$ and compare the results of passive and active compensation. Note that due to the finite extent of the image plane, it is necessary to multiply the electric fields with a window function to ensure that the field drops to zero where the image plane is abruptly terminated. Otherwise, errors are introduced in the Fourier transform calculations. Windowing the field distribution simply reduces these sources of error, which will be then visible only in the higher spatial frequencies. Since these errors are very small compared with the amplitude of the SD and SI sources of noise, they do not have a significant impact on the calculations. Increasing the length of the image plane along the y-axis can also reduce these errors, but because of computational constraints this may not be desirable.

Figure 2.8 shows the spatial electric field distributions on the object and image planes. Noise was artificially added to the fields on the image plane that were calculated with COMSOL. The resultant noisy images are indicated by the red and green lines in the figure. The Tukey (tapered cosine) window function was applied to the image plane

only. The Fourier transforms of the images, with and without added noise are shown in figure 2.9. The black line, which corresponds to $I_N(k_y)$ in Eq. 2.14, shows how the added noise has clearly affected the raw image spectrum beyond $\frac{k_y}{k_o} = 2$, where all of the object features are now completely buried under the noise and indiscernible. However, the blue line, which corresponds to $I'_N(k_y)$ in Eq. 2.15, shows how these features can be recovered with the convolved auxiliary.

We propose the following iterative process to apply the auxiliary source. We then use active compensation filter to reconstruct the image spectrum.

1. Select an arbitrary k_c in the region where the noise has substantially degraded the spectrum. Choose a guess auxiliary amplitude by selecting P_0.

2. Convolve the object with $A(y)$ to obtain the total object.

3. Measure the electric fields on the image plane corresponding to the total object.

4. Re-scale P_0 for the selected k_c if necessary, to make sure that adequate amplification is available in the image plane and noise is not visible in the Fourier spectrum.

5. Select another k_c on the noise floor and ensure that there is sufficient overlap between the adjacent auxiliaries.

6. Repeat the processes in $1 - 5$ by superimposing those multiple auxiliaries until the transfer function of the imaging system is reasonably accurate. We were

restricted by the inaccuracy of the simulated passive transfer function $T_P(k_y)$ beyond $\frac{k_y}{k_o} = 4.7$ which prevented us from going beyond.

Note that in the above steps the selection of P_o does not require prior knowledge about the object. The blue and green lines of figure 2.9 show the total images with and without added noise, respectively. They include four auxiliary sources with the center frequencies $k_c = k_y/k_o = 2.8,\ 3.1,\ 3.6,\ 4.2$ and $P_o = 3000,\ 10000,\ 4\times 10^5,\ 10^6$, respectively, with the same $\sigma = 0.35$. The final $A(y)$ was then convolved with the object and the resulting total field distribution on the object plane is shown by the blue line in figure 2.8.

Active compensation filter, defined by Eq. 2.11 and illustrated in figure 2.10, is then multiplied in the spatial frequency domain by the total image spectrum with the added noise. The resulting compensated spectrum is the red line of figure 2.10. The noise, which was visible in the total image spectrum beyond $\frac{k_y}{k_o} = 4.5$, is also amplified in this reconstruction process. However, in the regions where the auxiliary source is sufficiently strong, suppression of noise amplification is evident. The reconstructed spectrum perfectly coincides with the original object shown by the black curve in figure 2.10. The light blue line corresponds to the passively compensated image obtained by multiplying Eq. 2.2 (i.e., dark blue line in figure 2.10) with the noise added raw image (i.e., black line in figure 2.9). The advantage of the active compensation over its passive counterpart is therefore clearly evident from the reconstructed Fourier

spectrum. After the loss compensation process, the spectrum is truncated at $\frac{k_y}{k_o} = 4.7$ because the simulated transfer function loses accuracy.
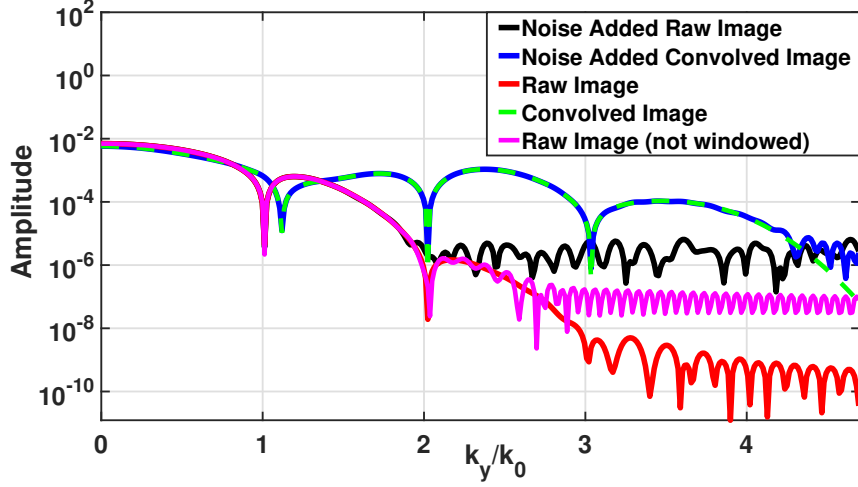
Figure 2.9: Amplitude of the Fourier transforms $[Vm^{-1}]$ on a log scale. Red and green lines are the image spectra $I(k_y)$ and $I'(k_y)$ with no added noise, respectively. The blue line shows the image of the total object with added noise, $I'_N(k_y)$. Noise is visible at $\frac{k_y}{k_o} > 4.5$ due to the inadequate amplification. The apparent noise in the pink line are due to the numerical errors introduced by the Fourier transform and shifts to higher $\frac{k_y}{k_o}$ values after applying the Tukey window as seen in the red line.

Figure 2.7 shows that the passive transfer function starts to flatten beyond $\frac{k_y}{k_o} = 4.5$, even though the analytical transfer function monotonically decreases (see figure 3 in [60]), inaccurate simulated transfer function $T_P(k_y)$ indicates that it is no longer possible to perform the required compensation accurately (see Eq. 2.11). More precisely, the imaging system requires more compensation than the transfer function predicts. The reconstructed spectrum therefore starts to deviate from the original object when $\frac{k_y}{k_o} > 4.5$ as seen in the red plot of figure 2.10, indicating inadequate compensation. This was one of the main reasons why we were unable to image

beyond $\frac{k_y}{k_o} = 5$.
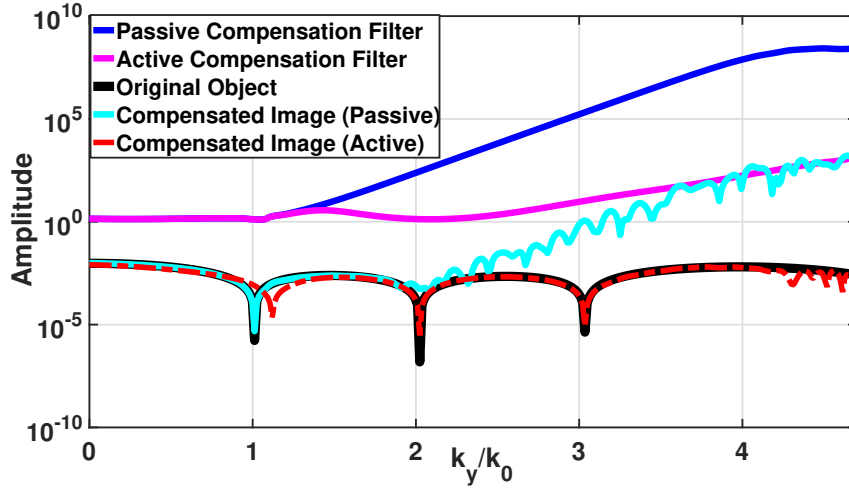
Figure 2.10: Fourier spectra $[Vm^{-1}]$ of the reconstructed images illustrating the difference between active and passive compensation. The passive compensation has significantly amplified the noise whereas the active one does not.

Additionally, reconstructing the object features successfully requires a strong amplification. The auxiliary amplitude necessary to produce this amplification is very high and it starts to generate substantial electric field oscillations towards the edges of the image plane. Because the image plane is finite along the y-axis and the electric field is abruptly cut at a point where it is non-zero, a computational error is introduced in the spatial Fourier transform. An artefact of this can be seen in figure 2.10 where the red plot shows that the feature at $\frac{k_y}{k_o} = 1$ is slightly shifted. The error is more prominent when the intensity of illumination is increased. Extending the size of the image plane along the y-axis mitigates the error at the expense of computational or physical resources.
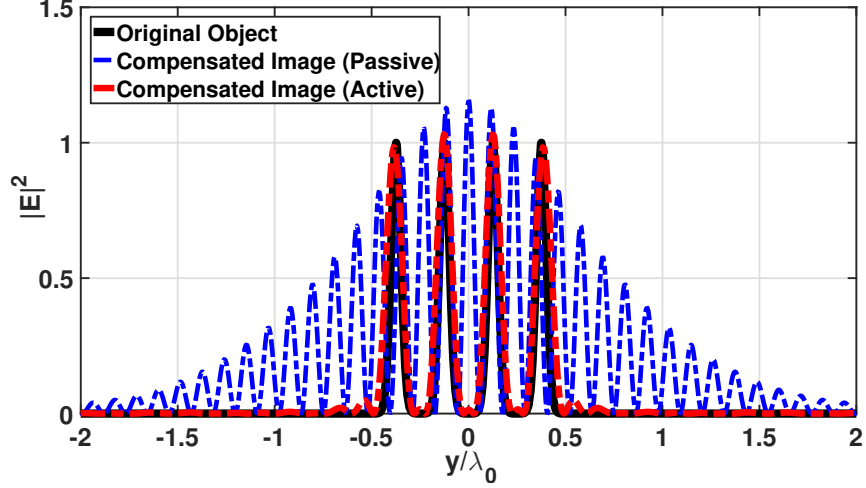
Figure 2.11: Reconstructed images showing the difference between active and passive compensation schemes. Note that the passively compensated image has been scaled down by 10^7.

Note that towards the tails of the amplification, or when $\frac{k_y}{k_o} > 4.5$, the amplification is not strong enough to overcome the noise. Hence, there should be sufficient overlap between the two adjacent auxiliaries. The FWHM of $P(k_y)$, controlled by σ, can be selected arbitrarily. In our simulations we were limited by the finite image plane. A very narrow $P(k_y)$ in the spatial frequency domain translates to a wide field distribution in the spatial domain. This created additional field oscillations towards the edges of the image plane increasing the errors in the Fourier transform calculations. Figure 2.11 shows the amplitude squared of the reconstructed fields illustrating the improvement of the active over passive compensation scheme.

2.5 Discussion

The active compensation scheme works, because the convolved auxiliary source allows us to *"selectively amplify"* spatial frequency features of the object. This amplification cannot be achieved simply by the superposition of the object with an object independent auxiliary source. This is illustrated in figure 2.12 where we set $O(k_y) = 1Vm^{-1}$ in the second term of Eq. 2.6 and use the same $P(k_y)$ distributions in figure 2.9. The blue and green lines correspond to the images of the object superimposed with the object independent auxiliaries with and without added noise, respectively. The buried object spectrum at $\frac{k_y}{k_o} = 3$ shown in figure 2.9 has gone undetected.
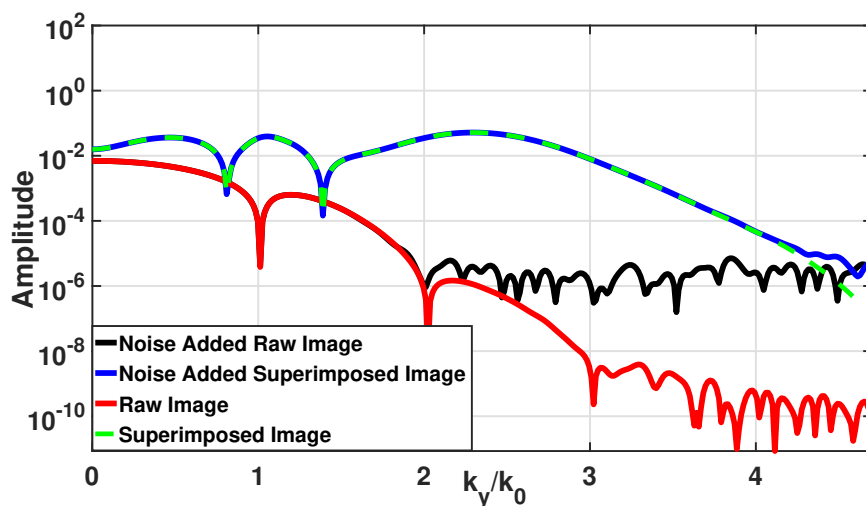
Figure 2.12: Fourier spectra $[Vm^{-1}]$ of the raw image superimposed with several object independent auxiliaries. Such superposition does not provide amplification and hence the feature at $\frac{k_y}{k_o} = 3$ is not recovered. Note that the black and red lines are the raw images with and without added noise, respectively, as also shown in figure 2.9.

The convolution process to construct the auxiliary source that was described in this paper can be thought of as a form of structured light illumination or wavefront engineering [73, 74, 75, 76, 77, 78, 79, 80]. Along these lines, for example, a plasmonic lens imaging system was discussed recently in [73], where the authors described the fields on the image plane by Eq. 2.1 that contains an illumination function as a result of a phase shifting mask. Spatial filters based on hyperbolic metamaterials [81, 82, 83] may be promising for the implementation of the proposed convolution. For example, an object illuminated with a high intensity plane wave and projected on such spatial filters can physically implement the convolved auxiliary source corresponding to the second term in Eq. 2.6 and used in step 2 of the iterative reconstruction process. Here, the spatial filter needs to be engineered to have a transfer function of the form similar to Eq. 2.4. The object (i.e., such as an aperture based object illuminated by a plane wave) is to be placed on top of this additional metamaterial layer. The field distribution at the exit of this layer would be the convolution of the object field distribution with the point spread function of the layer, hence leading to the auxiliary source term in Eq. 2.6 (i.e., second term). One way to engineer such a transfer function is with the hyperbolic metamaterials which support high spatial frequency modes. In [83], for example, the transmission coefficient for the transverse magnetic waves in a hyperbolic medium was shown to have multiple peaks in the high spatial frequency region. The position of these peaks can be tuned by changing the filling

fraction or the thickness of the hyperbolic medium. If one has engineered a meta-material with a transfer function having one transmission peak P_0 around a certain spatial frequency (i.e., center spatial frequency k_c in Eq. 2.4) and is zero everywhere else, the iterative process where P_0 is re-scaled (i.e., to control amplification) is functionally equivalent to re-scaling the amplitude of the plane wave E_0 illuminating the object. It is also worth mentioning here that this physically means actively adjusting the coherent plasmon injection rate in the imaging system to compensate the losses as conceptualized in [52]. On the other hand, controlling the center frequency will require multiple or tunable metamaterial structures where the transfer function can be tuned to show transmittance peaks at different center frequencies. Therefore, it would be advantageous to have a broad transmittance in a physical implementation as long as the noise amplification does not start to dominate. Another possible way to construct the necessary transfer function may be with the use of metasurfaces [84], which are ultrathin nanostructures fabricated at the interface of two media. The scattering properties of the sub-wavelength resonant constituents of the metasurfaces can be engineered to control the polarization, amplitude, phase, and other properties of light [74, 75, 76, 77, 85, 86]. This can allow one to engineer an arbitrary field pattern from a given incident illumination [85, 86].

In order to understand how the active compensation enhances the resolution limit of the NIFL we need a deeper understanding of the effect of the noise on the ideal image spectrum. Eqs. 2.16 and 2.17 tell us that the signal dependent noise is amplified

proportionally with the illumination. But since the active compensation seems to work so well, can we say that the noise is not amplified to the same extent as the signal? Then, would it be possible to achieve the same results by simply increasing the intensity of the plane wave illuminating the object? To address these questions we will consider below the *"weak illumination," "structured illumination"* and *"strong illumination"* cases.

We will take the Fourier transforms of Eqs. 2.14 and 2.15 and analyze how each noise term contributes to the total distortion of the ideal image under the three illumination schemes. The linearity of the Fourier transform allows us to plot each term in the equations separately and these are shown in figures 2.13 - 2.15 for the weak, strong, and structured illuminations, respectively. In the strong illumination case we have used a plane wave whose electric field is 10^8 times stronger than the weak illumination. The green and black lines in figures 2.13 - 2.15 correspond to the images with and without added noise, respectively. The Fourier transforms of the SI and SD noise are the blue and gold lines, respectively, which add up to the total noise shown by the red line.

To compare the performance of the imaging system under the three illumination schemes, we will see how closely the noise added images overlap with the images with no added noise. We should note that the spatial distribution of the SD noise will be spread out over multiple Fourier components [87] and therefore the random nature
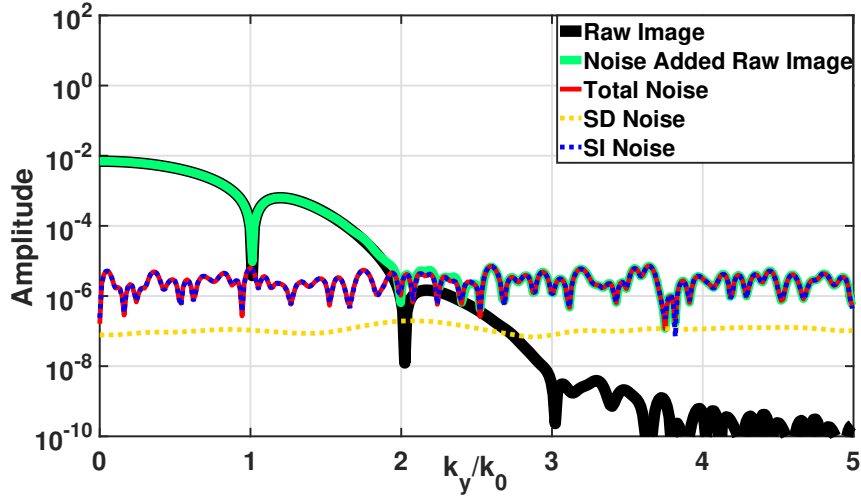
Figure 2.13: Fourier spectra $[Vm^{-1}]$ of the raw images with and without added noise illustrating the contribution of the SD and SI noise to the total distortion of the image under the weak illumination case.

of noise will not be visible in the spatial frequency domain. This can be seen in the

gold plots which are fairly smooth compared to the blue lines.
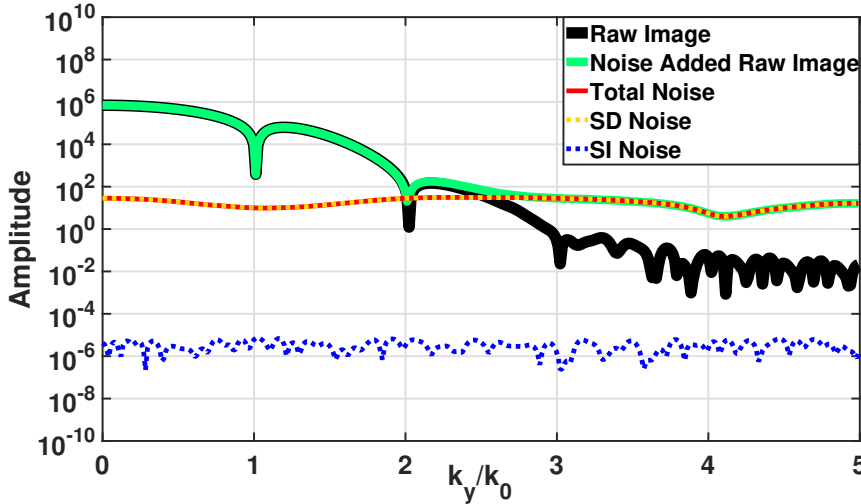
Figure 2.14: Fourier spectra $[Vm^{-1}]$ of the raw images with and without added noise illustrating the contribution of the SD and SI noise to the total distortion of the image under the strong illumination case. The SD noise is amplified approximately by a factor of 10^8 throughout the spectrum and the contribution of the SI noise is very small.
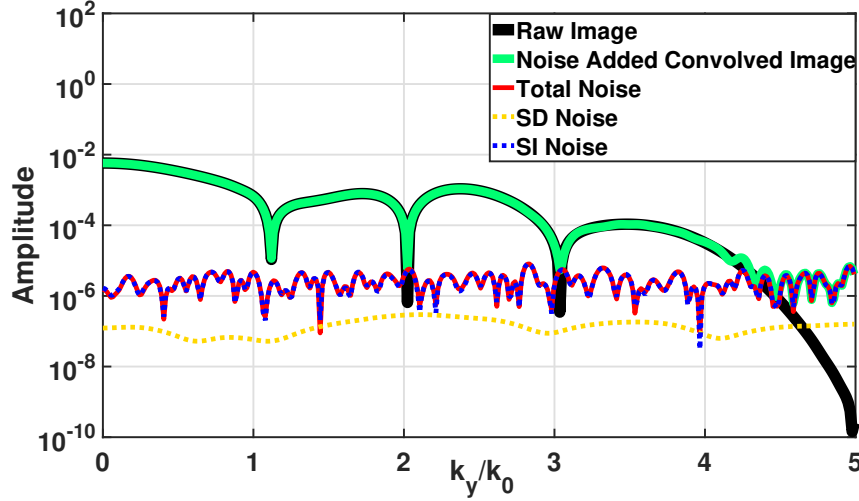
Figure 2.15: Fourier spectra $[Vm^{-1}]$ of the convolved images with and without added noise illustrating the contribution of the SD and SI noise to the total distortion of the image under the structured illumination case. The SD noise is approximately at the same level as the weak illumination except that the noise is redistributed.

If we compare the SD noise spectra in figures 2.13 and 2.14 we immediately conclude that as we increase the intensity of the illumination, the SD noise is amplified throughout the spectrum. However, a slight improvement to the noisy spectrum over the weak illumination is visible within the region $2 < \frac{k_y}{k_o} < 3$. Additionally, if we analyze figure 2.13, where the gold line intersects the black line, we see that in the strong illumination case in figure 2.14, only the Fourier components until this intersection point are recovered. The intersection marks the spatial frequency at which the ideal image (i.e., raw image with no added noise) $I(k_y)$ matches the Fourier transform of the SD noise $N_{SD}(k_y)$. Beyond this point, we can say that the ideal image is completely buried under the SD noise alone. As we steadily increase the intensity of the illumination, $I(k_y)$ and $N_{SD}(k_y)$ increase by the same proportion and therefore, the value of $\frac{k_y}{k_o}$ where the two intersect does not change. We can therefore say that the

improvement in the noisy spectrum in figure 2.14 is due to the signal rising above the SI noise which does not change with the illumination intensity. Further increments in the strength of the illumination will not improve the noisy image spectrum.

On the other hand, if we study the SD noise spectrum in figure 2.15, we can see that it is approximately at the same average level as figure 2.13. This is not surprising if we compare the green and red plots of figure 2.8. We can see that the spatial electric field distribution of the noise added images $I'_N(y)$ and $I_N(y)$ are comparable. The only difference is that $I'_N(y)$ has high spatial frequency features. Since the standard deviation of the SD noise is proportional to the amplitude of the image, according to Eqs. 2.16 and 2.17, we can see why the SD noise is approximately the same in both the weak and structured illumination schemes. Note that under the structured illumination, the noise added convolved image closely follows the ideal image until $\frac{k_y}{k_o} = 4.5$. This can be pushed to even higher spatial frequencies if the transfer function characterizing the lens is accurate. Also, note that the structured illumination has successfully suppressed the computational errors in the Fourier transform which are visible in the black line in figure 2.13 beyond $\frac{k_y}{k_o} = 3$. These errors are amplified by a factor of 10^8 times in figure 2.14.

From the above discussion we conclude that by using structured illumination the SD noise is not amplified but redistributed when compared with the strong illumination. Therefore, it is possible to raise the high spatial frequency features of the object above

the noise. This is the primary reason why structured illumination can accurately resolve the image while strong illumination fails.

The technique is generally applicable to any arbitrary object with the use of any plasmonic or metamaterial lens provided that accurate transfer function for the imaging system is available. A selective amplification process is used to recover specific object features by controlling P_0 near and beyond where the noise floor is reached in the Fourier spectrum of the raw image. Therefore, no prior knowledge of the object is required. However, a necessary criterion is a sufficiently accurate transfer function in the region where the auxiliary is applied to correctly estimate the required amount of amplification. It should be noted that different objects may require different auxiliaries, since the spatial frequency at which the noise floor is reached may vary for different objects. Therefore, it would be instrumental to have a tunability mechanism for the versatility of the imaging system. Even though a single narrowband auxiliary would be still sufficient to enhance the resolution of the raw image, further enhancement in the resolution would demand either superimposing multiple narrowband auxiliaries or a single sufficiently broadband auxiliary within the range of accurate transfer function. Narrowband auxiliaries require larger image plane and more post-processing while a single broadband auxiliary requires less post-processing and smaller image plane at the expense of possibly higher noise amplification. Similarly, unnecessarily large amplitude of a narrowband auxiliary may excessively amplify the noise. Another likely limitation arises from increasingly large power loss in the

deep subwavelength regime, which requires increasingly high amount of amplification to reconstruct extremely fine details of the object. This does not only reduce the efficiency but might also introduce undesired non-linear and thermal effects in the optical materials, hence, limiting the resolution of the imaging system.

2.6   Conclusion

In summary, we proposed an active implementation of the recently introduced plasmon injection scheme [52] to significantly improve the resolution of Pendry's non-ideal negative index flat lens beyond diffraction limit in the presence of realistic material losses and SD noise. Simply by increasing the illumination intensity, it is not generally possible to efficiently reconstruct the image due to the noise amplification. However, in the proposed active implementation one can counter the adverse noise amplification effect by using a convolved auxiliary source which allows for a selective amplification of the high spatial frequency features deep within the sub-wavelength regime. We have shown that this approach can be used to control the noise amplification while at the same time recover features buried within the noise, thus enabling ultra-high resolution imaging far beyond the previous passive implementations of the plasmon injection scheme [56, 88]. The convolution process to construct the auxiliary source in the proposed active scheme may be realized physically by different methods, metasurfaces [74, 75, 76, 77, 78, 84, 85, 86] and hyperbolic metamaterials

[81, 82, 83, 89] being the primary candidates. A more detailed analysis on the design of such structures to implement the convolved auxiliary source will be the focus of our future research. Finally, we should note that we purposefully focused on imperfect negative index flat lens here that poses a highly stringent and conservative problem. However, in the shorter term the proposed method can be relatively easily applied to experimentally available plasmonic superlenses [1, 2, 3, 64, 66, 73] and hyperlenses [4, 5, 6, 7, 8]. Our findings also raises the hopes for reviving Pendry's early vision of perfect lens [39] by decoupling the loss and isotropy issues toward a practical realization [90, 91, 92, 93, 94, 95].

References

[1] Nicholas Fang, Hyesog Lee, Cheng Sun, and Xiang Zhang. Diffraction-limited optical imaging with a silver superlens. *Science*, 308(5721):534–537, 2005.

[2] Thomas Taubner, Dmitriy Korobkin, Yaroslav Urzhumov, Gennady Shvets, and Rainer Hillenbrand. Near-field microscopy through a sic superlens. *Science*, 313(5793):1595–1595, 2006.

[3] Xiang Zhang and Zhaowei Liu. Superlenses to overcome the diffraction limit. *Nature materials*, 7(6):435–441, 2008.

[4] Zhaowei Liu, Hyesog Lee, Yi Xiong, Cheng Sun, and Xiang Zhang. Far-field optical hyperlens magnifying sub-diffraction-limited objects. *science*, 315(5819):1686–1686, 2007.

[5] Junsuk Rho, Ziliang Ye, Yi Xiong, Xiaobo Yin, Zhaowei Liu, Hyeunseok Choi, Guy Bartal, and Xiang Zhang. Spherical hyperlens for two-dimensional sub-diffractional imaging at visible frequencies. *Nature communications*, 1:143, 2010.

[6] Dylan Lu and Zhaowei Liu. Hyperlenses and metalenses for far-field super-resolution imaging. *Nature communications*, 3:1205, 2012.

[7] Jingbo Sun, Mikhail I Shalaev, and Natalia M Litchinitser. Experimental demonstration of a non-resonant hyperlens in the visible spectral range. *Nature communications*, 6:7201, 2015.

[8] Hyesog Lee, Zhaowei Liu, Yi Xiong, Cheng Sun, and Xiang Zhang. Development of optical hyperlens for imaging below the diffraction limit. *Optics express*, 15(24):15886–15891, 2007.

[9] Jason Valentine, Shuang Zhang, Thomas Zentgraf, Erick Ulin-Avila, Dentcho A Genov, Guy Bartal, and Xiang Zhang. Three-dimensional optical metamaterial with a negative refractive index. *nature*, 455(7211):376–379, 2008.

[10] NI Landy, S Sajuyigbe, JJ Mock, DR Smith, and WJ Padilla. Perfect metamaterial absorber. *Physical review letters*, 100(20):207402, 2008.

[11] Vasily V Temnov. Ultrafast acousto-magneto-plasmonics. *Nature Photonics*, 6(11):728–736, 2012.

[12] Muhammad I Aslam and Durdu Ö Güney. On negative index metamaterial spacers and their unusual optical properties. *Progress in Electromagnetic Research B*, 6:203–217, 2013.

[13] Mehdi Sadatgol, Mahfuzur Rahman, Ebrahim Forati, Miguel Levy, and Durdu Ö

Güney. Enhanced faraday rotation in hybrid magneto-optical metamaterial structure of bismuth-substituted-iron-garnet with embedded-gold-wires. *Journal of Applied Physics*, 119(10):103105, 2016.

[14] Muhan Choi, Seung Hoon Lee, Yushin Kim, Seung Beom Kang, Jonghwa Shin, Min Hwan Kwak, Kwang-Young Kang, Yong-Hee Lee, Namkyoo Park, and Bumki Min. A terahertz metamaterial with unnaturally high refractive index. *Nature*, 470(7334):369–373, 2011.

[15] W-C Chen, Christopher M Bingham, Kelley M Mak, Nicholas W Caira, and Willie J Padilla. Extremely subwavelength planar magnetic metamaterials. *Physical Review B*, 85(20):201104, 2012.

[16] Xu Zhang, Elvis Usi, Suhail K Khan, Mehdi Sadatgol, and Durdu Ö Guney. Extremely sub-wavelength negative index metamaterial. *Progress In Electromagnetics Research*, 152:95–104, 2015.

[17] David Schurig, JJ Mock, BJ Justice, Steven A Cummer, John B Pendry, AF Starr, and DR Smith. Metamaterial electromagnetic cloak at microwave frequencies. *Science*, 314(5801):977–980, 2006.

[18] J Gwamuri, DÖ Güney, and JM Pearce. Advances in plasmonic light trapping in thin-film solar photovoltaic devices. *Solar cell nanotechnology*, pages 241–269, 2013.

[19] Carsten Rockstuhl, Stephan Fahr, and Falk Lederer. Absorption enhancement in solar cells by localized plasmon polaritons. *Journal of applied physics*, 104(12):123102, 2008.

[20] Ankit Vora, Jephias Gwamuri, Nezih Pala, Anand Kulkarni, Joshua M Pearce, and Durdu Ö Güney. Exchanging ohmic losses in metamaterial absorbers with useful optical absorption for photovoltaics. *Scientific Reports*, 4:4901, 2008.

[21] Ankit Vora, Jephias Gwamuri, Joshua M Pearce, Paul L Bergstrom, and Durdu Ö Güney. Multi-resonant silver nano-disk patterned thin film hydrogenated amorphous silicon solar cells for staebler-wronski effect compensation. *Journal of Applied Physics*, 116(9):093103, 2014.

[22] Irfan Bulu, Humeyra Caglayan, Koray Aydin, and Ekmel Ozbay. Compact size highly directive antennas based on the srr metamaterial medium. *New Journal of Physics*, 7(1):223, 2005.

[23] H Odabasi, FL Teixeira, and DO Guney. Electrically small, complementary electric-field-coupled resonator antennas. *Journal of Applied Physics*, 113(8):084903, 2013.

[24] Durdu Ö Güney and David A Meyer. Negative refraction gives rise to the klein paradox. *Physical Review A*, 79(6):063834, 2009.

[25] Igor I Smolyaninov and Evgenii E Narimanov. Metric signature transitions in optical metamaterials. *Physical Review Letters*, 105(6):067402, 2010.

[26] Mark S Tame, KR McEnery, ŞK Özdemir, J Lee, SA Maier, and MS Kim. Quantum plasmonics. *Nature Physics*, 9(6):329–340, 2013.

[27] Md Abdullah al Farooqui, Justin Breeland, Muhammad I Aslam, Mehdi Sadatgol, Şahin K Özdemir, Mark Tame, Lan Yang, and Durdu Ö Güney. Quantum entanglement distillation with metamaterials. *Optics express*, 23(14):17941–17954, 2015.

[28] Motoki Asano, Muriel Bechu, Mark Tame, Şahin Kaya Özdemir, Rikizo Ikuta, Durdu Ö Güney, Takashi Yamamoto, Lan Yang, Martin Wegener, and Nobuyuki Imoto. Distillation of photon entanglement using a plasmonic metamaterial. *Scientific reports*, 5:18313, 2015.

[29] Pankaj K Jha, Xingjie Ni, Chihhui Wu, Yuan Wang, and Xiang Zhang. Metasurface-enabled remote quantum interference. *Physical review letters*, 115(2):025501, 2015.

[30] Ralph A Sperling, Pilar Rivera Gil, Feng Zhang, Marco Zanella, and Wolfgang J Parak. Biological applications of gold nanoparticles. *Chemical Society Reviews*, 37(9):1896–1908, 2008.

[31] Xiaohua Huang, Ivan H El-Sayed, Wei Qian, and Mostafa A El-Sayed. Cancer cell imaging and photothermal therapy in the near-infrared region by using gold nanorods. *Journal of the American Chemical Society*, 128(6):2115–2120, 2006.

[32] Surbhi Lal, Susan E Clare, and Naomi J Halas. Nanoshell-enabled photothermal cancer therapy: impending clinical impact. *Accounts of chemical research*, 41(12):1842–1851, 2008.

[33] Rui Guo, Leyang Zhang, Hanqing Qian, Rutian Li, Xiqun Jiang, and Baorui Liu. Multifunctional nanocarriers for cell imaging, drug delivery, and near-ir photothermal therapy. *Langmuir*, 26(8):5428–5434, 2010.

[34] Zachary J. Coppens, Wei Li, D. Greg Walker, and Jason G. Valentine. Probing and controlling photothermal heat generation in plasmonic nanostructures. *Nano Letters*, 13(3):1023–1028, 2013.

[35] Matthew D Blankschien, Lori A Pretzer, Ryan Huschka, Naomi J Halas, Ramon Gonzalez, and Michael S Wong. Light-triggered biocatalysis using thermophilic enzyme–gold nanoparticle complexes. *ACS nano*, 7(1):654–663, 2012.

[36] Yun-Sheng Chen, Wolfgang Frey, Seungsoo Kim, Kimberly Homan, Pieter Kruizinga, Konstantin Sokolov, and Stanislav Emelianov. Enhanced thermal stability of silica-coated gold nanorods for photoacoustic imaging and image-guided therapy. *Optics express*, 18(9):8867–8878, 2010.

[37] Sarah P Sherlock, Scott M Tabakman, Liming Xie, and Hongjie Dai. Photothermally enhanced drug delivery by ultra-small multifunctional feco/graphitic-shell nanocrystals. *Acs Nano*, 5(2):1505, 2011.

[38] Arash Ahmadivand, Nezih Pala, and Durdu Ö Güney. Enhancement of photothermal heat generation by metallodielectric nanoplasmonic clusters. *Optics express*, 23(11):A682–A691, 2015.

[39] J. B. Pendry. Negative refraction makes a perfect lens. *Phys. Rev. Lett.*, 85:3966–3969, Oct 2000.

[40] Wyatt Adams, Mehdi Sadatgol, and Durdu Ö Güney. Review of near-field optics and superlenses for sub-diffraction-limited nano-imaging. *AIP Advances*, 6(10):100701, 2016.

[41] Shuang Zhang, Wenjun Fan, N. C. Panoiu, K. J. Malloy, R. M. Osgood, and S. R. J. Brueck. Experimental demonstration of near-infrared negative-index metamaterials. *Phys. Rev. Lett.*, 95:137404, Sep 2005.

[42] A. N. Grigorenko, A. K. Geim, H. F. Gleeson, Y. Zhang, A. A. Firsov, I. Y. Khrushchev, and J. Petrovic. Nanofabricated media with negative permeability at visible frequencies. *Nature*, 438(7066):335–338, 2005.

[43] Gunnar Dolling, Christian Enkrich, Martin Wegener, Costas M. Soukoulis, and Stefan Linden. Simultaneous negative phase and group velocity of light in a metamaterial. *Science*, 312(5775):892–894, 2006.

[44] K. J. Webb, M. Yang, D. W. Ward, and K. A. Nelson. Metrics for negative-refractive-index materials. *Phys. Rev. E*, 70:035602, Sep 2004.

[45] Ming-Chuan Yang and Kevin J. Webb. Poynting vector analysis of a superlens. *Opt. Lett.*, 30(18):2382–2384, Sep 2005.

[46] Maziar P. Nezhad, Kevin Tetz, and Yeshaiahu Fainman. Gain assisted propagation of surface plasmon polaritons on planar metallic waveguides. *Opt. Express*, 12(17):4072–4079, Aug 2004.

[47] Alexander K. Popov and Vladimir M. Shalaev. Compensating losses in negative-index metamaterials by optical parametric amplification. *Opt. Lett.*, 31(14):2169–2171, Jul 2006.

[48] Durdu Ö. Güney, Thomas Koschny, and Costas M. Soukoulis. Reducing ohmic losses in metamaterials by geometric tailoring. *Phys. Rev. B*, 80:125129, Sep 2009.

[49] S. Anantha Ramakrishna and J. B. Pendry. Removal of absorption and increase in resolution in a near-field lens via optical gain. *Phys. Rev. B*, 67:201101, May 2003.

[50] Zhang, J., Jiang, H., Gralak, B., Enoch, S., Tayeb, G., and Lequime, M. Compensation of loss to approach –1 effective index by gain in metal-dielectric stacks. *Eur. Phys. J. Appl. Phys.*, 46(3):32603, 2009.

[51] Mark I. Stockman. Criterion for negative refraction with low optical losses from a fundamental principle of causality. *Phys. Rev. Lett.*, 98:177404, Apr 2007.

[52] Mehdi Sadatgol, K. Özdemir, Lan Yang, and Durdu Ö. Güney. Plasmon injection to compensate and control losses in negative index metamaterials. *Phys. Rev. Lett.*, 115:035502, Jul 2015.

[53] Muhammad I. Aslam and Durdu Ö. Güney. Surface plasmon driven scalable low-loss negative-index metamaterial in the visible spectrum. *Phys. Rev. B*, 84:195465, Nov 2011.

[54] Durdu Ö Güney, Thomas Koschny, and Costas M Soukoulis. Surface plasmon driven electric and magnetic resonators for metamaterials. *Physical Review B*, 83(4):045107, 2011.

[55] Muhammad I Aslam and Durdu Ö Güney. Dual-band, double-negative, polarization-independent metamaterial for the visible spectrum. *JOSA B*, 29(10):2839–2847, 2012.

[56] Wyatt Adams, Mehdi Sadatgol, Xu Zhang, and Durdu Ö Güney. Bringing the 'perfect lens' into focus by near-perfect compensation of losses without gain media. *New Journal of Physics*, 18(12):125004, 2016.

[57] Ting Xu, Amit Agrawal, Maxim Abashin, Kenneth J. Chau, and Henri J. Lezec. All-angle negative refraction and active flat lensing of ultraviolet light. *Nature*, 497(7450):470–474, 2013.

[58] Carlos García-Meca, Juan Hurtado, Javier Martí, Alejandro Martínez, Wayne Dickson, and Anatoly V. Zayats. Low-loss multilayered metamaterial exhibiting

a negative index of refraction at visible wavelengths. *Phys. Rev. Lett.*, 106:067402, Feb 2011.

[59] Ewold Verhagen, René de Waele, L. Kuipers, and Albert Polman. Three-dimensional negative index of refraction at optical frequencies by coupling plasmonic waveguides. *Phys. Rev. Lett.*, 105:223901, Nov 2010.

[60] Yulu Chen, Yu-Chun Hsueh, Mengren Man, and Kevin J. Webb. Enhanced and tunable resolution from an imperfect negative refractive index lens. *J. Opt. Soc. Am. B*, 33(3):445–451, Mar 2016.

[61] Robert D. Fiete and Theodore Tantalo. Comparison of snr image quality metrics for remote sensing systems. *Optical Engineering*, 40(4):574–585, 2001.

[62] Miles N Wernick, Oliver Wirjadi, Dean Chapman, Zhong Zhong, Nikolas P Galatsanos, Yongyi Yang, Jovan G Brankov, Oral Oltulu, Mark A Anastasio, and Carol Muehleman. Multiple-image radiography. *Physics in Medicine and Biology*, 48(23):3875, 2003.

[63] Gary T. Barnes. Radiographic mottle: A comprehensive theory. *Medical Physics*, 9(5):656–667, 1982.

[64] Zhen Guo, Qizhao Huang, Changtao Wang, Ping Gao, Wei Zhang, Zeyu Zhao, Lianshan Yan, and Xiangang Luo. Negative and positive impact of roughness and loss on subwavelength imaging for superlens structures. *Plasmonics*, 9(1):103–110, 2014.

[65] Haogang Wang, J. Quinn Bagley, Leung Tsang, Shaowu Huang, Kung-Hau Ding, and Akira Ishimaru. Image enhancement for flat and rough film plasmon super-lenses by adding loss. *J. Opt. Soc. Am. B*, 28(10):2499–2509, Oct 2011.

[66] Hong Liu, Bing Wang, Lin Ke, Jie Deng, Chan Chum Choy, Ming Sheng Zhang, Lu Shen, Stefan A. Maier, and Jing Hua Teng. High contrast superlens lithography engineered by loss reduction. *Advanced Functional Materials*, 22(18):3777–3783, 2012.

[67] Gerald C. Holst. *CCD arrays, cameras, and displays.* SPIE Optical Engineering Press, 2000.

[68] John F. Walkup and Robert C. Choens. Image processing in signal-dependent noise. *Optical Engineering*, 13(3):133258–133258, 1974.

[69] John J. Heine and Madhusmita Behera. Aspects of signal-dependent noise char-acterization. *J. Opt. Soc. Am. A*, 23(4):806–815, Apr 2006.

[70] Rangachar Kasturi, John F. Walkup, and Thomas F. Krile. Image restoration by transformation of signal-dependent noise to signal-independent noise. *Appl. Opt.*, 22(22):3537–3542, Nov 1983.

[71] Gary K. Froehlich, John F. Walkup, and Thomas F. Krile. Estimation in signal-dependent film-grain noise. *Appl. Opt.*, 20(20):3619–3626, Oct 1981.

[72] Makoto Akiba, Kenji Tsujino, and Masahide Sasaki. Ultrahigh-sensitivity single-photon detection with linear-mode silicon avalanche photodiode. *Opt. Lett.*, 35(15):2621–2623, Aug 2010.

[73] Zeyu Zhao, Yunfei Luo, Na Yao, Wei Zhang, Changtao Wang, Ping Gao, Cheng-wei Zhao, Mingbo Pu, and Xiangang Luo. Modeling and experimental study of plasmonic lens imaging with resolution enhanced methods. *Opt. Express*, 24(24):27115–27126, Nov 2016.

[74] Alexander V. Kildishev, Alexandra Boltasseva, and Vladimir M. Shalaev. Planar photonics with metasurfaces. *Science*, 339(6125), 2013.

[75] Anders Pors, Michael G. Nielsen, René Lynge Eriksen, and Sergey I. Bozhevolnyi. Broadband focusing flat mirrors based on plasmonic gradient metasurfaces. *Nano Letters*, 13(2):829–834, 2013.

[76] Yang Zhao and Andrea Alù. Manipulating light polarization with ultrathin plasmonic metasurfaces. *Phys. Rev. B*, 84:205428, Nov 2011.

[77] Nanfang Yu, Patrice Genevet, Mikhail A. Kats, Francesco Aieta, Jean-Philippe Tetienne, Federico Capasso, and Zeno Gaburro. Light propagation with phase discontinuities: Generalized laws of reflection and refraction. *Science*, 334(6054):333–337, 2011.

[78] Yun Xu, Jingbo Sun, Wiktor Walasik, and Natalia M. Litchinitser. Probing

metamaterials with structured light. *Opt. Express*, 24(23):26249–26254, Nov 2016.

[79] David R Smith, David Schurig, Marshall Rosenbluth, Sheldon Schultz, S Anantha Ramakrishna, and John B Pendry. Limitations on subdiffraction imaging with a negative refractive index slab. *Applied Physics Letters*, 82(10):1506–1508, 2003.

[80] Shun Cao, Taisheng Wang, Qiang Sun, Bingliang Hu, and Weixing Yu. Meta-nanocavity model for dynamic super-resolution fluorescent imaging based on the plasmonic structure illumination microscopy method. *Opt. Express*, 25(4):3863–3874, Feb 2017.

[81] Carlo Rizza, Alessandro Ciattoni, Elisa Spinozzi, and Lorenzo Columbo. Terahertz active spatial filtering through optically tunable hyperbolic metamaterials. *Opt. Lett.*, 37(16):3345–3347, Aug 2012.

[82] David Schurig and David R Smith. Spatial filtering using media with indefinite permittivity and permeability tensors. *Applied Physics Letters*, 82(14):2215–2217, 2003.

[83] B Wood, JB Pendry, and DP Tsai. Directed subwavelength imaging using a layered metal-dielectric system. *Physical Review B*, 74(11):115116, 2006.

[84] Patrice Genevet, Federico Capasso, Francesco Aieta, Mohammadreza Khorasa-ninejad, and Robert Devlin. Recent advances in planar optics: from plasmonic to dielectric metasurfaces. *Optica*, 4(1):139–152, Jan 2017.

[85] Carl Pfeiffer and Anthony Grbic. Metamaterial huygens' surfaces: tailoring wave fronts with reflectionless sheets. *Physical review letters*, 110(19):197401, 2013.

[86] Christopher L Holloway, Edward F Kuester, Joshua A Gordon, John O'Hara, Jim Booth, and David R Smith. An overview of the theory and applications of metasurfaces: The two-dimensional equivalents of metamaterials. *IEEE Antennas and Propagation Magazine*, 54(2):10–35, 2012.

[87] K. Hirakawa. Fourier and filterbank analyses of signal-dependent noise. In *2008 IEEE International Conference on Acoustics, Speech and Signal Processing*, pages 3517–3520, March 2008.

[88] Xu Zhang, Wyatt Adams, Mehdi Sadatgol, and Durdu Ö Güney. Enhancing the resolution of hyperlens by the compensation of losses without gain media. *Progress in Electromagnetic Research C*, 70:1–7, 2016.

[89] Xu Zhang, Sanjoy Debnath, and Durdu Ö Güney. Hyperbolic metamaterial feasible for fabrication with direct laser writing processes. *JOSA B*, 32(6):1013–1021, 2015.

[90] Costas M Soukoulis and Martin Wegener. Optical metamaterials—more bulky and less lossy. *Science*, 330(6011):1633–1634, 2010.

[91] Costas M Soukoulis and Martin Wegener. Past achievements and future challenges in the development of three-dimensional photonic metamaterials. *Nature Photonics*, 5(9):523–530, 2011.

[92] Durdu Ö Güney, Thomas Koschny, Maria Kafesaki, and Costas M Soukoulis. Connected bulk negative index photonic metamaterials. *Optics letters*, 34(4):506–508, 2009.

[93] Durdu Ö Güney, Thomas Koschny, and Costas M Soukoulis. Intra-connected three-dimensionally isotropic bulk negative index photonic metamaterial. *Optics express*, 18(12):12348–12353, 2010.

[94] Scott Michael Rudolph and Anthony Grbic. A broadband three-dimensionally isotropic negative-refractive-index medium. *IEEE Transactions on Antennas and Propagation*, 60(8):3661–3669, 2012.

[95] Sui Yang, Xingjie Ni, Boubacar Kante, Jie Zhu, Kevin O'Brien, Yuan Wang, and Xiang Zhang. Experimental demonstration of optical metamaterials with isotropic negative index. In *Lasers and Electro-Optics (CLEO), 2016 Conference on*, pages 1–2. IEEE, 2016.

Chapter 3

Enhanced superlens imaging with loss-compensating hyperbolic near-field spatial filter[1]

Controlling the interaction of light with metamaterials (MM) has instigated potentially revolutionary applications such as imaging beyond diffraction limit [1, 2, 3, 4], perfect absorbers [5], invisibility cloaks [6], and many others [7, 8]. However, especially in the visible spectrum, MMs have significant dissipative losses in their constituent metallic structures that dampen the coupled electron-light oscillations (i.e., surface plasmon polaritons (SPPs)). In the context of superresolution imaging, losses limit the resolution of "superlenses" hindering their advantages in applications such as nanoimaging and nanolithography [9, 10]. Loss compensation schemes involving non-linear effects [11] and electrically or optically pumped gain media [12, 13, 14] were developed. Although these approaches have shown substantial promise at optical frequencies, their usefulness has been limited in imaging. This is because preserving the amplitude and phase relationships between fields in time and space is difficult with gain-assisted MMs due to the stability and gain saturation issues that can lead to significant noise amplification [15].

Our approach to loss compensation employs an "auxiliary source," which injects SPPs to amplify the local SPPs of a plasmonic MM. The technique was initially conceptualized for a single wavevector in [16]. An auxiliary source capable of amplifying an arbitrary wavevector was also envisioned and loss compensation scheme was named the "plasmon-injection" or Π scheme. Theoretical studies later showed that the technique is similar to a linear deconvolution [17] capable of enhancing [17, 18, 19, 20] the resolution limits of previously studied near-field imaging systems employing negative

index MMs, plasmonic lenses and hyperlenses. However, in a physical implementation of the Π scheme, a detailed understanding of the auxiliary source was necessary. These were later presented in [21] where the word "active" is used to distinguish the Π scheme from previous "passive" counterparts [17, 18, 19, 20]. It was shown that the auxiliary must provide amplification to a narrow band of high spatial frequencies to avoid amplifying noise and must be constructed by a physical convolution with the object field. Following this revelation, it was shown how a hyperbolic metamaterial (HMM) functioning as a tunable near-field spatial filter presents a possible method to construct an auxiliary source with the above properties [22].

This letter describes for the first time, a coherent light physical implementation of the active Π scheme. A HMM spatial filter is integrated into a near-field imaging system to construct the convolved auxiliary source with selective amplification capabilities and an iterative reconstruction process [21], and is used to reconstruct the image. A plasmonic imaging system operating at wavelength $\lambda = 365 \, nm$ with a $50 \, nm$ thick Ag lens is selected. The lens is located symmetrically between object and image planes separated by $100 \, nm$. This superlens is incapable of resolving subwavelength features at one-sixth of the illumination wavelength $(\lambda/6)$ primarily due to material losses and noise. Numerical calculations, performed with the finite element based software package COMSOL Multiphysics, show how the active Π scheme when implemented with the system allows the $\lambda/6$ resolution. Additionally, the reconstruction process requires no prior knowledge of the object and the concept can be extended to other

near-field imaging systems at different wavelengths.

A schematic of the Ag lens imaging system, with and without the integrated HMM spatial filter is shown in figures 3.1(a) and (b), respectively. The spatial filter is constructed by alternately stacking layers of Al with dielectrics. The imaging system is embedded inside a dielectric with relative permittivity $\epsilon_d = 2.5$ similar to an experimental Ag lens [23]. The relative permittivities of Ag and Al at $\lambda = 365\ nm$ are $\epsilon_{Ag} = -1.8752 + 0.5947i$ and $\epsilon_{Al} = -18.179 + 3.2075i$, respectively calculated from the Drude-Lorentz model [24]. The systems are excited with a transverse magnetic (TM) polarized field from the object plane and the responses are extracted as a complex magnetic field from the image plane. The object and image planes are marked by dashed lines in figures 3.1(a) and (b). Both geometries are padded with perfectly matched layers (PMLs) shown in blue while the edges of the PMLs are backed by scattering boundary conditions shown by pink lines. The extent of the geometry along the y-axis is 80λ and 9500 mesh elements are defined at each boundary parallel to the y-axis with the smallest mesh element being approximately equal to $3\ nm$. Transfer functions are calculated by using a TM point source excitation on the object plane. A Gaussian field distribution with full width at half maximum of $6\ nm$ is used to mimic the point source. Prior to all image processing calculations, noise is introduced into the measured fields from the image plane by assuming that the spatial distribution of the field is measured by a detector with an array of pixels. The signal recorded at each pixel is distorted by a combination of signal dependent (SD) and
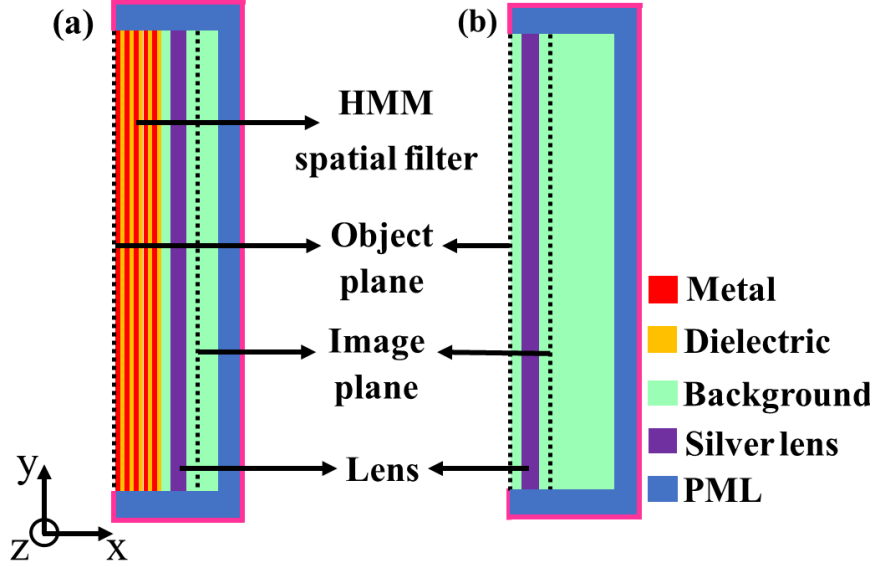
Figure 3.1: The geometry of the imaging system (a) with and (b) without the integrated spatial filter (not to scale). In the Π scheme, the object plane in (a) is illuminated by a high-intensity (above 1 $mW/\mu m^2$) plane wave. The resultant field in the image plane is then deconvolved to use in the reconstruction of the high resolution image. This process is equivalent to superimposing the object field in the object plane in (b) with a loss compensating auxiliary field followed by the deconvolution. The transfer functions are calculated from the field distributions on the image planes using point source excitations on the object planes. The HMM image plane is assumed to be the last interface. In all the imaging processes, spatial random noise is added in the image planes before any post-processing.

signal independent (SI) noise processes. The corresponding noisy image is calculated according to the "signal-modulated noise" model [25, 26, 27], employed previously in [21]. This work uses $0.025I(y)$ A/m and 0.005 A/m for the standard deviations of SD and SI noise, respectively and $I(y)$ is the spatial distribution of the noiseless or ideal signal on the image plane. Note that these values have larger standards than an experimental optical detector [28] and are selected to highlight the adequacy of the active Π scheme in noisy systems.

The efficacy of the active Π scheme in imaging is exemplified with an arbitrary object with 3 Gaussian features separated by $\lambda/6$. The object is defined as a real TM polarized field on the object plane (see figure 3.1). In a physical imaging system, no prior knowledge of the object will be available. Therefore, only the raw data from the image plane is used to pinpoint the spatial frequency at which the first instance of the auxiliary source should be applied. For this purpose, the Ag lens without the integrated spatial filter (see figure 3.1(b)) is used to image the object field. The measured amplitude and phase of the raw image are corrupted with noise and are shown by the green lines in figures 3.2(a) and (b), respectively. It is evident that the Ag lens is incapable of resolving the object shown by the black line in figure 3.2(a). The amplitude of the Fourier transforms of the object and the raw image are shown in figure 3.2(c) while figure 3.2(d) shows the contributions of the SD and SI noise. Figure 3.2(c) shows how the losses and noise progressively degrade the image spectrum beyond $k_y \approx 2k_0$, where k_0 is the free-space wavenumber. Eventually, the image spectrum is completely overwhelmed by the noise and cannot be recovered by passive deconvolution or increased illumination intensity since both processes proportionally amplify noise [21]. In conclusion, a selective amplification with the auxiliary must be initiated from $k_y \approx 2k_0$ and progressively moved to higher spatial frequencies. Note that the Fourier spectra in figures 3.2(c) and (d) are truncated at $k_y = 7k_0$ because the calculated transfer function loses accuracy beyond this point. Hence, the selective amplification process can be applied until $k_y = 7k_0$. One important reason for the
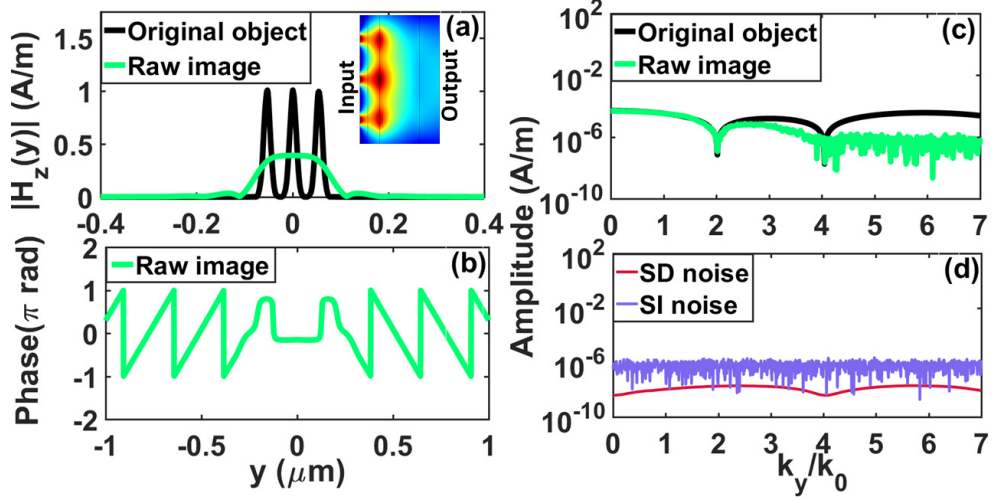
Figure 3.2: (a) Amplitude of the magnetic field distribution of the object and the raw image from the object and image planes (see figure 3.1(b)). The inset shows the two-dimensional (2D) pattern of the magnetic field amplitude along the imaging system. (b) The phase of the magnetic field of the raw image. The object is purely real and has zero phase. (c) The amplitude of the Fourier transform of the object and the raw image. (d) The contributions of the SD and SI noise to the raw image.

failure of the numerically calculated transfer function is the finite spatial extent of the image and object planes which introduces errors in the Fourier transforms due to the sharp truncation of the fields [21].

In order to design an auxiliary source to cover the spectral band $2k_0 \leq k_y \leq 7k_0$, tunable HMM spatial filters with pass-bands within this range will be used below. The pass-band of the HMM spatial filter can be tuned by changing the relative permittivity of the constituent dielectric layer and the filling fraction, because this shifts the type II hyperbolic dispersion of the filters [22]. Six HMM spatial filters are designed to cover the above range. The design parameters are listed in table 3.1. The metallic layer is set to Al and the overall thickness of the HMMs are kept constant at 365 nm

for consistency. The relative permittivities for the dielectrics listed in table 3.1 at $\lambda = 365 \ nm$ are obtained from [29, 30, 31, 32, 33, 34]. The amplitude and phase of the complex transfer function corresponding to the HMM spatial filters are shown in figures 3.3(a) and (b), respectively.

Table 3.1
Design parameters of the HMM spatial filters.

Dielectric	Relative permittivity	Number of unit cells	Filling fraction
SiO_2	2.2147	10	0.65
Al_2O3	3.18587	10	0.65
Si_3N_4	4.05373	10	0.65
ZrO_2	5.06205	10	0.65
MoO_3	$6.031 + 1.1908i$	10	1.1
TiO_2	$8.2886 + 0.10186i$	12	1.1
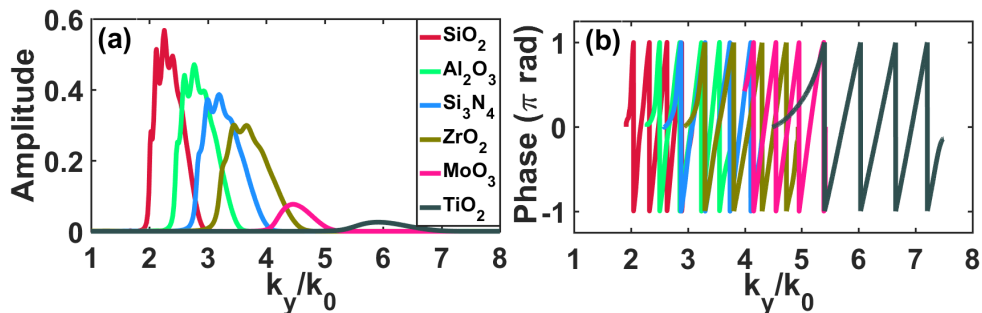
Figure 3.3: (a) Amplitude and (b) phase of the transfer function of each HMM spatial filter. The phase plot shows only the region of high transmission since the calculated phase is irrelevant and not reliable outside the pass-band of the filter due to poor transmission.

It is instructive to illustrate the effect of selective amplification with an auxiliary source with one filter-lens system. Therefore, we first select the integrated $Al - ZrO_2$ HMM spatial filter (see figure 3.3(a)). The object is illuminated with a high intensity (about $700 \ mW/\mu m^2$) coherent light source and then imaged with the integrated

system. The corresponding image measured by the detector is called the *"active image."* The amplitude and phase of the active image are shown in figures 3.4(a) and (b), respectively. The Fourier transform of the active image and the object spectrum are shown by dark green and black lines, respectively, in figure 3.4(c). Figure 3.4(d) shows the contribution of the SD noise. Comparing the active image spectrum in figure 3.4(c) with the raw image spectrum in figure 3.2(c), it is evident that the noise is not visible in the active image spectrum within the pass-band of the $Al-ZrO_2$ spatial filter. However, the raw image spectrum is predominantly noisy in the same spectral band. Additionally, the active image spectrum also shows a node at $k_y = 4k_0$ which is not detectable in the raw image spectrum. Since the missing Fourier component is within the pass-band of the filter, we must conclude that the node is a feature of the object which was previously buried under the noise. Importantly, the SD noise level for the integrated $Al-ZrO_2$ HMM spatial filter does not increase at the same rate as the input field (compare the dark green solid line in figure 3.4(d) and red solid line in 3.2(d)) due to the nontrivial superposition of the pass-band spatial frequencies with other frequencies in the image plane in the presence of spatial random noise. Similar behavior is observed with the other filters (only three are shown in figure 3.4 for clarity). This is the essence of how the selective amplification with the auxiliary source allows us to recover the object features with little noise amplification.

After determining the active image spectrum for each filter-lens integrated system, the final step is a post-processing technique where the noisy portions of the raw image
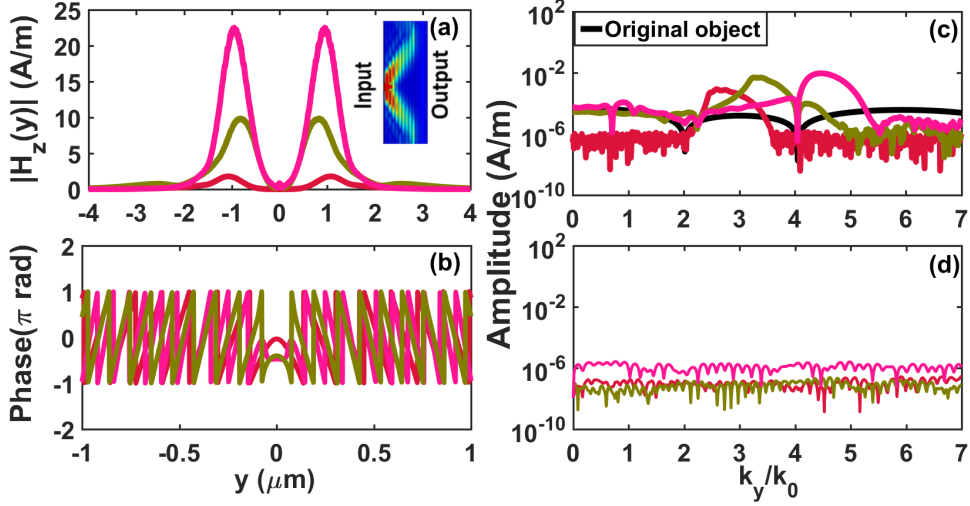
Figure 3.4: (a) Amplitude and (b) phase of the magnetic field distribution of the active images with different filters. The same color code as in figure 3.3 is used for the filters. The inset in (a) shows the 2D pattern of the magnetic field amplitude along the integrated imaging system using the $Al - SiO_2$ filter. (c) The amplitudes of the Fourier transforms of the object and the active images. (d) The contributions of the SD noise spectra.

spectrum are substituted with the noise-free portions of the relevant active image spectrum and then deconvolved with an active transfer function. The active image spectrum for the jth spatial filter is first expressed as

$$I_a^{(j)}(k_y) = H_0 T_l(k_y) P^{(j)}(k_y) O(k_y), \tag{3.1}$$

where $T_l(k_y)$, $P^{(j)}(k_y)$ are the transfer functions of the Ag lens and the $j^{(th)}$ HMM spatial filter, respectively. $O(k_y)$ is the object spectrum and H_0 is the incident plane-wave illumination amplitude. The noise-free portion of each active image spectrum

is selected by multiplying Eq. 3.1 with a rectangular function

$$
R^{(j)}(k_y) = \begin{cases} 1 & \left| \frac{k_y - k_c^{(j)}}{W^{(j)}} \right| \leq \frac{1}{2} \\ 0 & \texttt{otherwise.} \end{cases}
\tag{3.2}
$$

of width $W(j)$ and centered at $k_c^{(j)}$ defined for the jth integrated system. The equivalent portions of the raw image spectrum are substituted by the selected active image spectra. The resulting total image spectrum can be written as

$$
I^{'}(k_y) = I(k_y) \left[1 - \sum_{j=1}^{6} R^{(j)}(k_y) \right] + \sum_{j=1}^{6} I_a^{(j)}(k_y) R^{(j)}(k_y),
\tag{3.3}
$$

where $I(k_y)$ is the raw image spectrum. Similarly, the active transfer function $T_a(k_y)$ is obtained by substituting identical portions the Ag lens transfer function with the integrated system transfer function and is expressed as

$$
T_a(k_y) = T_l(k_y) \left\{ 1 - \sum_{j=1}^{6} R^{(j)}(k_y) + \sum_{j=1}^{6} H_0 P^{(j)}(k_y) R^{(j)}(k_y) \right\}.
\tag{3.4}
$$

The final reconstructed image is obtained by multiplying $I^{'}(k_y)$ from Eq. 4.2 with the inverse of the active transfer function in Eq. 3.4 (i.e., active deconvolution). $W^{(j)}$, $k_c^{(j)}$, and H_0 which were used for this reconstruction are listed in table 3.2 for each filter-lens integrated system. Note that two adjacent rectangle functions should not overlap for Eqs. 4.2 and 3.4 to be valid.

Table 3.2
Post-processing parameters

	SiO_2	Al_2O3	Si_3N_4	ZrO_2	MoO_3	TiO_2
$W^{(j)}$ (k_0)	0.949	0.476	0.456	0.369	1.145	1.882
$k_c^{(j)}$ (k_0)	2.366	3.078	3.544	3.957	4.716	6.228
H_0 (Am^{-1})	3000	3000	5000	60000	3×10^6	5×10^6

The reconstructed image spectrum obtained after the above post-processing steps is shown by the red line in figure 3.5(a). The active compensated spectrum closely follows the object spectrum shown by the black line and is almost noise-free. The raw image spectrum, shown by the green line and previously illustrated in figure 3.2(c), is significantly corrupted beyond $k_y \gg 3k_0$ and the passively compensated image spectrum, obtained by a simple deconvolution method [17, 18] shows significant noise amplification. Lastly, figure 3.5(b) compares the amplitude squared of the reconstructed fields with the original object illustrating the significant enhancement of the active Π loss compensation scheme. The lens completely fails to resolve the object and passive reconstruction is extremely unreliable due to significant noise amplification whereas, active compensation can resolve the object with a sufficiently high contrast. The effect here comes from the loss compensation mechanism implemented through the integrated system, not from the individual systems. Presently, image resolution is limited by the filter design, increasingly high power requirement, SD noise level, and accurate transfer functions.

In conclusion, we have shown how the Π loss compensation scheme when physically implemented with a near-field superlens enhances the performance of the superlens.
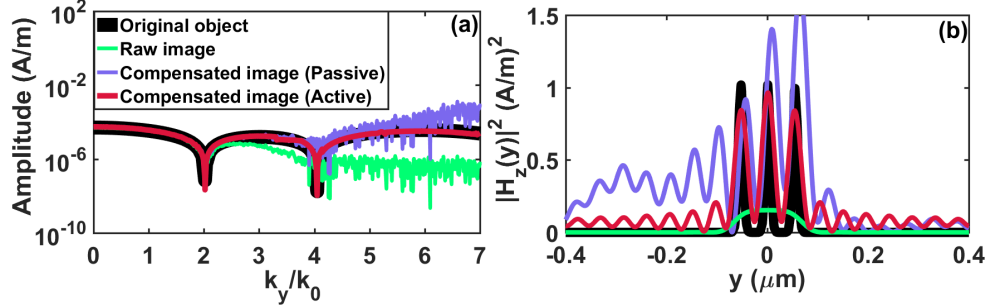
Figure 3.5: (a) Fourier spectra and (b) spatial field distributions of the reconstructed images illustrating the superiority of the active Π scheme over passive deconvolution. The imaging system is now capable of resolving objects separated by $\lambda/6$.

The introduction of a convolved auxiliary source, generated by integrating a HMM spatial filter into the system allows restoration of attenuated components of the image spectrum with little noise amplification. The proof-of-principle here can be verified experimentally with available plasmonic lenses and hyperlenses. The present implementation can be optimized for higher resolution with different near-field lenses and to operate with a single high-frequency spatial filter in near real-time at different wavelengths. We believe this work brings us closer to overcoming losses in near-field imaging and elevates the possibility of realizing a "perfect lens" first envisioned by Pendry. Finally, consistent with this letter, we noticed that in three other independent works HMM spatial filters either alone or integrated with a superlens cavity and a type I HMM were recently used to achieve pattern uniformity in lithography [35], high-resolution Bessel beam [36], and hyperbolic dark-field lens [37], respectively.

References

[1] J. B. Pendry. Negative refraction makes a perfect lens. *Phys. Rev. Lett.*, 85:3966–3969, Oct 2000.

[2] Pavel A Belov and Yang Hao. Subwavelength imaging at optical frequencies using a transmission device formed by a periodic layered metal-dielectric structure operating in the canalization regime. *Phys. Rev. B*, 73(11):113110, 2006.

[3] Zhaowei Liu, Hyesog Lee, Yi Xiong, Cheng Sun, and Xiang Zhang. Far-field optical hyperlens magnifying sub-diffraction-limited objects. *Science*, 315(5819):1686–1686, 2007.

[4] Heng-He Tang and Pu-Kun Liu. Long-distance super-resolution imaging assisted by enhanced spatial fourier transform. *Opt. Express*, 23(18):23613–23623, 2015.

[5] Koray Aydin, Vivian E Ferry, Ryan M Briggs, and Harry A Atwater. Broadband polarization-independent resonant light absorption using ultrathin plasmonic super absorbers. *Nat. Commun.*, 2:1528, 2011.

[6] John Pendry. Optics: All smoke and metamaterials. *Nature*, 460(7255):579–580, 2009.

[7] Huaping Wang, Yangyang Deng, Bin Zheng, Rujiang Li, Yuyu Jiang, Shahram Dehdashti, Zhiwei Xu, and Hongsheng Chen. Panoramic lens designed with transformation optics. *Sci. Rep*, 7:40083, 2017.

[8] Lian Shen, Ludmila J Prokopeva, Hongsheng Chen, and Alexander V Kildishev. Designing optimal nanofocusing with a gradient hyperlens. *Nanophotonics*, 7(2):479–487, 2017.

[9] Changtao Wang, Ping Gao, Zeyu Zhao, Na Yao, Yanqin Wang, Ling Liu, Kaipeng Liu, and Xiangang Luo. Deep sub-wavelength imaging lithography by a reflective plasmonic slab. *Opt. Express*, 21(18):20683–20691, 2013.

[10] Ping Gao, Na Yao, Changtao Wang, Zeyu Zhao, Yunfei Luo, Yanqin Wang, Guohan Gao, Kaipeng Liu, Chengwei Zhao, and Xiangang Luo. Enhancing aspect profile of half-pitch 32 nm and 22 nm lithography with plasmonic cavity lens. *Appl. Phys. Lett*, 106(9):093110, 2015.

[11] Alexander K. Popov and Vladimir M. Shalaev. Compensating losses in negative-index metamaterials by optical parametric amplification. *Opt. Lett.*, 31(14):2169–2171, Jul 2006.

[12] S Anantha Ramakrishna and John B Pendry. Removal of absorption and increase

in resolution in a near-field lens via optical gain. *Phys. Rev. B*, 67(20):201101, 2003.

[13] MA Vincenti, D de Ceglia, V Rondinone, A Ladisa, A D'Orazio, MJ Bloemer, and M Scalora. Loss compensation in metal-dielectric structures in negative-refraction and super-resolving regimes. *Phys. Rev. A*, 80(5):053807, 2009.

[14] Shumin Xiao, Vladimir P Drachev, Alexander V Kildishev, Xingjie Ni, Uday K Chettiar, Hsiao-Kuan Yuan, and Vladimir M Shalaev. Loss-free and active optical negative-index metamaterials. *Nature*, 466(7307):735, 2010.

[15] Costas M Soukoulis and Martin Wegener. Optical metamaterials—more bulky and less lossy. *Science*, 330(6011):1633–1634, 2010.

[16] Mehdi Sadatgol, Şahin K Özdemir, Lan Yang, and Durdu Ö Güney. Plasmon injection to compensate and control losses in negative index metamaterials. *Phys. Rev. Lett.*, 115(3):035502, 2015.

[17] Wyatt Adams, Anindya Ghoshroy, and Durdu Ö. Güney. Plasmonic superlens image reconstruction using intensity data and equivalence to structured light illumination for compensation of losses. *J. Opt. Soc. Am. B*, 34(10):2161–2168, Oct 2017.

[18] Wyatt Adams, Mehdi Sadatgol, Xu Zhang, and Durdu Ö Güney. Bringing the 'perfect lens' into focus by near-perfect compensation of losses without gain media. *New J. Phys*, 18(12):125004, 2016.

[19] Xu Zhang, Wyatt Adams, Mehdi Sadatgol, and Durdu Ö Güney. Enhancing the resolution of hyperlens by the compensation of losses without gain media. *Prog. Electromagn. Res. C*, 70:1–7, 2016.

[20] Xu Zhang, Wyatt Adams, and Durdu Ö. Güney. Analytical description of inverse filter emulating the plasmon injection loss compensation scheme and implementation for ultrahigh-resolution hyperlens. *J. Opt. Soc. Am. B*, 34(6):1310–1318, Jun 2017.

[21] Anindya Ghoshroy, Wyatt Adams, Xu Zhang, and Durdu Ö. Güney. Active plasmon injection scheme for subdiffraction imaging with imperfect negative index flat lens. *J. Opt. Soc. Am. B*, 34(7):1478–1488, Jul 2017.

[22] Anindya Ghoshroy, Xu Zhang, Wyatt Adams, and Durdu Ö Güney. Hyperbolic metamaterial as a tunable near-field spatial filter for the implementation of the active plasmon injection loss compensation scheme. *arXiv preprint arXiv:1710.07166*, 2017.

[23] Nicholas Fang, Hyesog Lee, Cheng Sun, and Xiang Zhang. Sub–diffraction-limited optical imaging with a silver superlens. *Science*, 308(5721):534–537, 2005.

[24] Aleksandar D Rakić, Aleksandra B Djurišić, Jovan M Elazar, and Marian L Majewski. Optical properties of metallic films for vertical-cavity optoelectronic devices. *Appl. Opt.*, 37(22):5271–5283, 1998.

[25] John F. Walkup and Robert C. Choens. Image processing in signal-dependent noise. *Opt. Eng.*, 13(3):133258–133258, 1974.

[26] John J. Heine and Madhusmita Behera. Aspects of signal-dependent noise characterization. *J. Opt. Soc. Am. A*, 23(4):806–815, Apr 2006.

[27] Gary K. Froehlich, John F. Walkup, and Thomas F. Krile. Estimation in signal-dependent film-grain noise. *Appl. Opt.*, 20(20):3619–3626, Oct 1981.

[28] Makoto Akiba, Kenji Tsujino, and Masahide Sasaki. Ultrahigh-sensitivity single-photon detection with linear-mode silicon avalanche photodiode. *Opt. Lett.*, 35(15):2621–2623, Aug 2010.

[29] Lihong Gao, Fabien Lemarchand, and Michel Lequime. Exploitation of multiple incidences spectrometric measurements for thin film reverse engineering. *Opt. Express*, 20(14):15734–15751, Jul 2012.

[30] Raymond L. Kelly. Program of the 1972 annual meeting of the optical society of america. *J. Opt. Soc. Am.*, 62(11):1336–1336, Nov 1972.

[31] Kevin Luke, Yoshitomo Okawachi, Michael R. E. Lamont, Alexander L. Gaeta, and Michal Lipson. Broadband mid-infrared frequency comb generation in a si3n4 microresonator. *Opt. Lett.*, 40(21):4823–4826, Nov 2015.

[32] D. L. Wood and K. Nassau. Refractive index of cubic zirconia stabilized with yttria. *Appl. Opt.*, 21(16):2978–2981, Aug 1982.

[33] L. Lajaunie, F. Boucher, R. Dessapt, and P. Moreau. Strong anisotropic influence of local-field effects on the dielectric response of α-moo$_3$. *Phys. Rev. B*, 88:115141, Sep 2013.

[34] Thomas Siefke, Stefanie Kroker, Kristin Pfeiffer, Oliver Puffky, Kay Dietrich, Daniel Franta, Ivan Ohlídal, Adriana Szeghalmi, Ernst-Bernhard Kley, and Andreas Tünnermann. Materials pushing the application limits of wire grid polarizers further into the deep ultraviolet spectral range. *Adv. Opt. Mater.*, 4(11):1780–1786, 2016.

[35] Gaofeng Liang, Xi Chen, Qing Zhao, and L Jay Guo. Achieving pattern uniformity in plasmonic lithography by spatial frequency selection. *Nanophotonics*, 7(1):277–286, 2018.

[36] Ling Liu, Ping Gao, Kaipeng Liu, Weijie Kong, Zeyu Zhao, Mingbo Pu, Changtao Wang, and Xiangang Luo. Nanofocusing of circularly polarized bessel-type plasmon polaritons with hyperbolic metamaterials. *Materials Horizons*, 4(2):290–296, 2017.

[37] Lian Shen, Huaping Wang, Rujiang Li, Zhiwei Xu, and Hongsheng Chen. Hyperbolic-polaritons-enabled dark-field lens for sensitive detection. *Sci. Rep*, 7(1):6995, 2017.

Chapter 4

Hyperbolic metamaterial as a tunable near-field spatial filter to implement active plasmon-injection loss compensation[1]

---

[1]Reproduced from A. Ghoshroy, W. Adams, X. Zhang, and D. O. Guney, "Hyperbolic metamaterial as a tunable near-field spatial filter to implement active plasmon-injection loss compensation," *Phys. Rev. Applied* 10, 024018 (2018); doi:10.1103/PhysRevApplied.10.024018. ©2020 by the American Physical Society.

4.1 Introduction

Our ability to control electromagnetic fields with metamaterials has flourished since the turn of the century and has in turn engendered a myriad of previously unthought of applications. As opposed to the electromagnetic properties of naturally occurring materials, the properties of metamaterials stem primarily from their subwavelength structural details rather than their chemical properties alone. By carefully controlling these subwavelength features, one can fabricate an artificial material with electromagnetic properties which are very rare and sometimes impossible to find in nature. One important application of metamaterials is in the field of near-field superlensing. The near-field optics coupled with plasmonics and metamaterials has a wide range of implications from subdiffraction imaging [1] to enhanced absorption [2, 3, 4]. In the context of imaging, the near-field contains information about the subwavelength features of an object and is evanescent in nature. Pendry envisioned [5] that a slab of negative index material (NIM) can be used to amplify these evanescent waves and renewed interest in the obscure idea of NIMs first conceived by Veselago [6] in the late 1960s.

In the years that followed, a NIM was realized [7] for the first time by Shelby, et al. followed by the demonstration of a near-field superlens that exhibits imaging beyond the diffraction limit [8, 9]. Subsequently, it was realized that the presence of inherent

material losses substantially degrade the performance of superlenses [10, 11, 12]. A robust loss compensation scheme was clearly necessary and in the ideal case should be completely independent of the object. Efforts to overcome this problem led to the development of new approaches at loss compensation which employed gain medium [13, 14, 15], non-linear effects [16], and geometric tailoring [17]. However, these approaches introduced additional complexities, such as pump requirement, stability, and gain saturation issues, among others, which are crucial especially for imaging applications.

We have been attempting to develop a new loss compensation scheme, with no above complexities, where the goal is to use an external *"auxiliary"* illumination to compensate losses in the material. This was initially conceptualized in [18], where the losses suffered by a normally incident wave were compensated by a coherent superposition with an auxiliary field. Although the method was studied in detail for a single wavevector, it inspired two important questions. If one could develop a similar technique, where an auxiliary source provides compensation for a large band of wavevectors, would it be possible to perfectly reconstruct the original object in an imaging scenario without having any prior knowledge of the object? If so, could the technique be applied to different near-field imaging systems such as those employing NIMs or plasmonic lenses using, for example, silver [19] and silicon carbide (SiC) [20], or hyperlenses [21] under both coherent and incoherent illumination? In [18], we used the name "plasmon-injection (Π) scheme," referring to the above form of

loss compensation which employs an external auxiliary source to amplify the decayed Fourier components propagating inside the lossy plasmonic metamaterial (see figure 4.1a). It has been envisioned that the amplitude of each Fourier component to be provided by the auxiliary could be estimated from the transfer function of the imaging system. Subsequent efforts were directed at answering the second question. It was demonstrated theoretically that the technique in general could be applied to different imaging systems to improve their resolution limits [22, 23, 24, 25]. However, no physical auxiliary source was considered. It was simply assumed that one already has the means to amplify an arbitrary Fourier component as proposed in [18]. Before attempting to physically realize the auxiliary source, it was important to understand what properties the auxiliary should possess in order to compensate losses in a realistic noisy imaging system. Continuing efforts [26] showed that the auxiliary must provide "selective amplification" to a narrow-band of high-frequency Fourier components to avoid large noise amplification. Additionally, to recover Fourier components of the object buried in the noise, the auxiliary source has to be constructed by the physical convolution of the object field.

In this work, we show that metal-dielectric systems with a hyperbolic dispersion operating as a tunable spatial filter can be used to construct the auxiliary source and preserve the necessary characteristics shown in [26] (see figure 4.1b). Selective amplification property relies on the selective spatial filter functionality of such physical systems. Since the auxiliary is to be applied in the deep subwavelength region in the
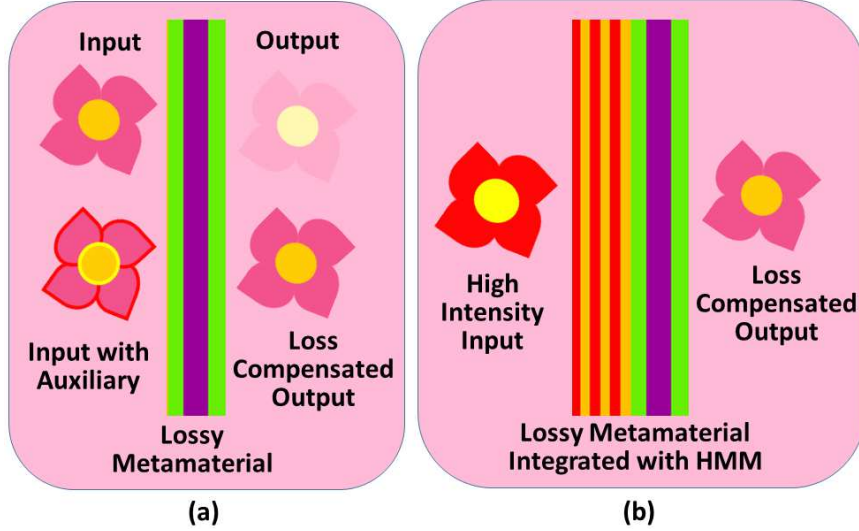
Figure 4.1: Implementations of active Π scheme. (a) In general, a desired input (upper left) cannot be faithfully transferred through a passive metamaterial due to optical losses and noise. However, in the Π scheme, the input is actively superimposed with a correlated auxiliary source (lower left) to compensate the losses, hence the output can be produced with a high fidelity. (b) This superposition process can be equivalently implemented by integrating the lossy metamaterial with a hyperbolic metamaterial (HMM) while simply elevating the illumination intensity. In both cases, with either two sources in (a) or a single source in (b), linear transmission through passive metamaterials is considered. The term "active" refers to physically adding energy to the input desired to be transferred.

reciprocal space, the spatial filter is designed to strongly suppress the propagating modes while allowing the transmission of a tunable band of evanescent modes. Layered metal-dielectric systems with hyperbolic dispersion are one possible solution for such spatial filters since they are known to support wavevectors with large transversal components exceeding the diffraction limit. This is due to the presence of coupled surface plasmon polariton (SPP) modes at the interfaces. By modifying the permittivities of the constituent materials one can control the eigenmodes supported by the system.

4.2 Theory

In section II.A, we briefly frame the essential mathematical properties of the active Π loss compensation scheme [26] by envisaging a possible physical system to realize described in section II.B. Throughout this paper we consider plane waves propagating in the xy-plane. The wavevector component k_y represents a spatial variation along the transversal direction and the wavevector component $k_z = 0$. Therefore, by looking at the sign of k_x^2 one can distinguish between the propagating and evanescent modes.

4.2.1 Active Π loss compensation scheme

The auxiliary source is essential to the active Π loss compensation scheme since it is the means with which appropriate levels of amplification are applied to the fields which suffer attenuation while propagating through a lossy metamaterial. It is important to emphasize that the term "active" refers to physically adding energy to the system (see figure 4.1). Still, linear transmission through passive metamaterials is considered. This is in a sense analogous to well-known active imaging and distinguishes the active Π scheme from deconvolution-only based implementations [22, 23, 24, 25], where no external physical energy is involved. Let $H_i(y)$ be the spatial distribution of an input field incident on a lossy metamaterial. The auxiliary source is constructed during

a convolution process between the input field and a function $A(y)$ whose Fourier transform, $A(k_y) = \mathcal{F}[A(y)]$ is

$$A(k_y) = 1 + A_0 G(k_y), \tag{4.1}$$

where $G(k_y)$ is a Gaussian centered at $k_y = k_c$ and A_0 is a constant. The convolved input field distribution has a selectively amplified Fourier spectrum provided that the second term in Eq. 4.1 is larger than 1 for some bandwidth. The amplification is controlled by the scaling factor A_0, while the central frequency and the bandwidth are tuned by the Gaussian function. In the Fourier domain, the auxiliary source is defined as the product of $H_i(k_y)$ with $A_0 G(k_y)$ (i.e., the second term in the Fourier domain). The modified incident field is then propagated through a lossy metamaterial structure which has a transfer function $T(k_y)$. The resulting output field distribution $H_o(y)$ has the Fourier spectrum

$$H_o(k_y) = H_i(k_y)[1 + A_0 G(k_y)]T(k_y). \tag{4.2}$$

The term $H_i(k_y)A_0 G(k_y)T(k_y)$ in Eq. 4.2 represents the selectively amplified spectrum measured at the output plane. In [26] this concept was proposed for a lossy NIM structure in the presence of realistic noise. An iterative loss-compensation scheme was developed where the auxiliary source was tuned to different high spatial frequencies and the amplification provided to each selected spatial frequency was controlled by

A_0. It was shown that this compensation scheme can account for material losses in the NIM structure while inhibiting the noise amplification. However, a possible physical implementation of this concept requires designing a metamaterial which can structure the input field in above described manner. The metamaterial should have a transmission shape similar to Eq. 4.1 and its response should be shift invariant in the plane perpendicular to the optical axis. A system is said to have shift invariance along a plane if its response to a point source excitation changes only in spatial position on that plane but not in functional form, as the point source traverses the input plane. This is necessary because to generate the auxiliary source, the incident field must be convolved with $A(y)$. Additionally, the metamaterial should have a relatively high transmission peak at a tunable centre frequency and low transmission on either side especially in the lower spatial frequencies. Therefore, the metamaterial should possess the characteristics of a tunable and high selectivity band-pass filter for high spatial frequencies. Since the transfer function of a passive physical system cannot easily take the mathematically convenient form in Eq. 4.1, one needs a metric to determine how closely a passive physical system can emulate the ideal one. As will be justified later, we assume that the transfer function of the realistic passive physical system is given by

$$a(k_y) = b + g(k_y),$$ \hfill (4.3)

where b is a constant low background transmission. $g(k_y)$ represents the pass-band of the passive system that approximates $G(k_y)$ in Eq. 4.1. Let us define

$$\mathcal{S}(k_y) = \frac{g(k_y)}{b},$$

(4.4)

to compare the "similarity" of Eq. 4.3 with Eq. 4.1. If the selectivity $\mathcal{S}(k_c)$ of the spatial filter is approximately the same as the second term in Eq. 4.3 at the center frequency, then Eq. 4.3 is said to be similar to Eq. 4.1 up to the factor b. This can be easily seen if we rewrite Eq. 4.3 as

$$a(k_y) = b[1 + \mathcal{S}(k_y)].$$

(4.5)

Once the transfer function given by Eq. 4.5 is multiplied by $A_0 = b^{-1}$, we obtain approximately the same equation as Eq. 4.1. However, this typically means amplification, since $b \ll 1$. Then, the question is, "How can we physically achieve an active transfer function from a passive spatial filter described by Eq. 4.5, especially the amplification step?" Note that this is necessary to construct Eq. 4.1, which in turn is required for the construction of the auxiliary source in the loss compensation scheme. If a band-pass spatial filter with the above mentioned properties can be designed and cascaded with the lossy metamaterial structure, then from Eqs. 4.2 and 4.5, the

transfer function of this cascaded system can be written as

$$T_A(k_y) = A_0 a(k_y) T(k_y)$$

$$= [1 + \mathcal{S}(k_y)] T(k_y). \tag{4.6}$$

Since $T_A(k_y)$ is the transfer function of the system in the presence of the auxiliary source, it is the modified or "active transfer function" of the cascaded system [26]. Hence, the theoretical framework of the active Π compensation scheme which employs an auxiliary source is physically equivalent to integrating the lossy metamaterial with a passive band-pass spatial filter of the selectivity $\mathcal{S}(k_c)$ and illuminating with a uniform plane wave of amplitude increased by a factor of $A_0 = b^{-1}$. Note that the required value of the selectivity $\mathcal{S}(k_c)$ can be obtained by optimizing the $g(k_c)$ and b. If the transmission peak is improved at the center frequency of the spatial filter, the suppression of the background transmission b can be relaxed and the process becomes more efficient due to the reduced A_0. This spatial filter should have a tunable pass-band with a high selectivity and the response must also be shift invariant along a plane perpendicular to the optical axis.

4.2.2 HMMs

Above properties in section II.A may be difficult, if not impossible, to realize with isotropic materials, but it is well known that there exists a class of metamaterials with hyperbolic dispersion which supports the propagation of evanescent modes. Spatial filtering using HMMs [27, 28, 29, 30, 31] has not been studied before directly in the context of loss compensation. Here we briefly review some of the properties of HMMs which are relevant to this work [32, 33, 34].

Without loss of generality, we assume magnetically isotropic HMMs. Then, the dispersion relation for the extraordinary waves can be easily determined from the eigenvalue equation and is

$$\frac{k_x^2}{\epsilon_y} + \frac{k_y^2}{\epsilon_x} = \frac{\omega^2}{c^2}, \tag{4.7}$$

where ω is the angular frequency and c is the speed of light in vacuum. Eq. 4.7 describes a hyperbola if the signs of the principal relative permittivity components are not the same (i.e., $\epsilon_y < 0$ and $\epsilon_x > 0$). The isofrequency contour of such a medium for transverse magnetic (TM) polarized light is shown in figure 4.2. The choice of the parameters and the operating wavelength in the figure will be detailed later on. We should also note that the contributions from the imaginary parts of the calculated relative permittivity to the isofrequency contour in figure 4.2 are negligible. From this isofrequency contour, one immediately concludes that the open form of the

102

hyperbola allows for the propagation of modes with very large transversal wavevector components, which generally leads to evanescent waves in conventional isotropic and uniaxially anisotropic media. Additionally, we make a note of the intercepts on the ordinate axis, which are crossed in figure 4.2. This shows that the medium only supports the propagation of high transversal wavevector components k_y beyond a certain cut-off. A common type of HMMs are physically constructed by alternately
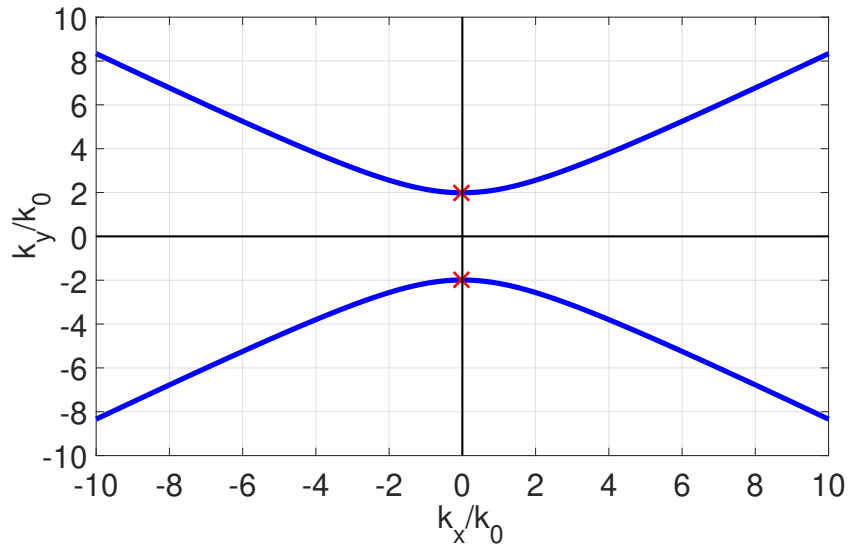
Figure 4.2: Isofrequency contour plot of a HMM with $\epsilon_y < 0$ and $\epsilon_x > 0$ at wavelength $\lambda_0 = 365\ nm$. k_0 is the free space wavenumber. The red markers indicate the cut-offs for the transversal wavevector components. The artificial material corresponding to the plot is realized by stacking 8 periods of alternating aluminium and quartz layers. The principal relative permittivity components are calculated with the effective medium approximation (see text for details).

stacking metallic and dielectric layers. Assuming that the electromagnetic parameters of individual layers are homogeneous and isotropic and the unit cell thickness is sufficiently small compared to the wavelength of the incident radiation such that the Maxwell-Garnett effective medium approximation is valid, then the system can be

described as an anisotropic medium whose principal permittivities are

$$\frac{1}{\epsilon_x} = \frac{1}{1+\eta}\left[\frac{1}{\epsilon_d} + \frac{\eta}{\epsilon_m}\right] \tag{4.8}$$

$$\epsilon_y = \epsilon_z = \frac{\epsilon_d + \eta\epsilon_m}{1+\eta}, \tag{4.9}$$

where η is the filling fraction, which is defined as the ratio of the thicknesses of the

two layers

$$\eta = \frac{T_m}{T_d}, \tag{4.10}$$

and ϵ_d and ϵ_m are the permittivities of the dielectric and metallic layers, respectively.

The cut-off transversal wavevector components marked in the isofrequency contour

in figure 4.2 can be expressed in terms of the effective parameters as

$$\frac{k_{cutoff}}{k_0} = \pm\sqrt{\frac{(1+\eta)\epsilon_m\epsilon_d}{\epsilon_m + \eta\epsilon_d}}. \tag{4.11}$$

This tells that the cut-off can be tuned by changing the material and geometric

parameters of the system. In fact, later on we will use Eq. 4.11 to select the available

materials when constructing a spatial filter with a desired cut-off frequency.
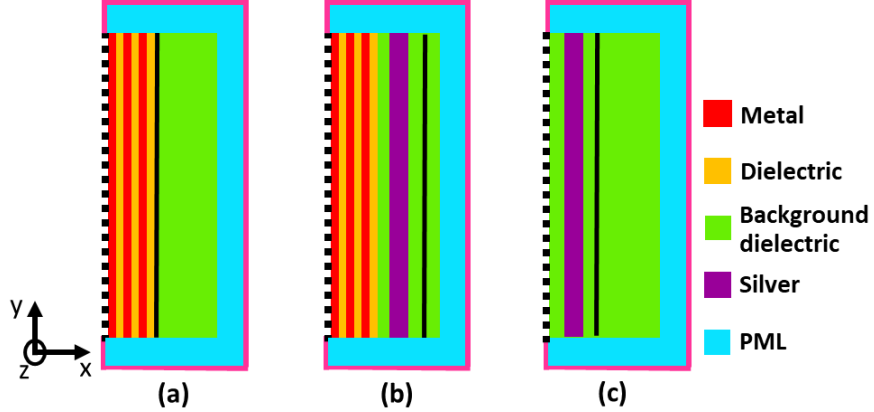
Figure 4.3: The geometries constructed in COMSOL to perform numerical simulations (not to scale) shows the (a) HMM spatial filter, and the lossy metamaterial (b) with and (c) without the HMM. Magnetic field polarized along the z-axis is incident on the input plane (dashed black lines) and the responses of the systems are extracted from the output planes (solid black lines). The red, orange, green, and blue regions are the metallic and dielectric layers of the HMM, background dielectric, and perfectly matched layers (PMLs), respectively. The purple region indicates the silver layer in the lossy metamaterial. Scattering boundary conditions are applied to the edges of the PMLs and highlighted in pink.

4.3 Results and Discussion

In section III.A, we first analyze the convolution and spatial filtering characteristics of the designed metal-dielectric multilayered structure which exhibits hyperbolic dispersion to verify if the physical system preserves all mathematical properties discussed earlier. These properties are essential to the auxiliary source which forms the backbone of the active Π loss compensation scheme. In section III.B, the HMM spatial filter is integrated with a lossy metamaterial to verify if the physically cascaded system behaves in accordance with the theoretical loss compensation framework [26] described in section II.A. This is achieved by studying the active transfer function of

the cascaded system in Eq. 4.6. Additionally, the response of the cascaded system to an arbitrary input (see Eq. 4.2) is studied to show that the HMM spatial filter can be used to physically implement the active Π loss compensation scheme. A 50 nm thick silver film coated with a 25 nm thick dielectric layer on each side is selected as the lossy metamaterial due to its simplicity and relevance to a "superlens" [19] functionality. The transmission of the structure degrades rapidly as one progresses to especially higher spatial frequencies. The transmission properties of the HMM spatial filter, the lossy metamaterial as well as the response of the integrated system to an arbitrary input are calculated with the finite element method based commercial software package COMSOL Multiphysics.

4.3.1   Convolution and spatial filtering with HMMs

The schematics of the HMM spatial filter, the lossy metamaterial with, and without the HMM are shown in figure 4.3. The same background dielectric material is used in all the structures with the relative permittivity $\epsilon_d = 2.5$ similar to the dielectric used for an experimental silver lens in [19]. Multiple HMM spatial filters, all of which use aluminium as the metallic layer are designed, each having the same overall thickness of 365 nm for consistency. The parameters used to design each spatial filter are listed in tables 4.1 and 4.2. The edges of the geometries are padded with PMLs shown in blue in figure 4.3 and backed by scattering boundary conditions indicated by the pink lines.

106

Each structure is illuminated with a TM polarized field from the input plane and the response is extracted as a complex magnetic field distribution from the output plane. For the rest of this paper we will set the operating wavelength at $\lambda_0 = 365\ nm$. This wavelength is selected because there exist near-field imaging systems and physical sources centered at 365 nm [19]. The relative permittivities of aluminum and silver at the selected wavelength are $\epsilon_{Al} = -18.179 - i3.2075$ and $\epsilon_{Ag} = -1.8752 - i0.5947$, respectively, calculated from the Drude-Lorentz model [35]. Initially, the results with the $Al - SiO_2$ HMM are presented by taking the relative permittivity of $\epsilon_d = 2.2147$ for SiO_2 at the selected wavelength [36]. Using these parameters and assuming that Eqs. 4.8 and 4.9 are valid, the relative permittivity tensor elements of the effective anisotropic material are $\epsilon_x = 3.5302 - 0.0391i$ and $\epsilon_y = -4.5832 - 1.0692i$. In figure 4.2, we used these parameters to plot the isofrequency contour for the extraordinary waves described by Eq. 4.7.

The transfer functions of the structures shown in figure 4.3 are calculated from the point spread functions (PSF) of the systems in response to a TM dipolar point source. A point source can be approximated by a Gaussian field distribution as long as the FWHM is extremely small compared with the operating wavelength. Therefore, a TM polarized Gaussian field distribution with $FWHM = 6\ nm$ is applied to the input planes of each system to determine respective transfer functions. To maintain a fairly high degree of accuracy in the calculations the spatial extent of the geometries along the y-axis is set to 80 times the wavelength. This is necessary for the shift

Table 4.1
**Geometric parameters of the HMM spatial filters and the low
cut-off wavevector components**

HMM	Unit cells	Filling fraction	Lower cut-off wavevector component (k_0)
$Al - SiO_2$	8	0.5	1.88071
$Al - Al_2O_3$	8	0.5	2.28849
$Al - Si_3N_4$	8	0.5	2.77659
$Al - ZrO_2$	8	0.5	2.96987
$Al - MoO_3$	12	0.7	3.54714
$Al - TiO_2$	12	1.1	5.11537

invariance and capturing the sufficiently large extent of the field from the output
plane. The data should not be abruptly truncated since this will introduce errors
in the Fourier transform calculations. Additionally, due to the excitation of SPPs
with large transversal wavevectors, there will be rapid field oscillations on the output
plane, as well as at each metal-dielectric interface. To capture this field accurately
we used 9500 mesh elements at each interface parallel to the y-axis with the smallest
mesh element being approximately equal to 3 nm.

Having explained the computational subtleties in the transfer function calculation,
we analyze in detail the transmission characteristics of the $Al - SiO_2$ HMM. The
amplitude and phase of the complex magnetic magnetic field in response to a point
source excitation are plotted in figures 4.5(a) and 4.5(b), respectively. If the system
is shift invariant, this field distribution becomes the PSF of the system and the
response to any arbitrary field distribution can be calculated from the PSF by using
convolution. In order to verify that the system is effectively shift invariant under the

Table 4.2
Relative permittivities of dielectrics and plasmonic metals at
$\lambda_0 = 365 \; nm.$

Materials	Relative permittivity
Ag	$-1.8752 - 0.59470i$
Al	$-18.179 - 3.2075i$
Pt	$-4.2933 - 8.5848i$
Ta	$-8.8170 - 9.0576i$
SiO_2	2.2147
Al_2O_3	3.18587
Si_3N_4	4.05373
ZrO_2	5.06205
MoO_3	$6.031 - 1.1908i$
TiO_2	$8.2886 - 0.10186i$

finite transversal extent of the HMM, hence the convolution property, we applied an arbitrary TM polarized magnetic field distribution on the input plane. The excitation field is chosen to be purely real and is plotted in figure 4.5(a). The corresponding response of the system is determined with COMSOL and is extracted as a complex magnetic field distribution from the output plane. The simulated amplitude and phase of the output magnetic field distribution are shown by the black lines in figures 4.5(a) and 4.5(b), respectively. If the convolution is satisfied, this simulated response should be equal to the convolution of the input field shown in figure 4.5(a) with the PSF of the system shown in figure 4.4. The expected response of the system from the numerical convolution is also calculated and the amplitude and phase of the output magnetic field are shown by the green lines in figures 4.5(b) and 4.5(c), respectively. When we compare the simulated response with the numerical convolution result, we
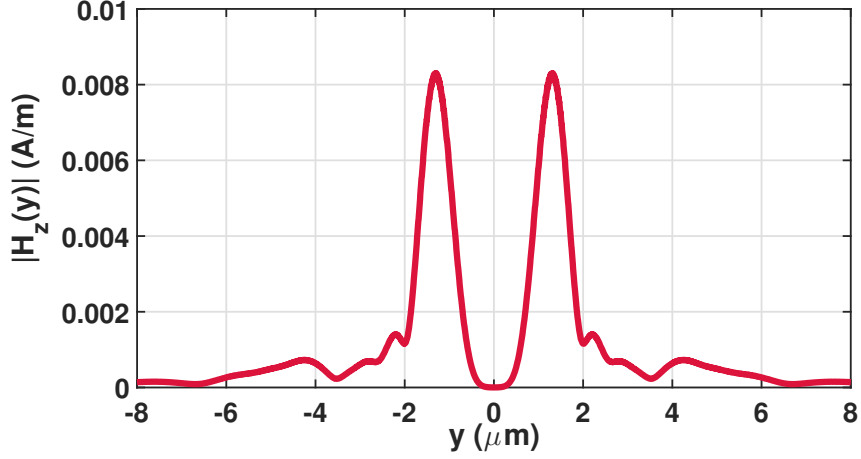
(a)
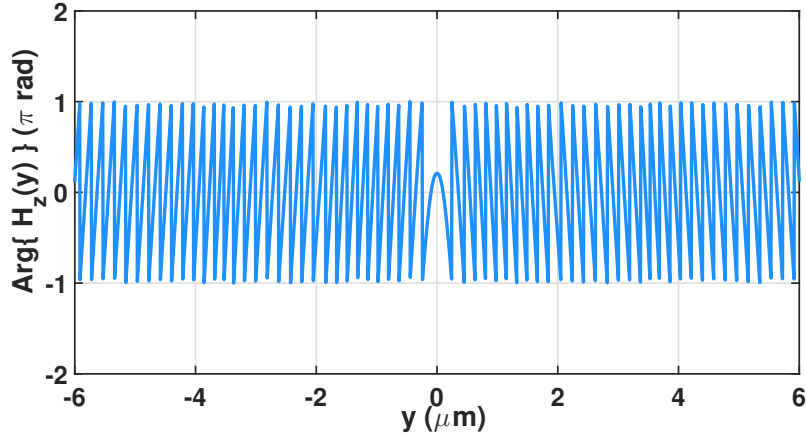
(b)

Figure 4.4: Plots of the (a) amplitude and (b) phase of the complex magnetic field distribution in response to a point source excitation. This is the PSF of the shift invariant $Al - SiO_2$ HMM and can be used to determine the response to any arbitrary incident excitation by using convolution.

can see that there is a very high degree of overlap. This indicates that the multi-layered structure is indeed effectively shift invariant under the assumed finite extents of the HMM and input field. However, the convolving feature of the HMM starts to deteriorate if the transversal extent of the HMM is decreased or that of the input field is increased.
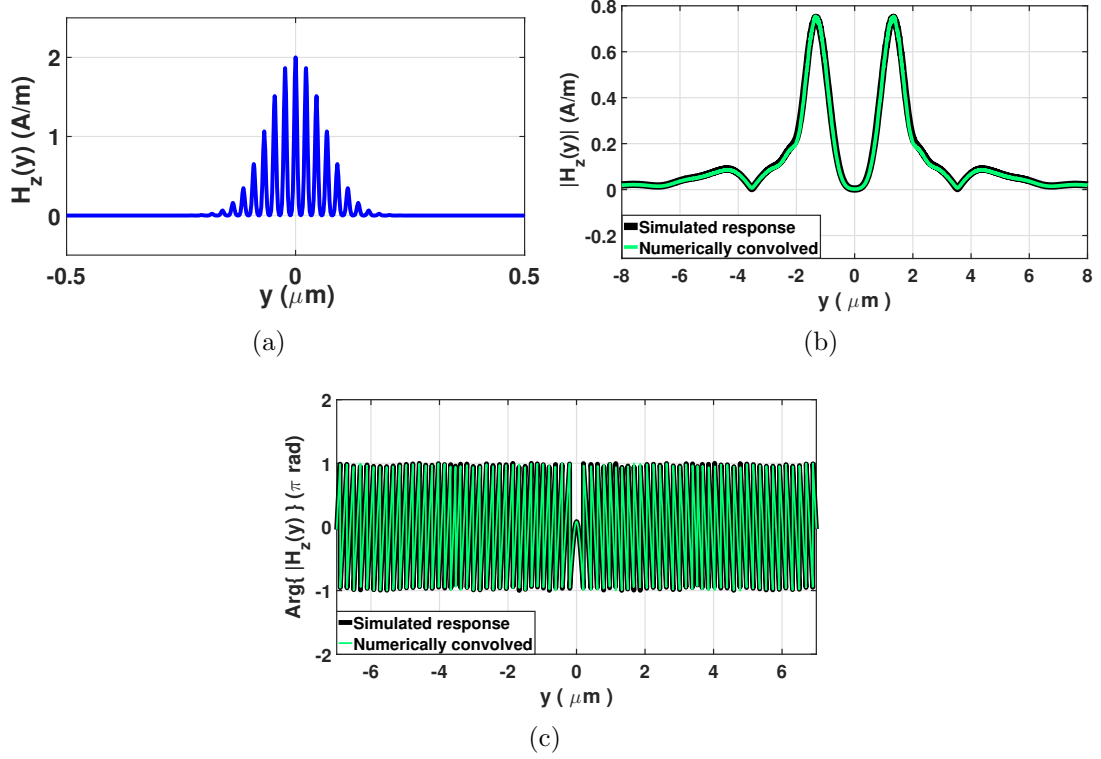
Figure 4.5: The effective shift invariance of the finite extent multi-layered $Al-SiO_2$ HMM. (a) An arbitrary TM polarized real magnetic field is applied to the geometry. (b) The amplitude and (c) the phase for the simulated response of the system, shown by the black lines are compared with those from the numerical convolution shown by the green lines.

The amplitude and phase of the complex transfer function of the $Al-SiO_2$ HMM are shown in figures 4.6(a) and 4.6(b), respectively. Four transmission peaks are clearly visible in the spectrum. Note that only the portion of the phase within the transmission band is shown. The phase varies continuously within the transmission band. The apparent discontinuities have a phase change of 2π which indicates that it is actually continuous. The cutoff wavevector component for the $Al-SiO_2$ multilayered structure can be calculated from Eq. 4.11 and is equal to $k_{cutoff} = 1.8807k_0$. The corresponding point is circled in the amplitude plot of figure 4.6(a). We see that in
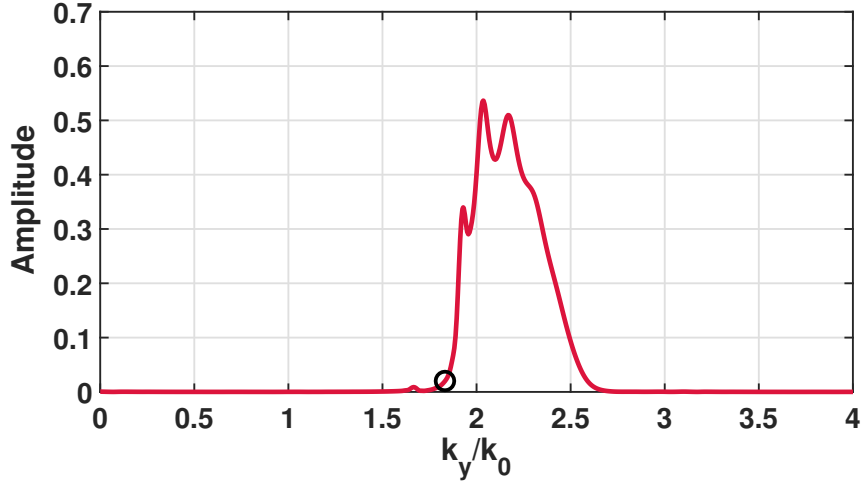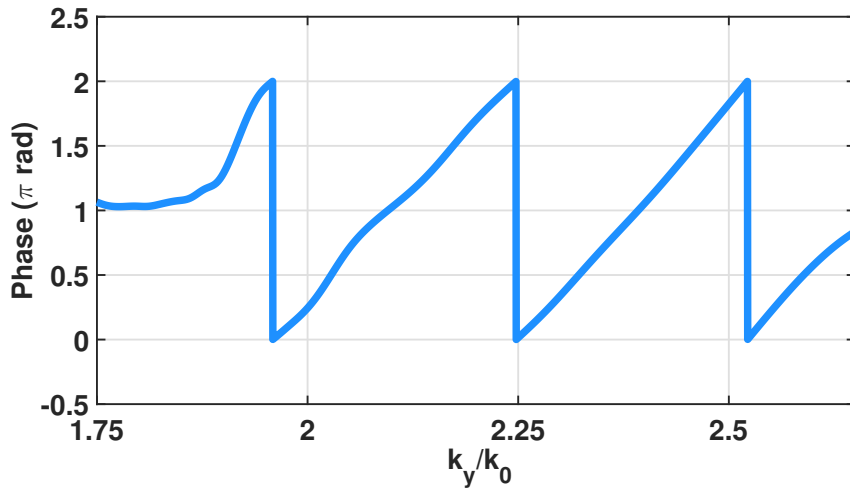
Figure 4.6: The amplitude and phase of the complex transfer function is shown in (a) and (b), respectively, for the $Al-SiO_2$ HMM. The circle in (a) corresponds to the cutoff transversal wavevector component calculated from Eq. 4.11. We see that the wave transmission sharply drops off in this region. Also, the peaks in the transmission spectrum correspond to the eigenmodes of the layered structure.

this region, the transmission drops off rapidly which is consistent with the prediction of the effective medium approximation. Figure 4.6 clearly shows the spatial filtering property of the HMM around $k_y = 2.2k_0$. In figure 4.7 we have used different dielectric
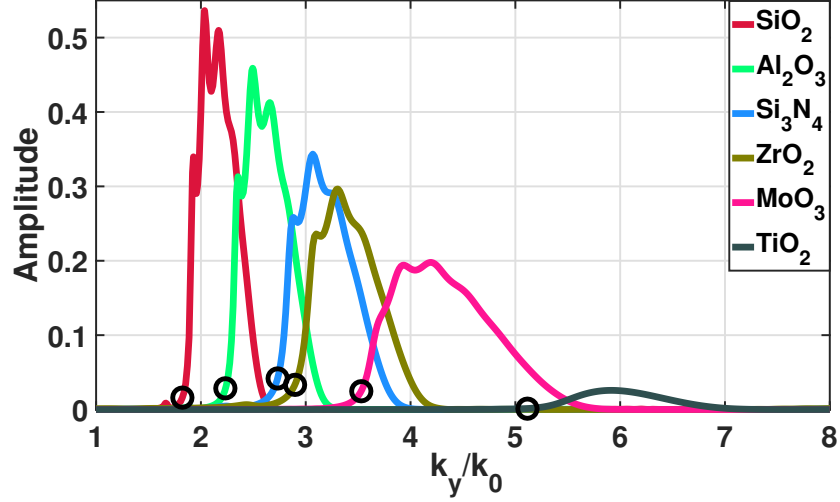
Figure 4.7: The tunable nature of the near-field spatial filter with different dielectrics. The cut-off wavevector components corresponding to each ϵ_d are calculated from Eq. 4.11 and circled in the respective transmission plots emphasizing the validity of the effective medium for the system.

materials. The material parameters for these dielectrics [36, 37, 38, 39, 40, 41] and their corresponding low cut-off wavevector components are shown in tables 4.1 and 4.2. The cut-offs are indicated by circles in the corresponding transmission plots in figure 4.7. We see that the predictions of the effective medium approximation are still valid since the amplitude transmission drops off sharply below the low cut-offs. Additionally, figure 4.7 shows the tunable nature of the designed spatial filters based on HMMs.

Note that even though Eq. 4.7 predicts an infinite number of transversal wavevector components allowed in the system, there is however an upper limit. This limit is set by the validity of the effective medium theory, which attempts to homogenize the layered system, and the rapid attenuation of high spatial frequencies [29, 42].

The approximation ceases to be valid whenever the wavelength corresponding to the longitudinal wavevector component k_x approaches the periodicity of the the layered structure which in our case is 45 nm.

The general guidelines for designing a near-field band-pass spatial filter can be determined from Eq. 4.11. Also, figure 4.8 shows the low cut-off wavevector component k_{cutoff} from Eq. 4.11 plotted as a function of the dielectric relative permittivity ϵ_d for different plasmonic metals at $\lambda_0 = 365$ nm. $\eta = 0.5$ is kept in all the plots. The permittivity of platinum is calculated from the Drude-Lorentz model with the data given in [35] whereas the relative permittivity of tantalum is taken from the reflection electron energy-loss spectroscopy data in [43]. The relative permittivity data is summarized in table 4.2. Figure 4.8 can be used to estimate the relative permittivity of the required dielectric material for different plasmonic metals. The slope of the plots is the measure of the sensitivity of the tunable nature of the spatial filter. The sensitivity depends on the selection of both plasmonic metal and the ratio η. Note that although silver has the highest sensitivity in figure 4.8, it has a limit beyond which the filter cannot be tuned with dielectrics. This is due to the loss of the hyperbolic nature of the layered structure above a certain value of the relative permittivity ϵ_d. In contrast, other metals allow tunability for a broader range of transversal wavevector components at the expense of higher loss and stringent dielectric permittivity requirements. While loss can be mitigated by controlling the filling fraction or the number of unit cells to some extent, the requirement of large permittivity imposes a
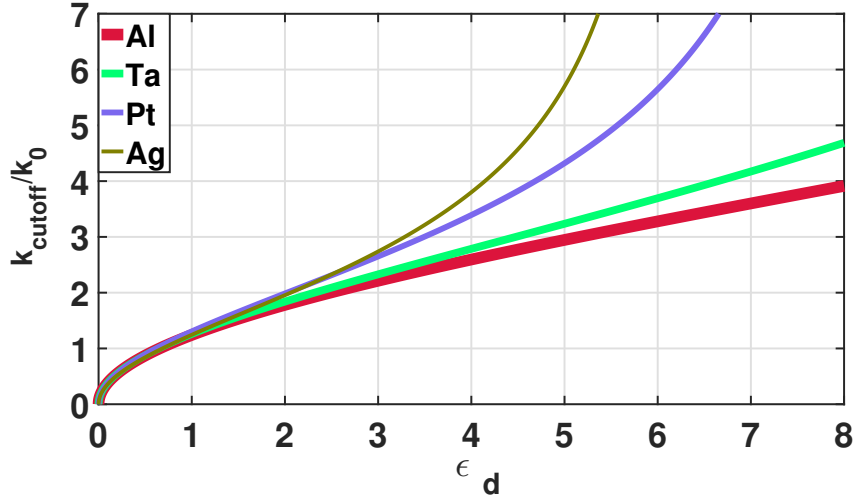
Figure 4.8: Plots of the low cut-off transversal wavevector components versus the dielectric relative permittivity ϵ_d for different plasmonic metals which give hyperbolic dispersion at $\lambda_0 = 365\ nm$ taking the filling fraction $\eta = 0.5$.

limitation on the tunability especially at small optical wavelengths. Note, however, that the spatial filters can be scaled to different wavelengths as long as the layered system exhibits hyperbolic dispersion. This is because the normalized cutoff wavevector component in Eq. 4.11 is not explicitly dependent on the wavelength and varies according to the material parameters and filling fraction.
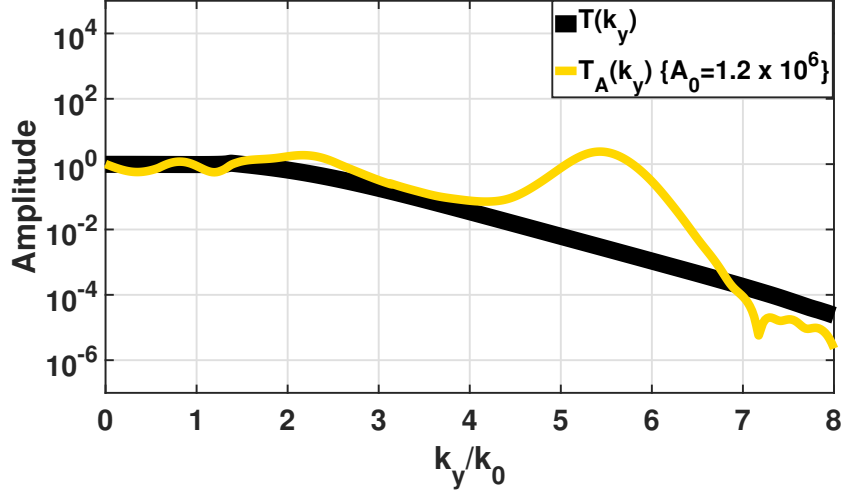
Figure 4.9: Plot of the passive transfer function of the lossy metamaterial $T(k_y)$ and the active transfer function $T_A(k_y)$ of the $Al - TiO_2$ HMM integrated with the lossy metamaterial. Losses progressively degrade the transmission of transversal wavevector components greater than k_0. However, the transmission spectrum of the active transfer function of the integrated system shows an improvement within the pass-band of the filter. The enhancement is on the order of $\mathcal{S}(k_y)$ and $A_0 = 1.2 \times 10^6$.

4.3.2 Implementation of the active Π loss compensation scheme with the HMM

The HMM spatial filters can physically emulate all the mathematical properties to generate the auxiliary source in the Π scheme. When an arbitrary input field with increased amplitude (i.e., by a factor of A_0) is incident on an HMM, the auxiliary source will be produced on the output plane of the HMM (see figure 4.3a) superimposed with the original arbitrary input field (see Eq. 4.2). The next step involves implementing the Π scheme by integrating the $Al - TiO_2$ filter with the lossy metamaterial (see figure 4.3b). This is verified by analyzing the active transfer function description of the

integrated system (see Eq. 4.6) and comparing with the passive transfer function of the lossy metamaterial structure (see figure 4.3c). The transfer function of the lossy metamaterial $T(k_y)$, is shown by the black line in figure 4.9. We observe how the losses progressively degrade transmission through the metamaterial with increasing k_y. The performance of the physical system will be further impacted by noise from multiple sources which tends to distort the field at the output plane. Such sources of noise can be related to, for example, the roughness in the nanostructures of the metamaterial or the detector which samples the intensity distribution from the output plane. This makes it challenging to overcome losses in a metamaterial without amplifying noise. However, if the transfer function of the lossy system $T(k_y)$ can be determined to a sufficient degree of accuracy, then the amount of compensation necessary for each attenuated transversal wavevector component can be estimated and provided by the active transfer function $T_A(k_y)$ of the integrated system as shown in figure 4.9. The peak in the active transfer function corresponds to the pass-band of the $Al - TiO_2$ filter which is shown in figure 4.7. As described by Eq. 4.6, the transmission within this pass-band is increased on the order of $\mathcal{S}(k_y)$. For example, figure 4.9 is obtained by the filter with the selectivity of $\mathcal{S}(k_c = 5.8k_0) \sim 10^3$ and $b \sim 10^{-6}$. Such improving of the transfer function using the integrated system is important for two reasons. First, the plot of the active transfer function provides evidence that integrating the $Al - TiO_2$ filter with the lossy metamaterial cascades the two systems such that the overall behavior can be described by Eq. 4.6 (i.e., convolution dictated by Eq. 6 is

maintained between the output of the HMM filter and the point spread function of the lossy metamaterial). Second, recall that the factor A_0 (see Eq. 4.1) scales the amount of selective amplification provided by the auxiliary source. Figure 4.9 shows that this is physically equivalent to integrating the lossy metamaterial with a high selectivity spatial filter and increasing the amplitude of illumination by a factor of A_0.

In order to confirm the viability of the HMM spatial filter in a loss compensation scenario, we compare the response of the lossy metamaterial to an arbitrary input field, with (see figure 4.3b) and without (see figure 4.3c) the integrated HMM spatial filter. The output is distorted by noise from a combination of signal dependent (SD) and signal independent (SI) sources using the "signal-modulated noise" model in [44, 45, 46]. This study uses $0.0045H_o(y)$ and $0.005\ A/m$ for the standard deviations of SD and SI noise, respectively, where $H_o(y)$ is the noise-free spatial field distribution on the output plane. These standard deviations are larger than the ones used in [26, 47], and in an experimental optical detector [48], and are selected, because they illustrate the deleterious effect of noise in a lossy metamaterial system and further stress the improvement achieved by integrating the spatial filter into the lossy system. In the subsequent discussion, the lossy metamaterial is first illuminated with a weak input field and the noisy response is analyzed in the Fourier domain. Then, the intensity of illumination is increased to see any improvements in the output spectrum. Finally, the integrated system is illuminated with the same increased input field and the three

(a)

(b)

(c)
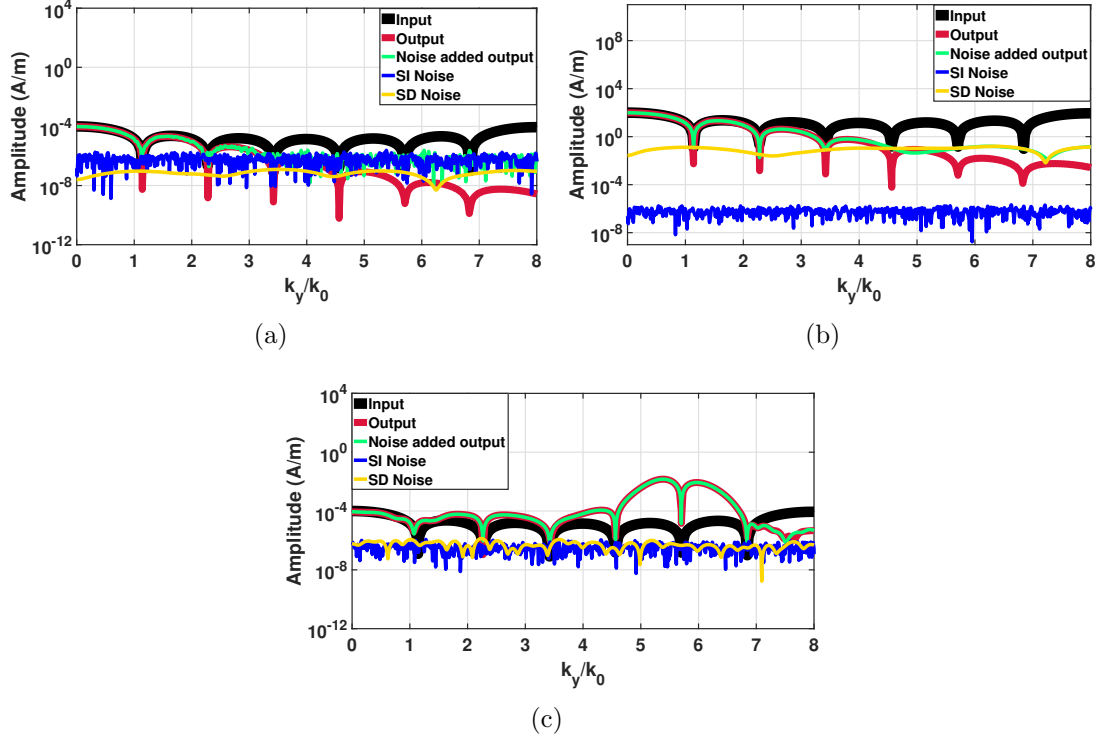
Figure 4.10: Fourier spectrum amplitudes of the input and output fields with and without added noise under the configurations, (a) weak illumination, (b) strong illumination, and (c) structured illumination. The SD and SI noise spectra show their relative contributions in the noise added output fields. Note that the most of the nodes in the input spectrum are completely obscured by noise at the output plane as shown by the green line in (a). Increasing the amplitude of illumination by a factor of 1.2×10^6 only slightly improves the noisy output spectrum in (b), because the SD noise is proportionally amplified and is the dominant source of distortion. However, with the HMM spatial filter integrated into the system in (c), the improvement in the noisy output spectrum is significant even under the same high intensity illumination as in (b). Nodes belonging to the input field spectrum within $4k_0 < k_y < 7k_0$ which were previously obscured by noise in both (a) and (b) are now visible in the noise added output spectrum in (c). Additionally, the SD noise amplification in (c) is much smaller when compared with (b). The level of SD noise is close to the SI noise similar to (a) indicating little noise amplification.

results are compared. We refer to these three cases as *"weak illumination," "strong illumination,"* and *"structured illumination,"* respectively. Figure 4.10 compares the results for the three cases. The black line shows the spectrum of the input field

119

desired to be transmitted faithfully (see figure 4.1) and the corresponding noise-free output is shown by the red line. The noise added output is shown by the green line and it contains random distortions from SD and SI sources of noise. Additionally, the Fourier spectra of the SD and SI noise which contribute to this distortion are also shown in the figure by yellow and blue lines, respectively. Note that the choice of the input field is purely arbitrary and is selected to complement the discussion to follow.

Let us first consider the weak illumination case (see the upper section in figure 4.1a); that is the response of the lossy metamaterial system to an input field when the amplitude of illumination is $1A/m$. The noise-free output spectrum shown by the red line in figure 4.10(a) shows deteriorating transmission with increasing k_y. Nevertheless, the nodes of the input spectrum are still visible. However, the most of the nodes are completely obscured in the noise added output spectrum especially for $k_y > 3k_0$ as shown by the green line in figure 4.10(a), because with increasing k_y the amplitude of distortion introduced by the combination of SI and SD noise becomes comparable to and eventually dominates the output spectrum. In the strong illumination regime shown in figure 4.10(b), the field amplitude is strengthened by a factor of 1.2×10^6. The Fourier spectrum of the noise added output shows a slight improvement compared to the weak illumination case in figure 4.10(a). This can be understood if we compare the intersection point of the output spectrum with the SD noise spectrum in figures 4.10(a) and 4.10(b). When the intensity of illumination is increased, only the Fourier components until this intersection point are simply raised above the SI noise.

This intersection marks the point in the Fourier domain where the amplitude of transmission in the output spectrum becomes equal to the distortion introduced by the SD noise. As the intensity of the illumination is increased, the output spectrum and the SD noise increase with the same proportion. Therefore, the Fourier component where the two intersect does not change and the Fourier components of the output spectrum beyond this point are always buried under the SD noise. Additional increments to illumination intensity will have no effect on the noise added output spectrum. Consider the structured illumination case in figure 4.10(c). The lossy metamaterial is integrated with the $Al - TiO_2$ HMM spatial filter and illuminated by the same high field amplitude of $1.2 \times 10^6 A/m$ (see figure 4.1b). The pass-band of the $Al - TiO_2$ HMM filter is shown in figure 4.7 and the active transfer function of the integrated system is shown in figure 4.9. We can immediately see that under the structured illumination, the level of SD noise in the Fourier spectrum is comparable with the SI noise similar to the low intensity case shown in figure 4.10(a). Importantly, the noise added output spectrum in figure 4.10(c) closely follows the noise-free output spectrum until about $7k_0$. In accordance with Eq. 4.6 and figure 4.9, below $4k_0$ the field spectrum remains intact as can be seen by the overlapping output (see green solid line in figure 4.10(c)) and input (see black solid line in figure 4.10(c)) spectra. Also, the three nodes within $4k_0 < k_y < 7k_0$, which were previously buried under the noise in figures 4.10(a) and 4.10(b), are now visible in figure 4.10(c), consistent with the active transfer function of the integrated system plotted in figure 4.9.

121

The above discussion clearly shows that a high selectivity HMM spatial filter can be used to physically implement the active Π loss compensation scheme by constructing the required auxiliary source that selectively amplifies a narrow band of high spatial frequencies (see Eq. 4.1). It is important to note that the concept shown in the above discussion is a physical implementation of the theory presented in [26] where the merits of selective amplification with auxiliary source were presented. Figure 4.10(c) and the accompanying discussion verify the concept with a physically designed auxiliary source and extend the idea of selective amplification to cascaded systems with controlled amplitude of illumination for amplification as described by Eq. 4.6.

In [49] the proposed implementation of the Π scheme with high selectivity integrated spatial filters under high intensity illumination, as described here, has been shown to enhance the resolution of a silver superlens imaging system, where the loss compensated output field is deconvolved with the active point spread function to improve the resolution. In Fourier domain, this is simply the inverse filtering of the output spectrum (see green solid line in figure 4.10(c)) with the active transfer function expressed by Eq. 4.6 (see also yellow solid line in figure 4.9).

4.4 Conclusion

In conclusion, we have proposed the use of a near-field spatial filter for the active implementation [26] of the recently introduced Π loss compensation scheme [18]. This presents in detail the first possible physical implementation of the scheme with arbitrary optical fields which has been only a mathematical abstraction before [18, 26]. The "tunability", "selective amplification" characteristics of the auxiliary source in the Π scheme can be realized with the layered metal-dielectric systems with hyperbolic dispersion that act as near-field spatial filters. We have verified that the convolution, which is vital for the construction of the auxiliary source, can be achieved in the layered system. This allows such layered systems to be integrated with the near-field superlenses (e.g., silver [19] and SiC [20] lenses), so that the complete imaging system can be described with a modified transfer function. The work here paves the way to a robust loss compensation scheme for enhanced near-field superlensing with ultra-high resolution [29, 30, 42, 49, 50]. A spatial filter of this form may also have potential applications in "edge-detection" as proposed for acoustics in a recent work [51], where an acoustic metamaterial is used to transmit the high-spatial evanescent modes while suppressing the propagating modes.

References

[1] Wyatt Adams, Mehdi Sadatgol, and Durdu Ö . Güney. Review of near-field optics and superlenses for sub-diffraction-limited nano-imaging. *AIP Advances*, 6(10):100701, 2016.

[2] Carsten Rockstuhl, Stephan Fahr, and Falk Lederer. Absorption enhancement in solar cells by localized plasmon polaritons. *Journal ofApplied Physics*, 104(12):123102, 2008.

[3] Jephias Gwamuri, Ankit Vora, Jeyanthinath Mayandi, Durdu Ö Güney, Paul L Bergstrom, and Joshua M Pearce. A new method of preparing highly conductive ultra-thin indium tin oxide for plasmonic-enhanced thin film solar photovoltaic devices. *Solar Energy Materials and Solar Cells*, 149:250–257, 2016.

[4] Arash Ahmadivand, Nezih Pala, and Durdu Ö Güney. Enhancement of photothermal heat generation by metallodielectric nanoplasmonic clusters. *Optics Express*, 23(11):A682–A691, 2015.

[5] John Brian Pendry. Negative refraction makes a perfect lens. *Physical Review Letters*, 85(18):3966, 2000.

[6] VG Veselago. The electrodynamics of substances with simultaneously negative values of ϵ and μ. *Usp. Fiz. Nauk*, 92:517, 1967.

[7] Richard A Shelby, David R Smith, and Seldon Schultz. Experimental verification of a negative index of refraction. *science*, 292(5514):77–79, 2001.

[8] Nicholas Fang and Xiang Zhang. Imaging properties of a metamaterial superlens. In *Proceedings of the 2nd IEEE Conference on Nanotechnology*, pages 225–228. IEEE, 2002.

[9] David OS Melville and Richard J Blaikie. Super-resolution imaging through a planar silver layer. *Optics Express*, 13(6):2127–2134, 2005.

[10] Viktor A Podolskiy and Evgenii E Narimanov. Near-sighted superlens. *Optics Letters*, 30(1):75–77, 2005.

[11] David R Smith, David Schurig, Marshall Rosenbluth, Sheldon Schultz, S Anantha Ramakrishna, and John B Pendry. Limitations on subdiffraction imaging with a negative refractive index slab. *Applied Physics Letters*, 82(10):1506–1508, 2003.

[12] Shuang Zhang, Wenjun Fan, NC Panoiu, KJ Malloy, RM Osgood, and SRJ

Brueck. Experimental demonstration of near-infrared negative-index metamaterials. *Physical Review Letters*, 95(13):137404, 2005.

[13] Sebastian Wuestner, Andreas Pusch, Kosmas L Tsakmakidis, Joachim M Hamm, and Ortwin Hess. Overcoming losses with gain in a negative refractive index metamaterial. *Physical Review Letters*, 105(12):127401, 2010.

[14] Shumin Xiao, Vladimir P Drachev, Alexander V Kildishev, Xingjie Ni, Uday K Chettiar, Hsiao-Kuan Yuan, and Vladimir M Shalaev. Loss-free and active optical negative-index metamaterials. *Nature*, 466(7307):735–738, 2010.

[15] Maziar P Nezhad, Kevin Tetz, and Yeshaiahu Fainman. Gain assisted propagation of surface plasmon polaritons on planar metallic waveguides. *Optics Express*, 12(17):4072–4079, 2004.

[16] Alexander K Popov and Vladimir M Shalaev. Compensating losses in negative-index metamaterials by optical parametric amplification. *Opt. Lett.*, 31(14):2169–2171, 2006.

[17] Durdu Ö Güney, Thomas Koschny, and Costas M Soukoulis. Reducing ohmic losses in metamaterials by geometric tailoring. *Physical Review B*, 80(12):125129, 2009.

[18] Mehdi Sadatgol, Sahin K Ozdemir, Lan Yang, and Durdu Ö Güney. Plasmon injection to compensate and control losses in negative index metamaterials. *Physical Review Letters*, 115(3):035502, 2015.

[19] Nicholas Fang, Hyesog Lee, Cheng Sun, and Xiang Zhang. Sub–diffraction-limited optical imaging with a silver superlens. *Science*, 308(5721):534–537, 2005.

[20] Thomas Taubner, Dmitriy Korobkin, Yaroslav Urzhumov, Gennady Shvets, and Rainer Hillenbrand. Near-field microscopy through a sic superlens. *Science*, 313(5793):1595–1595, 2006.

[21] Zubin Jacob, Leonid V Alekseyev, and Evgenii Narimanov. Optical hyperlens: far-field imaging beyond the diffraction limit. *Optics Express*, 14(18):8247–8256, 2006.

[22] Wyatt Adams, Mehdi Sadatgol, Xu Zhang, and Durdu Ö Güney. Bringing the 'perfect lens' into focus by near-perfect compensation of losses without gain media. *New Journal of Physics*, 18(12):125004, dec 2016.

[23] Wyatt Adams, Mehdi Sadatgol, and Durdu Ö Xu Zhang andGüney. Enhancing the resolution of hyperlens by the compensation of losses without gain media. *Progress In Electromagnetics Research C*, 70:1–7,, 2016.

[24] Xu Zhang, Wyatt Adams, and Durdu Ö Güney. Analytical description of inverse filter emulating the plasmon injection loss compensation scheme and implementation for ultrahigh-resolution hyperlens. *Journal of Optical Society of America B*, 34(6):1310–1318, 2017.

[25] Wyatt Adams, Anindya Ghoshroy, and Durdu Ö Güney. Plasmonic superlens image reconstruction using intensity data and equivalence to structured light

illumination for compensation of losses. *Journal of Optical Society of America B*, 34(10):2161–2168, 2017.

[26] Anindya Ghoshroy, Wyatt Adams, Xu Zhang, and Durdu Ö Güney. Active plasmon injection scheme for subdiffraction imaging with imperfect negative index flat lens. *Journal of Optical Society of America B*, 34(7):1478–1488, 2017.

[27] David Schurig and David R Smith. Spatial filtering using media with indefinite permittivity and permeability tensors. *Applied Physics Letters*, 82(14):2215–2217, 2003.

[28] Carlo Rizza, Alessandro Ciattoni, Elisa Spinozzi, and Lorenzo Columbo. Terahertz active spatial filtering through optically tunable hyperbolic metamaterials. *Optics Letters*, 37(16):3345–3347, 2012.

[29] Ling Liu, Ping Gao, Kaipeng Liu, Weijie Kong, Zeyu Zhao, Mingbo Pu, Changtao Wang, and Xiangang Luo. Nanofocusing of circularly polarized bessel-type plasmon polaritons with hyperbolic metamaterials. *Materials Horizons*, 4(2):290–296, 2017.

[30] Gaofeng Liang, Xi Chen, Qing Zhao, and L Jay Guo. Achieving pattern uniformity in plasmonic lithography by spatial frequency selection. *Nanophotonics*, 7(1):277–286, 2018.

[31] Marcin Kieliszczyk, Bartosz Janaszek, Anna Tyszka-Zawadzka, and Paweł

Szczepański. Tunable spectral and spatial filters for the mid-infrared based on hyperbolic metamaterials. *Applied Optics*, 57(5):1182–1187, 2018.

[32] Alexander Poddubny, Ivan Iorsh, Pavel Belov, and Yuri Kivshar. Hyperbolic metamaterials. *Nature Photonics*, 7(12):948, 2013.

[33] Prashant Shekhar, Jonathan Atkinson, and Zubin Jacob. Hyperbolic metamaterials: fundamentals and applications. *Nano Convergence*, 1(1):14, 2014.

[34] Vladimir P Drachev, Viktor A Podolskiy, and Alexander V Kildishev. Hyperbolic metamaterials: new physics behind a classical problem. *Optics Express*, 21(12):15048–15064, 2013.

[35] Aleksandar D Rakić, Aleksandra B Djurišić, Jovan M Elazar, and Marian L Majewski. Optical properties of metallic films for vertical-cavity optoelectronic devices. *Applied Optics*, 37(22):5271–5283, 1998.

[36] Lihong Gao, Fabien Lemarchand, and Michel Lequime. Exploitation of multiple incidences spectrometric measurements for thin film reverse engineering. *Optics Express*, 20(14):15734–15751, 2012.

[37] Raymond L Kelly. Program of the 1972 annual meeting of the optical society of america. *Journal of Optical Society of America B*, 62(11):1336–1336, 1972.

[38] Kevin Luke, Yoshitomo Okawachi, Michael RE Lamont, Alexander L Gaeta, and

Michal Lipson. Broadband mid-infrared frequency comb generation in a si_3n4 microresonator. *Optics Letters*, 40(21):4823–4826, 2015.

[39] Darwin L Wood and K Nassau. Refractive index of cubic zirconia stabilized with yttria. *Applied Optics*, 21(16):2978–2981, 1982.

[40] Luc Lajaunie, Florent Boucher, Remi Dessapt, and Philippe Moreau. Strong anisotropic influence of local-field effects on the dielectric response of α-moo_3. *Physical Review B*, 88(11):115141, 2013.

[41] Thomas Siefke, Stefanie Kroker, Kristin Pfeiffer, Oliver Puffky, Kay Dietrich, Daniel Franta, Ivan Ohlídal, Adriana Szeghalmi, Ernst-Bernhard Kley, and Andreas Tünnermann. Materials pushing the application limits of wire grid polarizers further into the deep ultraviolet spectral range. *Advanced Optical Materials*, 4(11):1780–1786, 2016.

[42] Lian Shen, Huaping Wang, Rujiang Li, Zhiwei Xu, and Hongsheng Chen. Hyperbolic-polaritons-enabled dark-field lens for sensitive detection. *Scientific Reports*, 7(1):1–8, 2017.

[43] Wolfgang SM Werner, Kathrin Glantschnig, and Claudia Ambrosch-Draxl. Optical constants and inelastic electron-scattering data for 17 elemental metals. *Journal of Physical and Chemical Reference Data*, 38(4):1013–1092, 2009.

[44] John F Walkup and Robert C Choens. Image processing in signal-dependent noise. *Optical Engineering*, 13(3):133258, 1974.

[45] John J Heine and Madhusmita Behera. Aspects of signal-dependent noise characterization. *Journal of Optical Society of America A*, 23(4):806–815, 2006.

[46] Gary K Froehlich, John F Walkup, and Thomas F Krile. Estimation in signal-dependent film-grain noise. *Applied Optics*, 20(20):3619–3626, 1981.

[47] Yulu Chen, Yu-Chun Hsueh, Mengren Man, and Kevin J Webb. Enhanced and tunable resolution from an imperfect negative refractive index lens. *Journal of Optical Society of America B*, 33(3):445–451, 2016.

[48] Makoto Akiba, Kenji Tsujino, and Masahide Sasaki. Ultrahigh-sensitivity single-photon detection with linear-mode silicon avalanche photodiode. *Optics Letters*, 35(15):2621–2623, 2010.

[49] Anindya Ghoshroy, Wyatt Adams, Xu Zhang, and Durdu Ö Güney. Enhanced superlens imaging with loss-compensating hyperbolic near-field spatial filter. *Optics Letters*, 43(8):1810–1813, 2018.

[50] Wyatt Adams, Anindya Ghoshroy, and Durdu O Guney. Plasmonic superlens imaging enhanced by incoherent active convolved illumination. *ACS Photonics*, 5(4):1294–1302, 2018.

[51] Miguel Molerón and Chiara Daraio. Acoustic metamaterial for subwavelength edge detection. *Nature communications*, 6(1):1–6, 2015.

Chapter 5

Theory of coherent active convolved illumination for superresolution enhancement[1]

---

[1]Reprinted from A. Ghoshroy, W. Adams, and D. O. Guney, "Theory of coherent active convolved illumination for superresolution enhancement," *J. Opt. Soc. Am. B* 37, 2452 (2020); with permission from ©The Optical Society.

5.1 Introduction

Metamaterials (MMs), which are artificial inhomogeneous structures usually designed with subwavelength metal/dielectric or all-dielectric building blocks, rose to prominence nearly two decades ago as an appealing direction for designing materials with unprecedented electromagnetic properties previously considered difficult, if not impossible, to realize. Invisibility cloaks [1], ultra-high-resolution imaging [2, 3, 4] and photolithography [5], enhanced photovoltaics [6, 7], miniaturized antennas [8], ultra-fast optical modulation [9], and metasurfaces [10, 11] are few of the multitude of applications which have been envisioned. Supported by parallel efforts in micro and nanofabrication, MMs are anticipated to have broad impact on many technologies employing electromagnetic radiation. However, despite enormous theoretical and experimental progress, numerous lingering problems [12] require diligent consideration. Optical losses continue to be one of the greatest threats to the viability of many of the MM-based devices proposed to date. Mitigation of losses remains a challenging problem for the MM community. Gain medium was initially proposed [13, 14, 15, 16] as a potential solution. However, later studies showed that stability and gain saturation issues as a result of stimulated emission near the field enhancement regions leads to intense noise generation [17, 18, 19]. Due to these concerns and other associated complexities such as pump requirement, progress towards the development of a robust loss compensation scheme has been somewhat sluggish even after nearly two decades

of efforts. Dielectric metasurfaces have also been proposed to alleviate some of these concerns [10, 11].

A recent theoretical study [20] investigated an unconventional approach in the form of an alternative exploration of "virtual gain" [21, 22] to manage the losses in MMs. This compensation process, designated "plasmon injection (PI or Π) scheme," employs an additional source to modify the field incident on a lossy MM. This auxiliary source is designed to adequately amplify an arbitrary field thereby enhancing its transmission through the MM. A multiport MM structure was used in [20] to illustrate the conceptual operating principle for the amplification of normally incident waves. Auxiliary fields are used to coherently add energy to the lossy system to compensate the losses of different natures. This amplification mechanism was related in [22, 23] to coherent amplification of pulses using a passive cavity described in [24, 25]. The main difference in [20] is continuous wave operation at the nanoscale plasmonic MM structure. In [26, 27, 28], we discussed in detail the generalization of the Π scheme to imaging, which involves a spectrum of spatial frequencies. A systematic amplification in the Fourier spectrum plays a key role in extending the resolution limit of the imaging system. This is akin to the Wiener optimal filtering principle that also attempts to cleverly privilege spatial frequencies with respect to their noises [29, 30, 31]. The earlier theoretical studies with MM or near-field imaging systems employing negative index materials (NIMs) [32], superlenses [33], and hyperlenses [34, 35] produced promising results. Implementing the Π scheme with the above systems resulted in

performance improvements. The distinguishing feature of the Π scheme is the auxiliary source. The earlier variants of the Π scheme were shown to emulate linear deconvolution [32].

The physical generation of the auxiliary source requires some considerations. It was shown [26] that the auxiliary source can be generated through a convolution process with the original object field incident at the detector while selectively providing amplification to a controllable band of spatial frequencies. As a result of this process, the auxiliary source becomes correlated with the original object field [26, 36]. A near-field spatial filter designed with hyperbolic metamaterials (HMMs) was proposed to physically generate the auxiliary source [27] with the above properties. The filter was integrated with a 50 nm silver film to illustrate the overall loss compensation process. This was the first potential application of the spatial filtering properties [37, 38, 39, 40, 41] of HMMs in the context of loss compensation. Later studies with coherent [28] and incoherent [42] illumination produced favourable results. An improvement in the resolution limit of a near-field silver superlens elevated the viability of the Π scheme as an effective alternative to previously conceived loss mitigation approaches [7, 13, 14, 15, 16, 43, 44] including dielectric metasurfaces [10, 11]. Even though the techniques presented in [28, 42] possess similar properties to the original concept of the Π scheme in [20], the scheme was generalized to a more encompassing term active convolved illumination (ACI) in [42], since it is essentially the physical convolution operation which is key to the process. Also, the Π scheme narrows down

the process to only plasmons. More recently, the ACI technique has been applied to an experimental system, where the signal-to-noise ratio (SNR) and resolution limit of a reference far-field imaging system have been significantly improved with a modest amount of amplification [45]. It has also been shown that the ACI offers more tolerance to pixel saturation compared to the reference system.

In this paper, we construct a theoretical framework to provide the first comprehensive mathematical exposition of the fundamental concept of ACI for coherent illumination. Pendry's classic setup [2] of a silver superlens operating at a wavelength of $365\,\mathrm{nm}$ is adopted since it is the simplest configuration which broadly exemplifies the rudimentary impact of optical losses such as in not only MM systems, but also different conventional and advanced linear systems. We consider the silver superlens only as a canonical example to accentuate how the ACI permits recovery of information carried by attenuated signal with minimal noise amplification. The greater scope of this paper is to develop a noise-resistant imaging theory that can be potentially generalized to a wide range of problems in various contexts related to noisy linear systems. Specific attention is drawn towards the required mechanisms, such as selective spectral amplification, physical convolution, and correlations. This study strengthens analytically, the previous results and associated assertions [28, 42] made with numerical simulations to gain physical insight into the ACI's working principles in imaging. We conjecture that the theory of ACI can be potentially generalized to a wide variety of noisy and lossy linear systems including, for example, those in

atmospheric imaging [46, 47, 48, 49], time-domain spectroscopy [50, 51], optical communications [52, 53, 54, 55], $\mathcal{PT}$ symmetric non-Hermitian photonics [21, 56, 57], and even quantum computing [49, 58, 59]. Some discussions of how the ACI can be applied to atmospheric imaging, time-domain spectroscopy, and quantum computing can be found in [49].

5.2 Near-Field Imaging System with ACI

As Pendry pointed out [2], the properties of a NIM necessary for superresolution imaging far beyond the diffraction limit, can be attained for transverse magnetic (TM) polarized light at a wavelength $\lambda = 365\,\mathrm{nm}$ by a thin silver film embedded inside a dielectric. Under such conditions, resonant excitation of surface plasmons at the silver interface provides satisfactory amplification to high spatial frequencies which can then be focused assuming that the thickness of the silver film, object and image plane distances are much smaller than the incident wavelength. The configuration of such an imaging system is shown in Fig. 5.1(a), where the silver film with thickness d is embedded inside a dielectric and positioned symmetrically between the object and image planes indicated by solid and dashed black lines, respectively. A TM field distribution on the object plane is detected from the image plane after propagating though the silver film. During this propagation process, material

losses progressively degrade the transmission of high spatial frequencies with increasing transversal wavenumber k_y. Therefore, the ultimate performance of the system is limited to the highest spatial frequency whose attenuated amplitude is strong enough to be accurately detected from the image plane amid noise. An ideal loss compensation scheme should extend this limit by intelligently providing adequate amounts of power to these previously undetectable spatial frequencies to allow them to survive the lossy transmission process by ensuring minimal noise amplification.
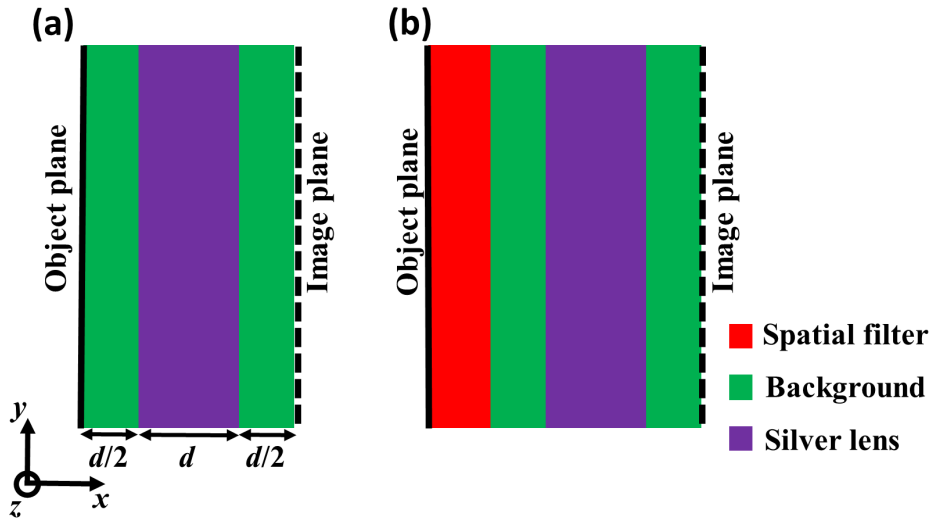
Figure 5.1: Schematic of a typical silver lens imaging system (a) without ACI and (b) the modified form with the integrated spatial filter for an implementation of ACI. The TM-polarized field distribution on the object plane propagates through each system and is recorded from the image plane. The purple, green, and red regions are the silver lens, background dielectric and the integrated spatial filter, respectively.

In ACI, loss compensation can be performed by introducing an additional material between the object plane and the lens as shown in Fig. 5.1(b). This material should behave as a tunable active band-pass spatial filter [26, 28]. We write the transfer

function of the spatial filter as [27]

$$a(k_y) = b + G(k_y), \qquad (5.1)$$

where we set b as a real constant corresponding to a uniform low background trans-mission. $G(k_y) = |G(k_y)|e^{i\varphi(k_y)}$ is a complex band-limited function with phase $\varphi(k_y)$ and describes the pass-band of the passive filter. If the amplitude of the wave il-luminating the system is increased by a factor $A_0 = b^{-1}$, the resulting transmitted spectrum is

$$A(k_y) = 1 + A_0 G(k_y). \qquad (5.2)$$

Eq. 5.2 is defined as the transfer function of the active spatial filter [27]. The term "active spatial filter" simply refers to the process of physically providing increased energy to the passive filter with the transfer function in Eq. 5.1. In other words, linear transmission through passive materials is considered. The word active also distinguishes ACI from purely deconvolution based methods [32, 33, 34, 35] where no additional energy is provided to the system.

The response of the active spatial filter should be shift invariant along the object plane and integrating the filter with the lens should allow the entire system to be described with an active transfer function [26, 28] written as

$$T_A(k_y) = T(k_y)[1 + A_0 G(k_y)], \qquad (5.3)$$

where $T(k_y)$ is the passive transfer function of the silver lens.
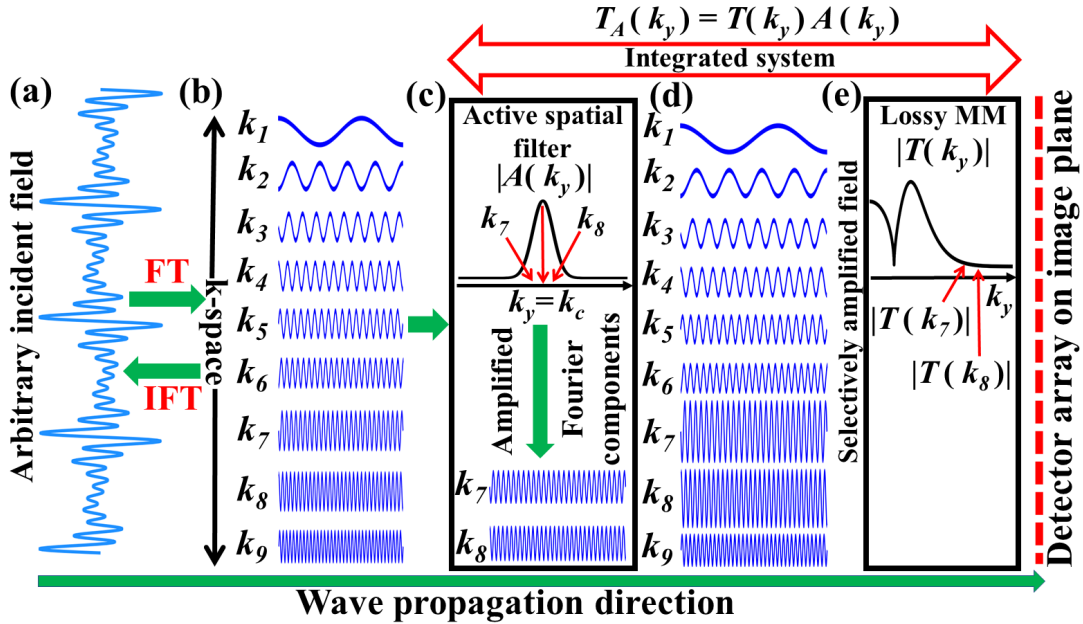
Figure 5.2: Conceptual schematic of ACI emphasizing the underlying physics of the loss compensation process. (a) An arbitrary incident field is (b) a weighted superposition of different harmonics. After propagating though (c) the active spatial filter, the amplitudes of a few selected harmonics (e.g., k_7 and k_8) are amplified relative to the others based on the transfer function of the filter given by Eq. 5.2 and depicted by the inset in (c). (d) The modified field incident on (e) the lossy MM contain the amplified spatial frequencies (origin of auxiliary source), superimposed with the unaltered harmonics. The estimated amplification provided to the selected harmonics can be the inverse of their passive transmission amplitudes (e.g., $T(k_7)$ and $T(k_8)$ in the inset). This would ensure that they survive the lossy transmission process through the MM.

The Eqs. 5.2 and 5.3 are central to the ACI loss compensation process. The physical picture is best illustrated with the aid of the schematic shown in Fig. 5.2. An arbitrary field incident on the system, shown in Fig. 5.2(a) can be described as a linear, weighted superposition of harmonics or spatial frequencies shown in Fig. 5.2(b). The active spatial filter in Fig. 5.2(c) is inserted between the lossy MM in

Fig. 5.2(e) and the incident field. The transfer function of the active filter has the form of Eq. 5.2 and the amplitude $|A(k_y)|$ is depicted in the inset in Fig. 5.2(c). The transmission amplitude of a lossy MM, which deteriorates for increasing spatial frequencies, is illustrated by the inset in Fig. 5.2(e). For example, assume that the spatial frequencies k_7 and k_8 will be compensated. ACI achieves this by tuning the center frequency, k_c of the active spatial filter such that $|A(k_y)| > 1$ over the identified spatial frequencies. This is illustrated by the inset in Fig. 5.2(c). After the harmonics of the incident field propagate though the active spatial filter, the amplitudes of the identified spatial frequencies are amplified relative to the other harmonics. Therefore, the field exiting the active filter contains the original harmonics of the object superimposed with the selectively amplified harmonics k_7 and k_8 [see Fig. 5.2(d)]. The amplification provided to these harmonics (controlled by A_0) is adjusted to ensure that they survive the lossy transmission process through the MM. The selectively amplified spatial frequencies at the exit of the filter constitute the auxiliary source as discussed in [26] and is conceptually similar to [20] with the only difference being the generation process, which here like in [26] employs the active spatial filter to simply modify the original field incident on the MM by a convolution operation.

Using numerical simulations, ACI was implemented with an experimentally realized silver superlens [60] at the wavelength $\lambda = 365\,\text{nm}$. A physical system approximating the properties of the active spatial filter was designed with aluminium-dielectric

multilayered structures which exhibit hyperbolic dispersion [27]. The above theoretical formulation was tested by integrating the multilayered structure with the lens as shown in Fig. 5.1(b). Imaging results with coherent [28] and incoherent [42] illumination showed an improvement in the resolution limit of the lens even under the presence of noise. The HMMs used in [28, 42] were designed to act as the spatial filter in Fig. 5.1(b), such that their transmission properties closely approximate Eq. 5.2 under high intensity illumination.

5.3 Variance in the Fourier Domain

To start with, let the image plane has a length L along the y-axis [see Fig. 5.3(a)]. A continuous signal $i(y)$, along the image planes is measured by a detector which can be an array of pixels or a scanning near-field probe. Based on the setup in Fig. 5.1, $i(y)$ represents TM-polarized field. An arbitrary spatial field distribution is decomposed into M discrete samples at intervals of Δy where M is an even integer. The above spatial decomposition is represented by the segmented line in Fig. 5.3(a) where each segment is defined as a pixel. An integer p satisfying $-\frac{M}{2} \leq p \leq \frac{M}{2} - 1$ uniquely identifies each pixel centered at $y(p) = p\Delta y \equiv \xi$. This relates the discrete space ξ to continuous space y. The signal sampled by the pth pixel is denoted by $i(\xi)$. In subsequent calculations we will set $L = 80\lambda$ with $\lambda = 365\,\text{nm}$ and $M = 5840$. Therefore, the sampling interval is $\Delta y = 5\,\text{nm}$ which is slightly larger than

previously demonstrated apertureless probes which can achieve resolutions down to 1 nm [61]. The resulting noisy image at each pixel is described with a popular signal-modulated noise model [62, 63, 64, 65, 66]. The image plane is thought of as an array of statistically independent random variables (RVs) and the subsequent noisy image at the pth pixel is denoted by

$$i_n(\xi) = \left[|i(\xi)| + n_{sd}(\xi)\right]e^{i\theta(\xi)}. \tag{5.4}$$

$i(\xi)$ is the noiseless field at the image plane and is corrupted by signal-dependent (SD) noise process $n_{sd}(\xi)$. The discussion of signal-independent noise can be found in [26, 27]. The RV $n_{sd}(\xi)$ in Eq. 5.4 has zero mean, Gaussian probability density function, and standard deviation $f\{|i(\xi)|\}^\gamma \sigma_{sd}$, where σ_{sd} is a constant. $\theta(\xi)$ is the phase of the noiseless coherent field $i(\xi)$ at the pth pixel (i.e., $\xi \equiv p\Delta y$). A correction due to the shift in the zero-optical-path difference point based on an interferometric setup was not included in our model. $f\{|i(\xi)|\}^\gamma$ is a function of the ideal image amplitude and is referred to as the modulation function [62]. γ is a parameter satisfying $0 \le \gamma \le 1$ [63]. The variance at each pixel is,

$$\sigma_{\xi_p}^2 = f\{|i(\xi)|\}^{2\gamma}\sigma_{sd}^2. \tag{5.5}$$

The modulation function and the value of γ are selected to best mimic the behavior of SD noise which affects the system.

143

The above detection process results in a similar decomposition of the continuous Fourier spectrum of $i(y)$ into M discrete spatial frequencies as illustrated by the segmented line in Fig. 5.3(b). Two adjacent frequencies are separated by Δk_y and the individual spatial frequencies are referenced by $k_y(q) = q\Delta k_y \equiv \zeta$, where $-\frac{M}{2} \leq q \leq \frac{M}{2} - 1$. This relates the discrete Fourier space ζ to continuous Fourier space k_y. The Fourier transform of the discretized noise-free image, $i(\xi)$, is denoted by $I(\zeta)$, and the standard deviation at the qth spatial frequency is σ_{ζ_q}. Knowledge of σ_{ζ_q} is particularly useful in determining the maximum achievable limiting resolution for optical systems where transmission progressively worsens for high spatial frequencies. For example, the Fourier components with transmitted amplitudes comparable to, or less than σ_{ζ_q} will be indiscernible from random noise fluctuations within the measured signal. Therefore, σ_{ζ_q} allows us to identify the spatial frequencies whose Fourier domain information is effectively lost due to noise effects. Additionally, the effectiveness of a loss compensation technique can also be evaluated by monitoring its effect on σ_{ζ_q}. Thus, a formulation of σ_{ζ_q} is important for our understanding of the underlying mechanism of ACI and its capacity at compensating losses while minimizing noise amplification.

A general expression for the standard deviation at the qth spatial frequency can be calculated by approximating the analytical Fourier transform relation as a Riemann sum [67]. The Fourier transform of the noisy image $i_n(\xi)$ in Eq. 5.4 is then written
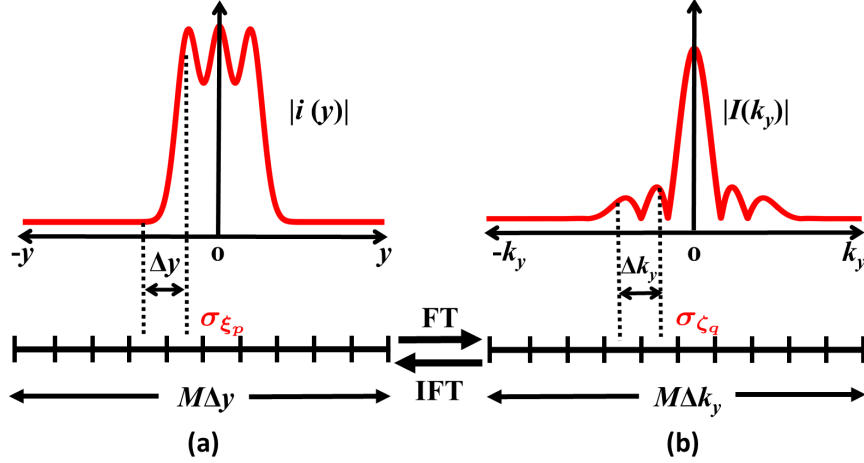
Figure 5.3: Illustration of an image measurement process in a detector system. (a) The continuous field $i(y)$ along the image plane of length L is decomposed into M samples at intervals of Δy. Each sample is identified by an integer p. During the detection process, noise degrades the ideal image and the standard deviation at each sample is σ_{ξ_p}. $|i_n(\xi)|$ is the magnitude of the recorded image at the pth pixel or $y = p\Delta y \equiv \xi$ spatial coordinate. (b) The Fourier spectrum of $i(\xi)$ is similarly a decomposition into M spatial frequencies and σ_{ζ_q} is the standard deviation at the qth frequency.

as

$$
\begin{aligned}
I_n(\zeta) &= \sum_{\xi=-\frac{M}{2}\Delta y}^{(\frac{M}{2}-1)\Delta y} |i_n(\xi)| e^{i\theta(\xi)} \exp\left(-i\xi\zeta\right) \Delta y \\
&= \sum_{\xi=-\frac{M}{2}\Delta y}^{(\frac{M}{2}-1)\Delta y} |i_n(\xi)| \left\{ \cos\left(\theta(\xi) - \xi\zeta\right) \right. \\
&\quad \left. + i\sin\left(\theta(\xi) - \xi\zeta\right) \right\} \Delta y \\
&= I_n'(\zeta) + iI_n''(\zeta)
\end{aligned}
\tag{5.6}
$$

with real and imaginary parts $I_n'(\zeta)$ and $I_n''(\zeta)$, respectively. Note that the number of samples M, is related to Δy and Δk_y by $M = 2\pi/\Delta y\Delta k_y$ [67]. We can substitute

145

$|i_n(\xi)|$ from Eq. 5.4 into Eq. 5.6 to express the real and imaginary parts of $I_n(\zeta)$ as

$$I_n'(\zeta) = \sum_{\xi = -\frac{M}{2}\Delta y}^{(\frac{M}{2}-1)\Delta y} \left\{ |i(\xi)| + n_{sd}(\xi) \right\} \cos[\phi(\xi, \zeta)]\Delta y, \tag{5.7}$$

and

$$I_n''(\zeta) = \sum_{\xi = -\frac{M}{2}\Delta y}^{(\frac{M}{2}-1)\Delta y} \left\{ |i(\xi)| + n_{sd}(\xi) \right\} \sin[\phi(\xi, \zeta)]\Delta y, \tag{5.8}$$

respectively, and $\phi(\xi, \zeta) = \theta(\xi) - \xi\zeta$.

Based on Eq. 5.6, we can write $I_n(\zeta)$ as

$$I_n(\zeta) = I(\zeta) + N_{sd}(\zeta), \tag{5.9}$$

where $I(\zeta)$ and $N_{sd}(\zeta)$ are the Fourier transforms of $i(\xi)$ and $n_{sd}(\xi)$ in Eq. 5.4, respectively. The real and imaginary parts of $I(\zeta)$ and $N_{sd}(\zeta)$ can also be expressed in terms of the sums of cosines and sines similar to $I_n(\zeta)$ (see Eqs. 5.7 and 5.8). $N_{sd}(\zeta)$ in Eq. 5.9 has a standard deviation σ_{ζ_q} describing SD noise at the qth Fourier component. The variance of the real and imaginary parts of $N_{sd}(\zeta)$ are denoted by $\sigma_{\zeta_q,r}^2$ and $\sigma_{\zeta_q,i}^2$, respectively. According to Eqs. 5.6 and 5.9 $N_{sd}(\zeta)$ is a weighted superposition of all the RVs in the spatial domain. Each RV involved in the summation is statistically independent with a Gaussian probability density function. Therefore, we can apply

Bienaymé's identity, to express $\sigma^2_{\zeta_q,r}$ and $\sigma^2_{\zeta_q,i}$ as

$$\sigma^2_{\zeta_q,r} = \sum_{\xi=-\frac{M}{2}\Delta y}^{(\frac{M}{2}-1)\Delta y} \sigma^2_{\xi_p} \cos^2[\phi(\xi,\zeta)](\Delta y)^2, \tag{5.10}$$

and

$$\sigma^2_{\zeta_q,i} = \sum_{\xi=-\frac{M}{2}\Delta y}^{(\frac{M}{2}-1)\Delta y} \sigma^2_{\xi_p} \sin^2[\phi(\xi,\zeta)](\Delta y)^2, \tag{5.11}$$

respectively, and $\sigma^2_{\xi_p} = f\{|i(\xi)|\}^{2\gamma}\sigma^2_{sd}$. The overall variance at each spatial frequency is simply the sum of the variances of the real and imaginary parts in Eqs. 5.10 and 5.11, that is

$$\sigma^2_{\zeta_q} = \sum_{\xi=-\frac{M}{2}\Delta y}^{(\frac{M}{2}-1)\Delta y} f\{|i(\xi)|\}^{2\gamma}\sigma^2_{sd}(\Delta y)^2. \tag{5.12}$$

Without loss of generality, the subsequent calculations can be simplified and provide more physical insight by assuming the modulation function in Eq. 5.12 is a linear function of $|i(\xi)|$ with $\gamma = 1$. This results in constant SNR and has implications on the considered noise levels and required illumination intensities. This is chosen to relate the variance directly to the total physical power contained in the signal as shown below. Similar effects are obtained, such as in practical detectors with the Poisson distribution of photon noise [42, 45, 62]. Substituting $f\{|i(\xi)|\} = |i(\xi)|$ and

$\gamma = 1$ we can rewrite Eq. 5.12 as

$$\sigma_{\zeta_q}^2 = \left[\sum_{\xi=-\frac{M}{2}\Delta y}^{(\frac{M}{2}-1)\Delta y} |i(\xi)|^2 \sigma_{sd}^2 \Delta y \right] \Delta y. \qquad (5.13)$$

The summation enclosed inside brackets, is proportional to the optical power on the image plane. Therefore, we can employ the energy conservation theorem by using Parseval's relation and rewrite $\sigma_{\zeta_q}^2$ in Eq. 5.13 as

$$\sigma_{\zeta_q}^2 = \left[\frac{1}{2\pi} \sum_{\zeta=-\frac{M}{2}\Delta k_y}^{(\frac{M}{2}-1)\Delta k_y} |I(\zeta)|^2 \sigma_{sd}^2 \Delta k_y \right] \Delta y$$

$$= \frac{1}{M} \sum_{\zeta=-\frac{M}{2}\Delta k_y}^{(\frac{M}{2}-1)\Delta k_y} |I(\zeta)|^2 \sigma_{sd}^2. \qquad (5.14)$$

Eqs. 5.13 and 5.14 state, for a fixed number of pixels $M = 2\pi/\Delta y \Delta k_y$, that the spectral variance $\sigma_{\zeta_q}^2$ is constant and proportional to the total power contained in the signal. Similar results have been reported for incoherent light in [68, 69, 70]. This is a remarkable result, which can be potentially generalized to a wide variety of problems in noisy and lossy linear systems, either classical or quantum. Below, in the context of superresolution imaging, we demonstrate how this result leads to enhanced spectral SNR with the incorporation of selective spectral amplification and correlations. For different values of γ, the variance is still flat, but not proportional to the power contained in the signal (see Eq. 5.12). To the best of our knowledge,

the utilization of Eqs. 5.13 and 5.14 in imaging has only been drawn attention to here and in a slightly modified form recently in [69] to extend the SNR limit using sub-pupils.

The presence of an extra Δy clearly makes $\sigma^2_{\zeta_q}$ dependent on the spatial discretization. Rescaling Δy in Eq. 5.14 would result in effects of upsampling or downsampling of continuous signals. Therefore, Eq. 5.14 cannot be readily generalized for an arbitrary detector system without considering the physical mechanism through which information is extracted. The spectral variance may not necessarily reduce with pixel miniaturization and multiple factors must also be considered when determining the overall effect on noise. The number of detected photons are also intimately related to the pixel active area, quantum efficiency, the pixel optical path, integration time, and sensitivity [71, 72, 73, 74]. Additionally, it may be necessary to incorporate crosstalk effects between adjacent pixels to accurately model the effect of pixel scaling on $\sigma^2_{\zeta_q}$. However, the effects of pixel miniaturization on the detected noise are considered independent from ACI, which only deals with compensation of signal losses for a fixed number of pixels.

In subsequent discussions, an analytical equation [75] is used for the transfer function of the silver lens imaging system, which is configured similar to an experimental silver lens [60] with $d = 50\,\text{nm}$ and embedded inside a background dielectric of relative permittivity $\epsilon_d = 2.5$ [27, 28, 42] [see Figs. 5.1(a) and 5.4]. The relative permittivity
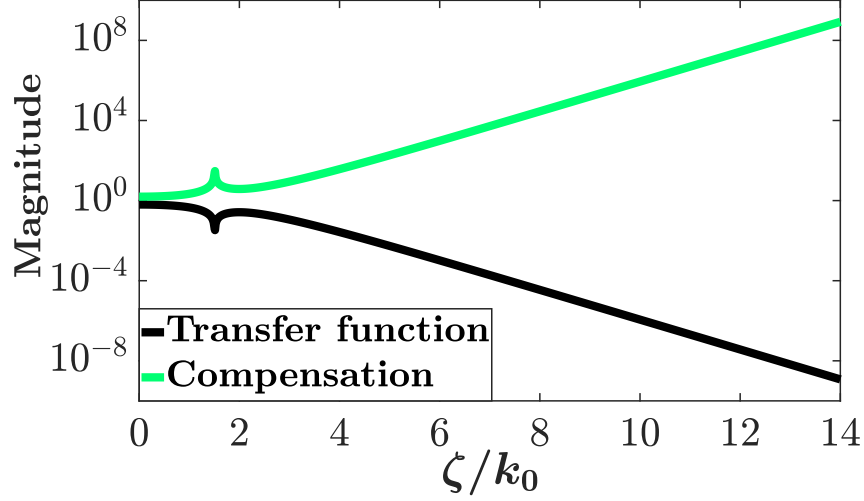
Figure 5.4: Magnitude of the analytical transfer function for a 50 nm thick silver lens embedded inside a dielectric and symmetrically placed between the object and image planes as shown in Fig. 5.1(a). The required compensation at each Fourier component should ideally be the inverse of the transfer function and is shown by the green line.

of silver at $\lambda = 365$ nm is $\epsilon_{Ag} = -1.88 + 0.60i$, calculated from the Drude-Lorentz model [76]. The corresponding estimated compensation necessary for each spatial frequency is simply the inverse of the corresponding magnitude of transmission (see Fig. 5.4). In Fig. 5.4 and following ones negative spatial frequencies are not shown, although the full spectrum is considered in all the calculations.

5.4   Results

5.4.1   Selective spectral amplification and correlations

In the following, an example object with a Gaussian spectrum is employed in Figs. 5.5 and 5.6, defined as

$$|O(\zeta)| = \exp\left[\frac{-\zeta^2}{2\alpha^2}\right], \tag{5.15}$$

where α describes the full width at half maximum (FWHM) of $|O(\zeta)|$ and is defined as

$$\alpha = \frac{0.25 M \Delta k_y}{2\sqrt{2\ln 2}}. \tag{5.16}$$

The imaging systems are illuminated with a TM-polarized source from the object plane (see Fig. 5.1). We assume that the object field is created through subwavelength slits [3, 77]. The spatially coherent discretized complex magnetic field distribution along the object plane is denoted as $o(\xi)$. The Fourier transforms of the noiseless image for the passive (i.e., without ACI) and active (i.e., with ACI) imaging systems

are

$$I_P(\zeta) = O(\zeta)T(\zeta), \tag{5.17a}$$

$$I_A(\zeta) = O(\zeta)T(\zeta)[1 + A_0 G(\zeta)], \tag{5.17b}$$

respectively, where $O(\zeta) = \mathcal{F}\{o(\xi)\}$ and $\mathcal{F}$ is the Fourier transform operator. The subscripts "P" and "A" refer to the passive and active imaging systems, respectively. $O(\zeta)A_0 G(\zeta)$ in Eq. 6.3b is defined as the auxiliary source [26, 27, 28] (see Fig. 5.2). Therefore, $O(\zeta)T(\zeta)A_0 G(\zeta)$ is the residual auxiliary source which survived the lossy transmission process through the lens. As can be seen from Eq. 6.3b, the object field $O(\zeta)$ is superimposed coherently with the auxiliary source. The auxiliary source is required to possess three important properties. First, it is correlated with the object field $O(\zeta)$ [26]. Second, it is defined over a finite bandwidth through $G(\zeta)$. Third, it is amplified by a factor of A_0. Below, without loss of generality, we use a band-limited unit magnitude rectangular function for $G(\zeta)$. Then, overall, the auxiliary source corresponds to only a portion of the object spectrum, which is selectively amplified. However, in general, the function $G(\zeta)$ can have an arbitrary profile with a finite bandwidth [27]. In this case, the auxiliary source spectrum is modified in accordance with the given function $G(\zeta)$, while being still selectively amplified and correlated with the object. In [27] and [28], we show how to construct such an auxiliary source using HMMs acting as near-field spatial filters.

The standard deviations at the qth Fourier component corresponding to $I_P(\zeta)$ and $I_A(\zeta)$ in Eq. 6.3 are denoted by $\sigma_{\zeta_q,P}$ and $\sigma_{\zeta_q,A}$, respectively. Their expressions are determined by substituting $|I(\zeta)|$ in Eq. 5.14 with $|I_P(\zeta)|$ and $|I_A(\zeta)|$, respectively. That is

$$\sigma_{\zeta_q,P}^2 = \frac{1}{M} \sum_{\zeta=-\frac{M}{2}\Delta k_y}^{(\frac{M}{2}-1)\Delta k_y} |O(\zeta)T(\zeta)|^2 \sigma_{sd}^2, \tag{5.18}$$

and

$$\sigma_{\zeta_q,A}^2 = \frac{1}{M} \sum_{\zeta=-\frac{M}{2}\Delta k_y}^{(\frac{M}{2}-1)\Delta k_y} |O(\zeta)T(\zeta)|^2 \sigma_{sd}^2 |1 + A_0 G(\zeta)|^2$$

$$= \sigma_{\zeta_q,P}^2 + \sigma_{\zeta_q,Aux}^2. \tag{5.19}$$

Note that $\sigma_{\zeta_q,A}^2$ can be split into its contributing parts. $\sigma_{\zeta_q,Aux}^2$ describes the contribution to the SD noise from the residual auxiliary source and is given by

$$\sigma_{\zeta_q,Aux}^2 = \frac{1}{M} \sum_{\zeta=-\frac{M}{2}\Delta k_y}^{(\frac{M}{2}-1)\Delta k_y} |O(\zeta)T(\zeta)|^2 A_0^2 \sigma_{sd}^2$$

$$\times \left[\frac{2G'(\zeta)}{A_0} + |G(\zeta)|^2 \right], \tag{5.20}$$

where $G'(\zeta)$ is the real part. Eqs. 5.18 and 5.19, say that integrating the active spatial filter with the imaging system gives an additional standard deviation $\sigma_{\zeta_q,Aux}$, dependent on the filter parameters. Eq. 5.20 shows how the active filter parameters,

such as A_0, the center frequency q_c, and the width of $G(\zeta)$ contribute to the noise at each Fourier component. Before proceeding further, we reduce Eq. 5.20 to

$$\sigma_{\zeta_q,Aux}^2 \approx \frac{1}{M} \sum_{\zeta=-\frac{M}{2}\Delta k_y}^{(\frac{M}{2}-1)\Delta k_y} |O(\zeta)T(\zeta)|^2 A_0^2 \sigma_{sd}^2 |G(\zeta)|^2, \qquad (5.21)$$

since the summation of the first term inside the brackets in Eq. 5.20 can be generally dropped. For example, consider compensating the spatial frequencies $10k_0 \leq \zeta \leq 12k_0$. According to the green line in Fig. 5.4, the estimated value for A_0 is approximately within the order $10^6 \sim 10^8$.

For simplicity, we rewrite the transfer function of the active spatial filter in Eq. 5.2 as

$$A_R(\zeta) = 1 + A_0 G_R(\zeta), \qquad (5.22)$$

where $G_R(\zeta) = |G_R(\zeta)|e^{i\varphi_R(\zeta)}$ is a unit magnitude rectangular function of width $W k_0$ and centered at ζ_c. That is

$$|G_R(\zeta)| = \begin{cases} 1 & \left|\frac{(\zeta-\zeta_c)}{W k_0}\right| \leq \frac{1}{2} \\ 0 & \texttt{otherwise.} \end{cases} \qquad (5.23)$$

This redefinition conveniently emphasizes the effect of selective spectral amplification without loss of generality. Then, we can express the ratio R_σ of $\sigma_{\zeta_q,Aux}^2$ in Eq. 5.21

154

to $\sigma^2_{\zeta_q,P}$ in Eq. 5.18 as

$$R_\sigma = A_0^2 \frac{P_{I_P,W}}{P_{I_P}}, \tag{5.24}$$

where $P_{I_P,W}$ is the portion of the total power contained by $I_P(\zeta)$ distributed over

bandwidth Wk_0 and centered at ζ_c, and P_{I_P} is the total power contained by $I_P(\zeta)$.

Thus, it is important to note that Eq. 5.24 is the ratio of the power in the selectively

amplified band to the total power in the noiseless signal without selective amplifi-

cation. This ratio should not be too large to prevent excessive noise amplification.

Consider, for example, the case where the Fourier components within $6k_0 \leq \zeta \leq 8k_0$
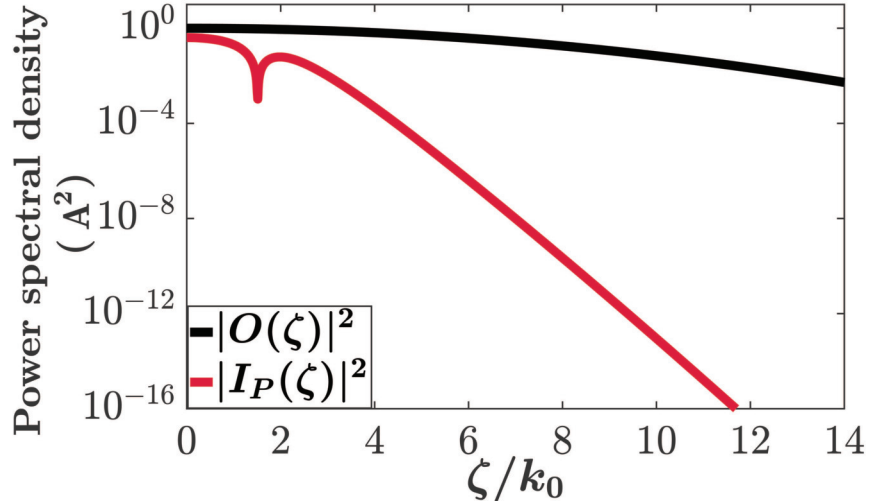
Figure 5.5: The power spectral densities of the object ($|O(\zeta)|^2$) and the passive image ($|I_P(\zeta)|^2$) showing how the total power contained within the Gaussian object and image is distributed throughout the Fourier spectrum.

are selected for amplification. We set $A_0 = 10^4$ to guarantee the recovery of this

entire band. This overcompensates the lower spatial frequencies within the band.

From Eq. 5.24 the ratio R_σ evaluates to about 13. This indicates that even though

Fourier components were strongly amplified, the resultant increment in the spectral

variance is comparatively small. This can be generalized for an arbitrary ζ_c. Fig. 5.5 shows the power spectral density (PSD) plots for $|O(\zeta)|^2$ and the corresponding $|I_P(\zeta)|^2 = |O(\zeta)T(\zeta)|^2$ indicated by black and red lines, respectively. Since $|T(\zeta)|$ decays with increasing q (see black line in Fig. 5.4), the PSD of $I_P(\zeta)$ clearly follows a similar trend. Most of the power contained within the image is distributed over a small portion of the Fourier spectrum. For example, if the previously selected band is modified to $8k_0 \leq \zeta \leq 10k_0$, $P_{I_P,W}$ in Eq. 5.24 will decrease as can be seen from Fig. 5.5. However, P_{I_P} will remain the same and therefore, the ratio between $P_{I_P,W}$ and P_{I_P} decreases. This conveniently restricts R_σ from becoming large even though the Fourier components within $8k_0 \leq \zeta \leq 10k_0$ require larger amplification compared to the previous example.

Based on R_σ in Eq. 5.24 the ACI technique suggests, in principle, an infinite resolution. Because there is a trade-off between the illumination intensity and the bandwidth of the passive spatial filter to keep the spectral SNR above $0\,\mathrm{dB}$ at an arbitrarily large spatial frequency in the loss compensated image spectrum. Once the SNR is above $0\,\mathrm{dB}$ for a particular spatial frequency, that particular frequency of the image can be reconstructed with deconvolution using the active transfer function in Eq. 5.3. The larger the illumination intensity, the smaller the bandwidth should be to suppress the noise amplification. However, in practice the resolution is limited by several factors: maximum power, minimum bandwidth and maximum center frequency of the passive spatial filter, and the minimum pixel size. Also, the present model of

ACI does not consider weak signals, which should be treated with a quantum optical model [78].

5.4.2 Improving SNR and resolution limits

The above inhibition of noise amplification during the compensation process results in substantial improvement in system performance [26, 28, 42]. This is investigated by comparing between the spectral SNR of the passive and active systems. A general expression for the spectral SNR is

$$SNR(\zeta) = \frac{|I(\zeta)|}{\sigma_{\zeta_q}}. \tag{5.25}$$

Substituting the constant A_0 with a functional form $A_0(\zeta) = |T(\zeta)|^{-1}$ allows optimal amplification for full compensation of losses within Wk_0 bandwidth and is adopted below to emphasize the relative importance of the selective amplification rather than the exact functional form. Alternatively, a Gaussian or log-normal form of $|G_R(\zeta)|$ can also be used to better describe the previously considered MM spatial filters [27, 28]. Additionally, for the remainder of this work we will use $\sigma_{sd} = 10^{-3}$ in the signal-modulated noise model in Eq. 5.4 for consistency with our previous works [26, 27, 28, 42], where an experimental imaging system detector [79] is considered.

Based on Eqs. 6.3 and 5.25, the SNR of the passive and active imaging systems $SNR_P(\zeta)$ and $SNR_A(\zeta)$, respectively, are written as

$$SNR_P(\zeta) = \frac{|O(\zeta)T(\zeta)|}{\sigma_{\zeta_q,P}}, \tag{5.26}$$

and

$$SNR_A(\zeta) = \frac{|O(\zeta)T(\zeta)||1 + A_0(\zeta)G_R(\zeta)|}{\sigma_{\zeta_q,A}}, \tag{5.27}$$

respectively. $SNR_P(\zeta)$ is plotted by the black line in Fig. 5.6 and $SNR_A(\zeta)$ for filters with $W = 1, 3, 4$, and 6 by the pink, green, blue and purple lines, respectively. Note that ζ_c is kept constant at $10k_0$ and the dashed yellow line marks $SNR = 0 \, \text{dB}$. The intersection of $SNR_P(\zeta)$ with the dashed line marks the resolution limit of the passive system since larger Fourier components will be indistinguishable from noise in the detected signal. However, $SNR_A(\zeta)$ shows a remarkable improvement especially within the regions where compensation is provided. We point out that $SNR_A(\zeta)$ is less than $SNR_P(\zeta)$ outside the selected bands as expected, since the additional noise from $\sigma_{\zeta_q,Aux}$ affects the entire spectrum (see Eq. 5.14). This contribution increases with W as is evident from Fig. 5.6. Nevertheless, the additional increment in the spectral variance is significantly smaller than the amplification provided to each Fourier components inside the selected bands, which results in an impressive enhancement in SNR. The purple line is particularly interesting since it encapsulates the remarkable power of ACI. The rectangle function $|G_R(\zeta)|$, in this case, spans a

fairly broad $6k_0$ bandwidth and has essentially extended the resolution limit of the system close to double compared to the passive system.
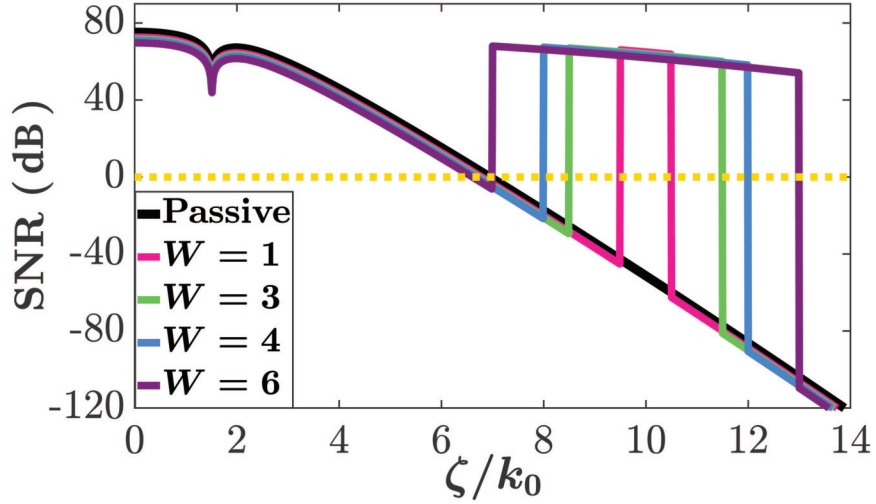
Figure 5.6: SNRs of the passive (black line) and active imaging systems (pink, green, blue and purple lines) with different W. The effective resolution limit of the passive imaging system is approximately $\zeta = 7k_0$. In contrast, the SNR of the active imaging systems incorporating ACI is increased within the selected bands of each filter. Slightly reduced SNR outside the selected bands indicate the noise contribution from the auxiliary source.

5.4.3 Arbitrary objects

In general, the theory of ACI can be expanded to arbitrary objects. This is illustrated with Fig. 5.7 where the Fourier spectrum of an arbitrary object is plotted by the black line. The corresponding noise-free passive image spectrum is calculated from Eq. 6.3a and corrupted with noise in the spatial domain according to the signal-modulated noise model in Eq. 5.4. The noisy image is then Fourier transformed to

obtain $I_{n,P}(\zeta)$. The magnitudes of $I_P(\zeta)$ and $I_{n,P}(\zeta)$ are shown in Fig. 5.7 by pink

and light green lines, respectively. The standard deviation $\sigma_{\zeta_q,P}$, which has degraded

the passive image spectrum is shown by the dashed dark green line. We can see how

$|I_P(\zeta)|$ progressively worsens with increasing ζ. Eventually, $\sigma_{\zeta_q,P}$ becomes comparable

to $|I_P(\zeta)|$ at approximately $\zeta = 7k_0$ after which $|I_{n,P}(\zeta)|$ is overwhelmed by noise,

similar to the simpler Gaussian object in Fig. 5.6 (see black line). The noise-free

active image spectrum is calculated from Eq. 6.3b taking $\zeta_c = 10k_0$, $W = 4$, and

substituting $A_0 G(\zeta)$ with $A_0(\zeta) G_R(\zeta)$, where $A_0(\zeta) = |T(\zeta)|^{-1}$. This active image

is then also corrupted with noise in the spatial domain and Fourier transformed to

obtain $I_{n,A}(\zeta)$, magnitude of which is shown by the light blue line in Fig. 5.7. The

standard deviation for the active system $\sigma_{\zeta_q,A}$ is shown by the dashed dark blue line.

Fig. 5.7 clearly manifests the noise-resistant effect of the selective amplification. Note

that the missing nodes on the object spectrum are accurately recovered inside the

band $8k_0 \leq \zeta \leq 12k_0$ where the selective amplification is provided. The inhibition of

noise amplification with ACI's selective spectral amplification is therefore applicable

for arbitrary objects. Based on Fig. 5.7, we find that the resolution limit can be

in the end extended by more than 40% when the underlying passive spatial filter is

illuminated with an intensity of about 0.03mW/μm² (i.e., the intensity amplification

factor $A_0^2 \approx 1.6 \times 10^5$). A coherent light around this level of intensity is accessible for

a superresolution imaging experiment with a relatively less lossy MM structure [80].

Retrieving deep subwavelength information from a low-Q system disturbs the system
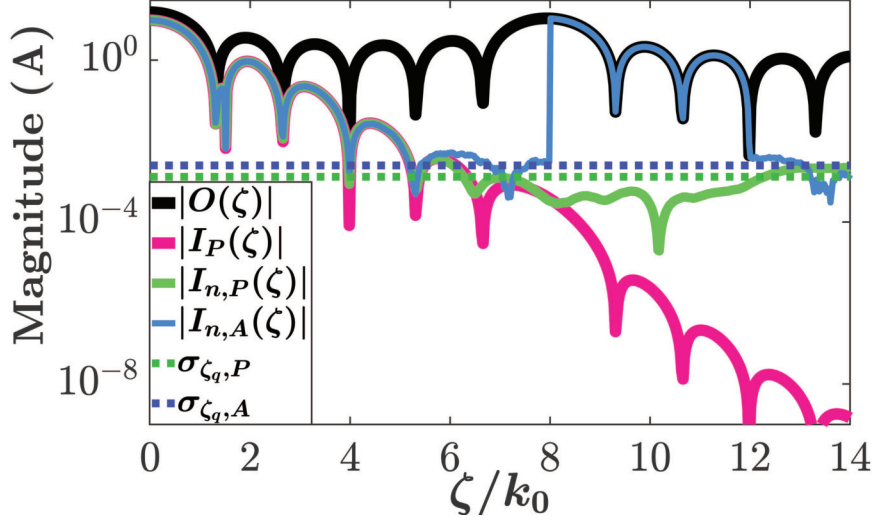
Figure 5.7: Generalization of the ACI to an arbitrary object. The amplitude of the Fourier transforms of the object, the corresponding noise-free and noisy passive images, and the active image are shown by the black, pink, light green and light blue lines, respectively. The standard deviations for the noisy passive image and the active image spectra are shown by the dashed dark green and dark blue lines, respectively. The active image is adequately compensated within $8k_0 \leq \zeta \leq 12k_0$ with a very small amplification of SD noise.

and lets the high spatial frequency modes quickly dissipate. In our calculations we did not include this effect. Therefore, it is necessary to maintain a sufficiently high intensity continuous wave illumination to counter this effect. Here, for simplicity, we consider only one-dimensional imaging. Therefore, the dimension of the pixel along the z-direction can be taken equal to the length L of the image plane. For two-dimensional imaging more intensity is needed. Additional noise and speckle associated with high illumination intensity and small pixel size limit the achievable resolution. Also, the amplification at high spatial frequencies will be difficult in the presence of spatial dispersion. Therefore, the designed spatial filter in Fig. 5.1(b) should support the highest desired spatial frequency. In a future work, an efficient (i.e., low

161

power) implementation could replace the spatial filter in Fig. 5.1(b) with a plasmonic structured illumination [81] that is systematically designed based on Eqs. 5.13 and 5.14. Another possibility could be considered along the lines of [82], where the HMM is used to collect the low and high spatial frequencies at different polarizations. In our model, we assume 60 dB spatial SNR (i.e., $\sigma_{sd} = 10^{-3}$). Since the spectral variance is constant through the image spectrum (see Fig. 5.7) and proportional to σ_{sd}^2, the larger the spatial SNR the lower the required power is to reconstruct a specific spatial frequency.

In the ACI method, once the selective amplification is applied to the spatial frequencies that were previously buried under the noise (see Fig. 5.7), the reconstructed image can be obtained from deconvolution based on the active transfer function (see Eq. 5.3). If the optimal Wiener filter $[1 + 1/SNR_A(\zeta)^2]^{-1}$ [29, 30, 31] is used in the deconvolution step, the reconstructed image can be written as

$$\tilde{O}_{n,A}(\zeta) = I_{n,A}(\zeta) \frac{1}{1 + \frac{1}{SNR_A(\zeta)^2}} \frac{1}{T(\zeta)[1 + A_0 G(\zeta)]}, \qquad (5.28)$$

assuming a constant A_0 and general pass-band function $G(\zeta)$. For high $SNR_A(\zeta)$ (i.e., around low spatial frequencies and regions of selective amplification), this deconvolution process approaches to "active inverse filtering." For low $SNR_A(\zeta)$ (e.g., around $7k_0$ and $13k_0$ in Fig. 5.7), the optimal Wiener filter does not heavily amplify

the noise as opposed to the inverse filter [29]. In general, the optimal Wiener filter employs the image SNR (see Eq. 5.28) to prevent excessive noise amplification [30, 31]. In this regard, the selective amplification in the ACI method has also a similar spirit as the optimal Wiener filter. However, as shown below in Fig. 5.8, with the ACI even without the optimal Wiener filter one can restore spatial frequencies that cannot be restored by a typical optimal Wiener deconvolution [29, 30, 31]. This is achieved by selectively amplifying those spatial frequencies, while preventing excessive noise amplification in accordance with Eqs. 5.13 and 5.14. Furthermore, as given in Eq. 5.28, when the optimal Wiener filter is integrated with the ACI, this extends the restored spatial frequency range of the optimal Wiener filter.

Fig. 5.8 compares the passive and active reconstructed images and their corresponding spectra for 4 Gaussian objects separated by 18 nm peak-to-peak distance. The yellow line corresponds to the unresolved passive image reconstructed with the optimal Wiener filter. The images reconstructed with the ACI are shown with the red and purple lines in Fig. 5.8(b). The purple line highlights the effect of discretization assuming $\Delta y = 5$ nm. Consistent with Eq. 5.14, the noise is increased with larger discretization. It is clearly seen that the objects are fully resolved using ACI, with a resolution better than $\lambda/20$. The selective amplification process of ACI is achieved by 2 overlapping Gaussian pass-bands with FWHMs of $2.3k_0$ and centered at $7k_0$ (i.e., near the resolution limit of the passive system) and $8.5k_0$. The incident plane wave illumination amplitude [see Fig. 5.1(b)] is increased by a constant factor of $A_0 = 630$.

Finally, the reconstructed images are obtained from deconvolution based on the active transfer function (see Eq. 5.3) and using the noisy active image spectrum $I_{n,A}(\zeta)$ [see blue line in Fig. 5.8(a)].

5.5 Discussion and Conclusion

The ACI is more than a loss compensation in MMs or plasmonics. The ACI concept, the then-called Π scheme, was first numerically demonstrated as a loss compensation method in a plasmonic NIM [20], but later rapidly evolved into a scheme for the mitigation of information loss in noisy and lossy linear systems. The ACI has, since, turned into a scheme for spectrum manipulation using selective amplification and correlations [26, 28, 42].

In this work, we have presented a mathematical analysis of the conceptual framework of ACI. We showed that selective amplification of a controllable band of spatial frequencies with an auxiliary source can provide sufficient amplification to previously attenuated spatial frequencies with minimal amplification of noise. It is important to emphasize that the amplification process in the theory of ACI described here is fundamentally different than the traditional optical gain media and does not require a quantum optical model. The ACI is more feasible than optical gain or nonlinear media, which are more complex and cumbersome due to pumping, gain saturation,

or amplified spontaneous emission (ASE) [78, 83]. In the coherent model of ACI, the amplification of the spatial frequencies within the selected band (see Figs. 5.6 and 5.7) is achieved by the coherent superposition of the original object field with an external auxiliary source, which is correlated with the object field (see Eq. 6.3). Possible physical generations of the auxiliary source relying on the HMMs and injection of plasmons have been studied in detail in our previous works [20, 27, 28]. The implementations for far-field imaging can be made possible with, for example, structured illumination [68] and spatial filtering [45, 69]. Thus, the ACI does not suffer from the severe adverse effect of ASE on the SNR associated with the amplification of weak signals using optical gain media [78, 83]. Also, the imaging system here employs amplification (e.g., by using a brighter source) prior to the lossy transmission to avoid the difficulty with the signal amplification at the detection side, especially for the retrieval of higher spatial frequencies, and is operated with stronger signals. Moreover, the classical correlations play an important role in ACI [26, 36]. In practice, the ACI may not necessarily need increased input power or a separate auxiliary source, but may only need to locally (selectively) amplify the signal spectrum by redistributing the spatial frequency content [45, 69].

The present model of ACI is based on linear systems. Therefore, ACI can also compensate the adverse effect of nonlocality [84] on the imaging performance of the system, as long as the nonlocal system operates in the linear regime. However, since such a

nonlocal system has a poor transfer function compared to the one without spatial dispersion, it will be more difficult to extend the resolution limit. On a similar token, we have previously shown in [35] that an adverse effect of a deviation from homogeneous effective medium approximation can also be compensated with ACI.

We provided a detailed analytical explanation of the role and importance of the various aspects of ACI for greater insights into the previous results [26, 28]. The same mathematical framework can be further expanded to include incoherent illumination [42, 45, 68, 69] using the Wiener-Khinchin theorem. We believe that this work can also theoretically explain the other numerical and experimental results presented in independent works including pattern uniformity in lithography [40], high-resolution Bessel beam generation [39], and acoustic real-time subwavelength edge detection [85], and fosters further explanation of recent simulation and experimental results in far-field imaging [68, 69].

Eqs. 5.13 and 5.14 can also be used to explain why dark-field imaging [86, 87, 88] improves the contrast. Blocking the low spatial frequencies reduces the power contained in the signal, hence the flat variance in the Fourier spectrum. Because the high spatial frequencies are not blocked, however, the spectral SNR increases in this region, hence the image contrast. In contrast, as can be seen from the active transfer function in Eq. 5.3, the ACI does not aim to block low spatial frequencies. It rather aims to selectively amplify the high spatial frequencies buried under the noise without

166

excessive noise amplification. Therefore, it does not sacrifice brightness or strongly enhance artifacts unlike dark-field imaging [87]. The theory presented here can also be applied to bright field imaging. Guided by Eqs. 5.13 and 5.14, the high spatial frequencies can be recovered with the selective amplification.

Revealed from the simple mathematical result in Eq. 5.14, we conjecture that the theoretical concepts of ACI can be potentially generalized to numerous scenarios in noisy and lossy linear systems (e.g., atmospheric imaging [46, 47, 48, 49], bioimaging [89], deep-learning based imaging [90], structured illumination [68], tomography [91], time-domain spectroscopy [50, 51], free space optical communications [52, 53, 54, 55], $\mathcal{PT}$ symmetric non-Hermitian photonics [21, 56, 57], and quantum computing [49, 58, 59], etc.) at different frequencies. Since ACI operates down at the physical layer, all of these scenarios should benefit from ACI for improved performance. Analogous equations to Eqs. 5.13 and 5.14 can be derived for different systems to understand the noise behavior and other effects (e.g., turbulence, scattering, aberration, dispersion, etc.) in the output spectrum to determine the best amplification strategy.
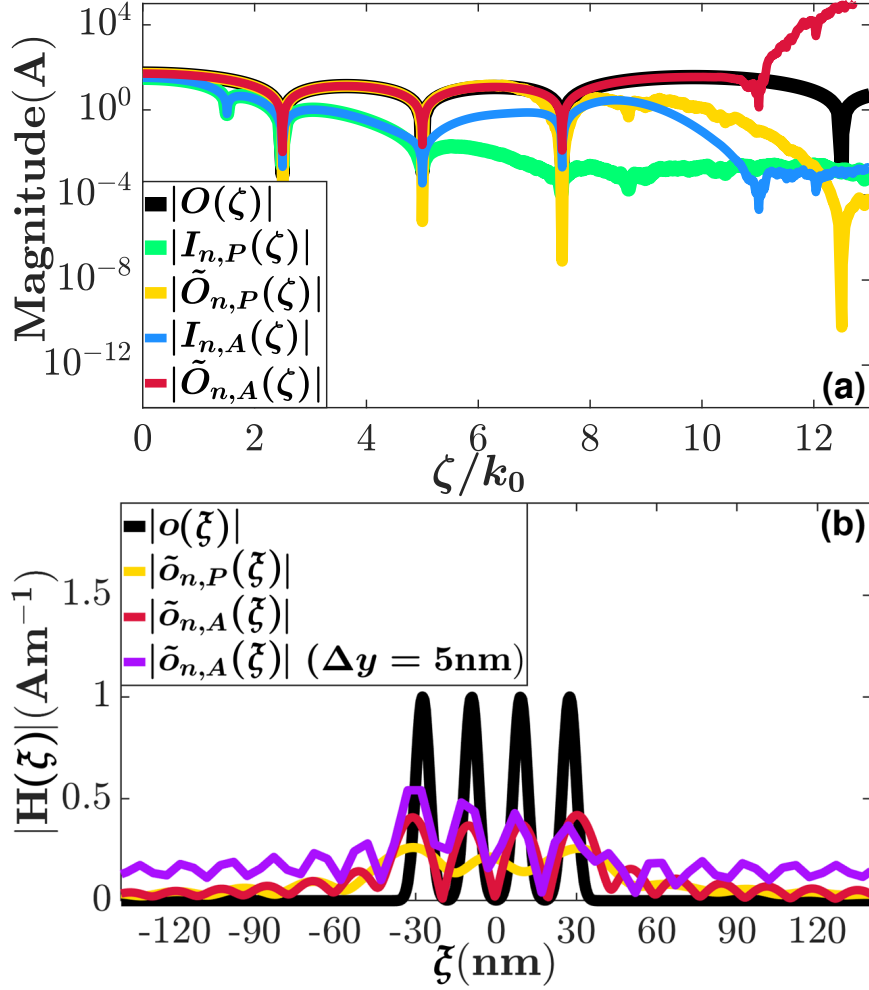
Figure 5.8: The comparison of the image reconstruction using ACI (without optimal Wiener filter) and the passive image reconstruction using the optimal Wiener filter, in (a) Fourier domain and (b) spatial domain. $\tilde{O}_{n,P}(\zeta)$ and $\tilde{O}_{n,A}(\zeta)$ refer to passive reconstructed image spectrum obtained by the optimal Wiener filter and the active reconstructed image spectrum obtained by the ACI without optimal Wiener filter. $\tilde{o}_{n,P}(\xi)$ and $\tilde{o}_{n,A}(\xi)$ are the respective reconstructed images in the spatial domain. The object (black) and the noisy images $\tilde{I}_{n,P}(\zeta)$ and $\tilde{I}_{n,A}(\zeta)$ before deconvolution are also indicated. Only magnitudes are shown. In (b) the discrete space ξ is interpolated to guide the eye. The ACI method clearly resolves the 4 objects (see black lines) separated by 18 nm peak-to-peak distance, using 2 overlapping Gaussian pass-bands with FWHMs of $2.3k_0$ and centered at $7k_0$ and $8.5k_0$. The constant amplitude amplification factor $A_0 = 630$.

References

[1] David Schurig, Jack J Mock, BJ Justice, Steven A Cummer, John B Pendry, Anthony F Starr, and David R Smith. Metamaterial electromagnetic cloak at microwave frequencies. *Science*, 314(5801):977–980, 2006.

[2] John Brian Pendry. Negative refraction makes a perfect lens. *Physical Review Letters*, 85(18):3966, 2000.

[3] Thomas Taubner, Dmitriy Korobkin, Yaroslav Urzhumov, Gennady Shvets, and Rainer Hillenbrand. Near-field microscopy through a *sic* superlens. *Science*, 313(5793):1595–1595, 2006.

[4] Zubin Jacob, Leonid V Alekseyev, and Evgenii Narimanov. Optical hyperlens: far-field imaging beyond the diffraction limit. *Optics Express*, 14(18):8247–8256, 2006.

[5] Ping Gao, Na Yao, Changtao Wang, Zeyu Zhao, Yunfei Luo, Yanqin Wang, Guohan Gao, Kaipeng Liu, Chengwei Zhao, and Xiangang Luo. Enhancing

aspect profile of half-pitch 32 nm and 22 nm lithography with plasmonic cavity lens. *Applied Physics Letters*, 106(9):093110, 2015.

[6] J Gwamuri, DÖ Güney, and JM Pearce. Advances in plasmonic light trapping in thin-film solar photovoltaic devices. *Solar Cell Nanotechnology*, pages 243–270, 2013.

[7] Ankit Vora, Jephias Gwamuri, Nezih Pala, Anand Kulkarni, Joshua M Pearce, and Durdu Ö Güney. Exchanging ohmic losses in metamaterial absorbers with useful optical absorption for photovoltaics. *Scientific Reports*, 4:4901, 2014.

[8] H Odabasi, FL Teixeira, and Durdu Ö Güney. Electrically small, complementary electric-field-coupled resonator antennas. *Journal of Applied physics*, 113(8):084903, 2013.

[9] Andres D Neira, Gregory A Wurtz, Pavel Ginzburg, and Anatoly V Zayats. Ultrafast all-optical modulation with hyperbolic metamaterial integrated in si photonic circuitry. *Optics Express*, 22(9):10987–10994, 2014.

[10] Amir Arbabi, Yu Horie, Mahmood Bagheri, and Andrei Faraon. Dielectric metasurfaces for complete control of phase and polarization with subwavelength spatial resolution and high transmission. *Nature Nanotechnology*, 10(11):937, 2015.

[11] Patrice Genevet, Federico Capasso, Francesco Aieta, Mohammadreza Khorasaninejad, and Robert Devlin. Recent advances in planar optics: from plasmonic to dielectric metasurfaces. *Optica*, 4(1):139–152, 2017.

[12] Costas M Soukoulis and Martin Wegener. Past achievements and future challenges in the development of three-dimensional photonic metamaterials. *Nature Photonics*, 5(9):523–530, 2011.

[13] S Anantha Ramakrishna and John B Pendry. Removal of absorption and increase in resolution in a near-field lens via optical gain. *Physical Review B*, 67(20):201101, 2003.

[14] MA Vincenti, D De Ceglia, V Rondinone, A Ladisa, A D'Orazio, MJ Bloemer, and M Scalora. Loss compensation in metal-dielectric structures in negative-refraction and super-resolving regimes. *Physical Review A*, 80(5):053807, 2009.

[15] Sebastian Wuestner, Andreas Pusch, Kosmas L Tsakmakidis, Joachim M Hamm, and Ortwin Hess. Overcoming losses with gain in a negative refractive index metamaterial. *Physical Review Letters*, 105(12):127401, 2010.

[16] Shumin Xiao, Vladimir P Drachev, Alexander V Kildishev, Xingjie Ni, Uday K Chettiar, Hsiao-Kuan Yuan, and Vladimir M Shalaev. Loss-free and active optical negative-index metamaterials. *Nature*, 466(7307):735–738, 2010.

[17] C M Soukoulis and M Wegener. Optical metamaterials—more bulky and less lossy. *Science*, 330(6011):1633–1634, 2010.

[18] Mark I Stockman. Criterion for negative refraction with low optical losses from a fundamental principle of causality. *Physical Review Letters*, 98(17):177404, 2007.

[19] Paul Kinsler and MW McCall. Causality-based criteria for a negative refractive index must be used with care. *Physical Review Letters*, 101(16):167401, 2008.

[20] Mehdi Sadatgol, Sahin K Ozdemir, Lan Yang, and Durdu Ö Güney. Plasmon injection to compensate and control losses in negative index metamaterials. *Physical Review Letters*, 115(3):035502, 2015.

[21] Huanan Li, Ahmed Mekawy, Alex Krasnok, and Andrea Alù. Virtual parity-time symmetry. *Physical Review Letters*, 124(19):193901, 2020.

[22] Anindya Ghoshroy, Şahin K. Özdemir, and Durdu Ö. Güney. Loss compensation in metamaterials and plasmonics with virtual gain. *Optical Materials Express*, to be published.

[23] Alex Krasnok and Andrea Alu. Active nanophotonics. *Proceedings of the IEEE*, 108(5):628–654, 2020.

[24] R. J. Jones and J. Ye. Femtosecond pulse amplification by coherent addition in a passive optical cavity. *Optics Letters*, 27:1848, 2002.

[25] Eric O. Potma, Conor Evans, X. Sunney Xie, R. Jason Jones, and Jun Ye. Picosecond-pulse amplification with an external passive optical cavity. *Optics Letters*, 28:1835, 2003.

[26] Anindya Ghoshroy, Wyatt Adams, Xu Zhang, and Durdu Ö Güney. Active plasmon injection scheme for subdiffraction imaging with imperfect negative index flat lens. *Journal of Optical Society of America B*, 34(7):1478–1488, 2017.

[27] Anindya Ghoshroy, Wyatt Adams, Xu Zhang, and Durdu Ö Güney. Hyperbolic metamaterial as a tunable near-field spatial filter to implement active plasmon-injection loss compensation. *Physical Review Applied*, 10(2):024018, 2018.

[28] Anindya Ghoshroy, Wyatt Adams, Xu Zhang, and Durdu Ö Güney. Enhanced superlens imaging with loss-compensating hyperbolic near-field spatial filter. *Optics Letters*, 43(8):1810–1813, 2018.

[29] Michael C Roggemann, David W Tyler, and Marsha F Bilmont. Linear reconstruction of compensated images: theory and experimental results. *Applied Optics*, 31(35):7429–7441, 1992.

[30] Jan Biemond, Reginald L Lagendijk, and Russell M Mersereau. Iterative methods for image deblurring. *Proceedings of the IEEE*, 78(5):856–883, 1990.

[31] Anthony Zaknich. *Principles of adaptive filters and self-learning systems.* Springer Science & Business Media, 2005.

[32] Wyatt Adams, Mehdi Sadatgol, Xu Zhang, and Durdu Ö Güney. Bringing the 'perfect lens' into focus by near-perfect compensation of losses without gain media. *New Journal of Physics*, 18(12):125004, dec 2016.

[33] Wyatt Adams, Anindya Ghoshroy, and Durdu Ö Güney. Plasmonic superlens image reconstruction using intensity data and equivalence to structured light illumination for compensation of losses. *Journal of Optical Society of America B*, 34(10):2161–2168, 2017.

[34] Xu Zhang, Wyatt Adams, Mehdi Sadatgol, and Durdu Ö Güney. Enhancing the resolution of hyperlens by the compensation of losses without gain media. *Progress In Electromagnetics Research C*, 70:1–7, 2016.

[35] Xu Zhang, Wyatt Adams, and Durdu Ö Güney. Analytical description of inverse filter emulating the plasmon injection loss compensation scheme and implementation for ultrahigh-resolution hyperlens. *Journal of Optical Society of America B*, 34(6):1310–1318, 2017.

[36] Xiao-Feng Qian, A Nick Vamivakas, and Joseph H Eberly. Emerging connections: classical and quantum optics. *Optics and Photonics News*, 28(10):34–41, 2017.

[37] David Schurig and David R Smith. Spatial filtering using media with indefinite permittivity and permeability tensors. *Applied Physics Letters*, 82(14):2215–2217, 2003.

[38] Carlo Rizza, Alessandro Ciattoni, Elisa Spinozzi, and Lorenzo Columbo. Terahertz active spatial filtering through optically tunable hyperbolic metamaterials. *Optics Letters*, 37(16):3345–3347, 2012.

[39] Ling Liu, Ping Gao, Kaipeng Liu, Weijie Kong, Zeyu Zhao, Mingbo Pu, Chang-tao Wang, and Xiangang Luo. Nanofocusing of circularly polarized bessel-type plasmon polaritons with hyperbolic metamaterials. *Materials Horizons*, 4(2):290–296, 2017.

[40] Gaofeng Liang, Xi Chen, Qing Zhao, and L Jay Guo. Achieving pattern uniformity in plasmonic lithography by spatial frequency selection. *Nanophotonics*, 7(1):277–286, 2018.

[41] Marcin Kieliszczyk, Bartosz Janaszek, Anna Tyszka-Zawadzka, and Paweł Szczepański. Tunable spectral and spatial filters for the mid-infrared based on hyperbolic metamaterials. *Applied Optics*, 57(5):1182–1187, 2018.

[42] Wyatt Adams, Anindya Ghoshroy, and Durdu O Guney. Plasmonic superlens imaging enhanced by incoherent active convolved illumination. *ACS Photonics*, 5(4):1294–1302, 2018.

[43] Alexander K Popov and Vladimir M Shalaev. Compensating losses in negative-index metamaterials by optical parametric amplification. *Optics Letters*, 31(14):2169–2171, 2006.

[44] Durdu Ö Güney, Thomas Koschny, and Costas M Soukoulis. Reducing ohmic losses in metamaterials by geometric tailoring. *Physical Review B*, 80(12):125129, 2009.

[45] Wyatt Adams. *Enhancing the Resolution of Imaging Systems by Spatial Spectrum Manipulation.* PhD thesis, Michigan Technological University, 2019.

[46] Mohamed E Hanafy, Michael C Roggemann, and Durdu Ö Güney. Detailed effects of scattering and absorption by haze and aerosols in the atmosphere on the average point spread function of an imaging system. *Journal of Optical Society of America A*, 31(6):1312–1319, 2014.

[47] Mohamed E Hanafy, Michael C Roggemann, and Durdu Ö Güney. Estimating the image spectrum signal-to-noise ratio for imaging through scattering media. *Optical Engineering*, 54(1):013102, 2015.

[48] Mohamed E Hanafy, Michael C Roggemann, and Durdu Ö Güney. Reconstruction of images degraded by aerosol scattering and measurement noise. *Optical Engineering*, 54(3):033101, 2015.

[49] Durdu Ö Güney, Wyatt Adams, and Anindya Ghoshroy. Super-resolution enhancement with active convolved illumination and correlations. In *Active Photonic Platforms XI*, volume 11081, page 1108128. International Society for Optics and Photonics, 2019.

[50] Hichem Guerboukha, Kathirvel Nallappan, and Maksim Skorobogatiy. Toward real-time terahertz imaging. *Advances in Optics and Photonics*, 10(4):843–938, 2018.

[51] Kiarash Ahi. A method and system for enhancing the resolution of terahertz imaging. *Measurement*, 138:614–619, 2019.

[52] Greg Gbur and Emil Wolf. Spreading of partially coherent beams in random media. *Journal of Optical Society of America A*, 19(8):1592–1598, 2002.

[53] Aristide Dogariu and Stefan Amarande. Propagation of partially coherent beams: turbulence-induced degradation. *Optics Letters*, 28(1):10–12, 2003.

[54] Greg Gbur. Partially coherent beam propagation in atmospheric turbulence. *Journal of Optical Society of America A*, 31(9):2038–2045, 2014.

[55] Milo W Hyde. Controlling the spatial coherence of an optical source using a spatial filter. *Applied Sciences*, 8(9):1465, 2018.

[56] Francesco Monticone, Constantinos A Valagiannopoulos, and Andrea Alù. Parity-time symmetric nonlocal metasurfaces: all-angle negative refraction and volumetric imaging. *Physical Review X*, 6(4):041018, 2016.

[57] Ramy El-Ganainy, Mercedeh Khajavikhan, Demetrios N Christodoulides, and Sahin K Ozdemir. The dawn of non-hermitian optics. *Communications Physics*, 2(1):1–5, 2019.

[58] Amor Gueddana, Peyman Gholami, and Vasudevan Lakshminarayanan. Can a universal quantum cloner be used to design an experimentally feasible near-deterministic cnot gate? *Quantum Information Processing*, 18(7):221, 2019.

[59] Amor Gueddana and Vasudevan Lakshminarayanan. Toward the universal quantum cloner limit for designing compact photonic cnot gate. *arXiv:1906.06547*, 2019.

[60] Nicholas Fang, Hyesog Lee, Cheng Sun, and Xiang Zhang. Sub–diffraction-limited optical imaging with a silver superlens. *Science*, 308(5721):534–537, 2005.

[61] FYHK Zenhausern, Y Martin, and HK Wickramasinghe. Scanning interferometric apertureless microscopy: optical imaging at 10 angstrom resolution. *Science*, 269(5227):1083–1085, 1995.

[62] John J. Heine and Madhusmita Behera. Aspects of signal-dependent noise characterization. *Journal of Optical Society of America A*, 23(4):806–815, 2006.

[63] John F Walkup and Robert C Choens. Image processing in signal-dependent noise. *Optical Engineering*, 13(3):133258, 1974.

[64] Rangachar Kasturi, John F. Walkup, and Thomas F. Krile. Image restoration by transformation of signal-dependent noise to signal-independent noise. *Applied Optics*, 22(22):3537–3542, 1983.

[65] Gary K Froehlich, John F Walkup, and Thomas F Krile. Estimation in signal-dependent film-grain noise. *Applied Optics*, 20(20):3619–3626, 1981.

[66] S Ibrahim Sadhar and AN Rajagopalan. Image estimation in film-grain noise. *IEEE Signal Processing Letters*, 12(3):238–241, 2005.

[67] David Voelz. *Computational fourier optics: a MATLAB tutorial.* SPIE press, 2011.

[68] EA Ingerman, RA London, Rainer Heintzmann, and MGL Gustafsson. Signal, noise and resolution in linear and nonlinear structured-illumination microscopy. *Journal of Microscopy*, 273(1):3–25, 2019.

[69] Jan Becker, Ronny Förster, and Rainer Heintzmann. Better than a lens-a novel concept to break the snr-limit, given by fermat's principle. *arXiv:1811.08267*, 2018.

[70] Robert L Lucke. Fourier-space properties of photon-limited noise in focal plane array data, calculated with the discrete fourier transform. *Journal of Optical Society of America A*, 18(4):777–790, 2001.

[71] G Agranov, R Mauritzson, S Barna, J Jiang, A Dokoutchaev, X Fan, and X Li. Super small, sub 2 μm pixels for novel cmos image sensors. In *Extended Programme of the 2007 International Image Sensor Workshop*, pages 307–310, 2007.

[72] M Bigas, Enric Cabruja, Josep Forest, and Joaquim Salvi. Review of cmos image sensors. *Microelectronics Journal*, 37(5):433–451, 2006.

[73] Igor Shcherback and Orly Yadid-Pecht. Photoresponse analysis and pixel shape optimization for cmos active pixel sensors. *IEEE Transactions on Electron Devices*, 50(1):12–18, 2003.

[74] Oleg Mitrofanov, Mark Lee, Julia WP Hsu, Igal Brener, Roey Harel, John F Federici, James D Wynn, Loren N Pfeiffer, and Ken W West. Collection-mode near-field imaging with 0.5-thz pulses. *IEEE Journal of Selected Topics in Quantum Electronics*, 7(4):600–607, 2001.

[75] Nicholas Fang, Zhaowei Liu, Ta-Jen Yen, and Xiang Zhang. Regenerating evanescent waves from a silver superlens. *Optics Express*, 11(7):682–687, 2003.

[76] Aleksandar D Rakić, Aleksandra B Djurišić, Jovan M Elazar, and Marian L Majewski. Optical properties of metallic films for vertical-cavity optoelectronic devices. *Applied Optics*, 37(22):5271–5283, 1998.

[77] Zhaowei Liu, Hyesog Lee, Yi Xiong, Cheng Sun, and Xiang Zhang. Far-field optical hyperlens magnifying sub-diffraction-limited objects. *Science*, 315(5819):1686–1686, 2007.

[78] Hermann A Haus. *Electromagnetic noise and quantum optical measurements.* Springer Science & Business Media, 2012.

[79] Makoto Akiba, Kenji Tsujino, and Masahide Sasaki. Ultrahigh-sensitivity single-photon detection with linear-mode silicon avalanche photodiode. *Optics Letters*, 35(15):2621–2623, 2010.

[80] Zhaowei Liu. Electrical and Computer Engineering Department, University of California at San Diego, La Jolla, Calif. 92093 (personal communication, 2020).

[81] Anna Bezryadina, Junxiang Zhao, Yang Xia, Xiang Zhang, and Zhaowei Liu. High spatiotemporal resolution imaging with localized plasmonic structured illumination microscopy. *ACS Nano*, 12(8):8248–8254, 2018.

[82] Yi Xiong, Zhaowei Liu, Cheng Sun, and Xiang Zhang. Two-dimensional imaging by far-field superlens at visible wavelengths. *Nano Letters*, 7(11):3360–3365, 2007.

[83] Sudhakar Prasad. Implications of light amplification for astronomical imaging. *Journal of Optical Society of America A*, 11(11):2799–2803, 1994.

[84] A Demetriadou and JB Pendry. Taming spatial dispersion in wire metamaterial. *Journal of Physics: Condensed Matter*, 20(29):295222, 2008.

[85] Miguel Molerón and Chiara Daraio. Acoustic metamaterial for subwavelength edge detection. *Nature Communications*, 6(1):1–6, 2015.

[86] Henri Benisty and François Goudail. Dark-field hyperlens exploiting a planar fan of tips. *Journal of the Optical Society of America B*, 29(9):2595–2602, 2012.

[87] Taavi Repän, Andrei V Lavrinenko, and Sergei V Zhukovsky. Dark-field hyperlens: Super-resolution imaging of weakly scattering objects. *Optics Express*, 23(19):25350–25364, 2015.

[88] Lian Shen, Huaping Wang, Rujiang Li, Zhiwei Xu, and Hongsheng Chen.

Hyperbolic-polaritons-enabled dark-field lens for sensitive detection. *Scientific Reports*, 7(1):1–8, 2017.

[89] Rajagopal Vadivambal and Digvir S Jayas. *Bio-imaging: principles, techniques, and applications.* CRC Press, 2015.

[90] Hongda Wang, Yair Rivenson, Yiyin Jin, Zhensong Wei, Ronald Gao, Harun Günaydın, Laurent A Bentolila, Comert Kural, and Aydogan Ozcan. Deep learning enables cross-modality super-resolution in fluorescence microscopy. *Nature Methods*, 16(1):103–110, 2019.

[91] Jean Paul Guillet, Benoît Recur, Louis Frederique, Bruno Bousquet, Lionel Canioni, Inka Manek-Hönninger, Pascal Desbarats, and Patrick Mounaix. Review of terahertz tomography techniques. *Journal of Infrared, Millimeter, and Terahertz Waves*, 35(4):382–411, 2014.

Chapter 6

Superresolution enhancement with active convolved illumination and correlations[1]

6.1 Introduction

Recently Sadatgol et al. proposed an alternative solution to manage the losses in metamaterials named "plasmon injection (PI or Π) scheme" [1]. The process modifies the field incident on a lossy metamaterial with an auxiliary source. This source amplifies an arbitrary field thereby enhancing transmission through the lossy metamaterial. Since amplification is achieved by a coherent superposition of the original incident field with the auxiliary source, the process is fundamentally different from conventional optical gain medium. This avoids typical problems associated with gain medium such as stability, gain saturation [2, 3] and noise generation due to amplified spontaneous emission [4]. The Π scheme was theoretically implemented with near-field imaging systems employing negative index materials [5], superlenses [6], and hyperlenses [7, 8] to show significant performance improvements. These implementations were shown to emulate linear deconvolution [5]. Later studies investigated the advantages of generating the auxiliary source through a convolution process with the original field to selectively amplify a controllable band of spatial frequencies [9]. The auxiliary source which is now correlated [9, 10] with the original object field was shown to be substantially resistant to noise amplification when implemented with coherent [11] and incoherent [12] illumination. The introduction of correlations [13] into the auxiliary source marked a significant milestone towards the development of

an effective alternative to previously conceived loss mitigation approaches. This moti-vated a generalization of the earlier variants of the Π scheme to a more encompassing active convolved illumination (ACI) [12] since the physical convolution operation is the cornerstone of the process and is not specific to plasmons.

In this study we review the ACI and present potential implementations with different imaging systems with the goal of pushing their resolutions beyond existing limits. We also discuss a possible extension of the ACI theory to quantum computing. This work is motivated by a recently developed theoretical framework which provides extensive mathematical analysis of the fundamental concept of ACI for coherent illumination [14]. Particular emphasis was directed at the required mechanisms, such as selective amplification and physical convolution to accentuate their role in enabling recovery of attenuated spatial frequencies with minimal noise amplification with ACI. We briefly summarize the framework presented in [14] in a more general perspective to facilitate the development of subsequent discussions.

6.2   Brief review of the theory of ACI

Figure 6.1 shows a generalized schematic of a system which attempts to extract useful information from an object. A source of light $E_{in}(\vec{k})$ with wavevector $\vec{k}$ acts as the carrier and interacts with an object resulting in the spectrum $O(\vec{k})$. This propagates
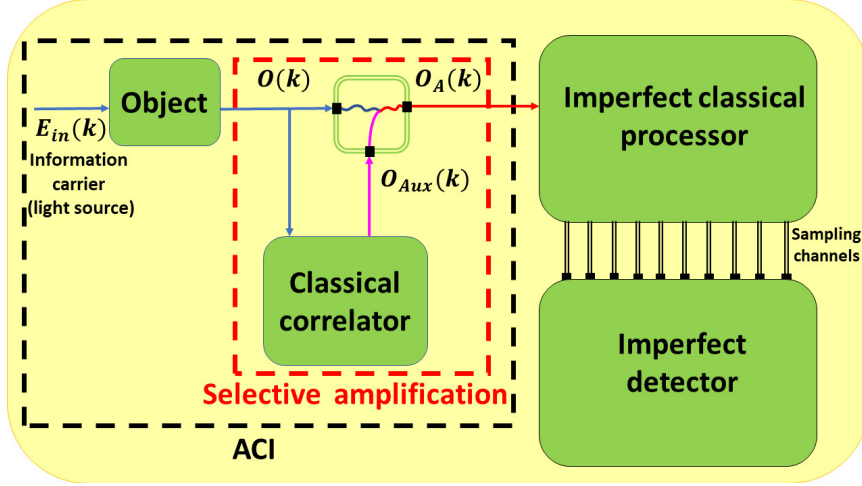
Figure 6.1: A generalized schematic of an imperfect information transmission and collection system with the inclusion of ACI.

through an imperfect classical processor such as standard optical or metamaterial lenses, fibers, aerosol laden or random media and is collected by a detector before being converted into meaningful data. However, during the propagation process, $O(\vec{k})$ is distorted by attenuation or partial decorrelation. Material losses, diffraction, scattering or random fluctuations in material or structural properties within the classical processor are few of the contributing factors. The propagation step is described with a point spread function (PSF) and $I(\vec{k}) = O(\vec{k})T(\vec{k})$ is the signal reaching the detector, where $T(\vec{k})$ is the Fourier transform of the PSF. Additionally, the imperfect detector which samples the information incorporates further noise into the measured signal. Let us assume that the information is measured as a periodic sequence of $M \times M$ spatial samples along the yz plane. The resulting noisy signal is described

with the signal modulated noise model as

$$i_n(\xi_y, \xi_z) = i(\xi_y, \xi_z) + f\{i(\xi_y, \xi_z)\}^\gamma n_{sd} + n_{si}, \qquad (6.1)$$

where ξ_y and ξ_z are the sample points along the y and z axis and n_{sd} and n_{si} are random variables with standard deviations σ_1 and σ_2, respectively. $i(\xi_y, \xi_z)$ and $i_n(\xi_y, \xi_z)$ are the ideal and noisy versions of the image and $i(\xi_y, \xi_z) = o(\xi_y, \xi_z) * PSF(\xi_y, \xi_z)$. The second and third terms in Eq. 6.1 are the signal-dependent and independent noise processes and with $0 < \gamma < 1$. The overall variance of noise in the Fourier domain is [14]

$$\sigma^2_{\zeta_{k_y}, \zeta_{k_z}} = \frac{1}{M^2} \sum_{\zeta_{k_y}} \sum_{\zeta_{k_z}} |I(\zeta_{k_y}, \zeta_{k_z})|^2 \sigma_1^2 + \sigma_2^2. \qquad (6.2)$$

Implementation of ACI involves modifying the illumination fed into the classical processor as shown by the dashed black box in figure 6.1. A classical correlator taps into $O(\vec{k})$ and selectively amplifies the portion of the spectrum which is most vulnerable to distortion. This selectively amplified spectrum $O_{Aux}(\vec{k})$, referred to as auxiliary source is superimposed with $O(\vec{k})$ resulting in $O_A(\vec{k})$ and is fed into the classical processor. The spectrum measured at the detector without and with the selective amplification block is

$$I_P(\zeta_{k_y}, \zeta_{k_z}) = O(\zeta_{k_y}, \zeta_{k_z})T(\zeta_{k_y}, \zeta_{k_z}), \qquad (6.3a)$$

$$I_A(\zeta_{k_y}, \zeta_{k_z}) = O(\zeta_{k_y}, \zeta_{k_z})T(\zeta_{k_y}, \zeta_{k_z})[1 + A_0 G(\zeta_{k_y}, \zeta_{k_z})], \qquad (6.3b)$$

respectively where $T(\zeta_{k_y}, \zeta_{k_z}) = \mathcal{F}\{PSF(\xi_y, \xi_z)\}$ is the transfer function describing the transmission of ζ_{k_y} and ζ_{k_z} spectral components through the classical processor. The second term in Eq. 6.3b is the residual auxiliary source where A_0 is the amplification provided and $G(\zeta_{k_y}, \zeta_{k_z})$ is a band-limited function identifying the selectively amplified the portion of the spectrum. The variance of noise for $I_P(\zeta_{k_y}, \zeta_{k_z})$ and $I_A(\zeta_{k_y}, \zeta_{k_z})$ are denoted by $\sigma^2_{\zeta_{k_y}, \zeta_{k_z}, P}$ and $\sigma^2_{\zeta_{k_y}, \zeta_{k_z}, A}$ respectively, and the latter can be written as [14] $\sigma^2_{\zeta_{k_y}, \zeta_{k_z}, A} = \sigma^2_{\zeta_{k_y}, \zeta_{k_z}, P} + \sigma^2_{\zeta_{k_y}, \zeta_{k_z}, Aux}$ according to Eq. 6.2 where the second term is the additional noise contribution from the residual auxiliary source in Eq. 6.3b. It was shown [14] how the selective amplification block (see figure 6.1) can contribute towards the adequate amplification in the signal while minimizing $\sigma^2_{\zeta_{k_y}, \zeta_{k_z}, Aux}$. In general, ACI can be implemented with temporal or spatial frequencies and the placement of the selective amplification block (see figure 6.1) is configurable and can be before the object block as well. However, the current variant of ACI restricts placement of the selective amplification block before the imperfect processor stage.

6.3   Implementations of ACI

In this work, we discuss some of the potential implementations and extensions of ACI with three separate systems. We provide a brief description of each system to emphasize the commonalities with figure 6.1 followed by proposing potential methods of including the selective amplification block into the system. The factors which limit

the performance of each system is briefly discussed followed by an argument on how it can be extended with ACI.

6.3.1 Imaging through scattering and random media

We propose an implementation of ACI for imaging through scattering and random media. This topic is of considerable theoretical and practical importance particularly in free-space optical communications, imaging and targeting systems where the origins of turbulence and scattering may be terrestrial, atmospheric and ionospheric (e.g., plasma) [15, 16, 17]. In the subsequent discussion, an imaging process involving wave propagation through an aerosol laden atmosphere is adopted. The presence of various molecular species and aerosols in a turbulent medium results in attenuation and blurring of the propagating electromagnetic wave. Attenuation is attributed primarily to absorption and Rayleigh scattering. Stochastic variations in the propagation path due to turbulence and Mie scattering results in photons being intercepted by adjacent pixels and produces a blurred image [18, 19].

The schematic in figure 6.2 shows a generalized atmospheric imaging scenario. A perfect Lambertian surface along the yz plane has a spectral degree of reflectance $\rho(y, z)$ and is defined as the target. It is illuminated by a monochromatic source of wavelength λ with an intensity distribution $E_0(y, z)$. Light from the source is assumed

to propagate though the atmosphere before hitting the target. Therefore, object has an intensity distribution $o(y, z) = E(y, z)\rho(y, z)$ where $E(y, z) = E_0(y, z)e^{-\tau_{atm}(\lambda)}$ and $\tau_{atm}(\lambda)$ is the atmospheric optical depth. $o(y, z)$ propagates a distance d through the aerosol laden atmosphere before being intercepted by a standard imaging system with focal length f and an entrance aperture of area A. The radial PSF of the camera system shown in figure 6.2 is a diffraction-limited Airy disc pattern denoted by $PSF_{Airy}(r)$ described by a Bessel function of the first kind and order 1. The effect of atmospheric aerosols broadens $PSF_{Airy}(r)$ and the radial distribution of the effective PSF (denoted by $PSF_{eff}(r)$) is

$$PSF_{eff}(r) = e^{-\tau_{atm}(\lambda)}PSF_{Airy}(r) + PSF_{sca}(r) , \qquad (6.4)$$

where $PSF_{sca}(r)$ is the radial intensity distribution of the scattered radiation[17, 20, 21, 22, 23, 24]. The convolution between $o(y, z)$ and $PSF_{eff}(r)$ is the resulting image which is recorded by the detector. The first term in Eq. 6.4 is essentially an attenuated Airy disk pattern (unscattered light) superimposed with the scattered intensity distribution. Therefore, the convolution between $o(y, z)$ and the second term in Eq. 6.4 is the scattered intensity which is temporally and spatially uncorrelated from the input field and results in a blurred halo on the image plane. In addition to the aerosol-induced blurring, the statistical nature of photon detection also adds shot noise with Poissonian statistics. Therefore, the noisy intensity distribution of
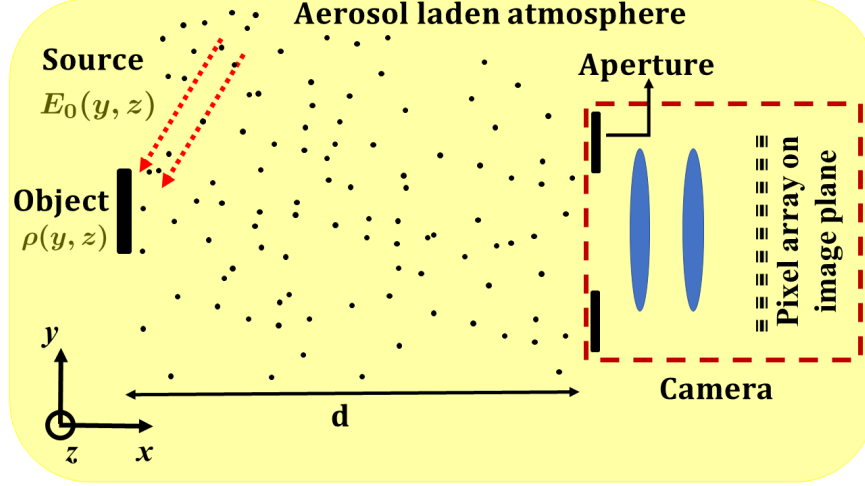
Figure 6.2: Atmospheric imaging schematic.

the image is written by modifying Eq. 6.1 as

$$i_n(r) = e^{-\tau_{atm}(\lambda)} i(r) + f\{i_{eff}(r)\}^{\gamma} n_{sd} + n_{si}, \qquad (6.5)$$

where $i(r)$ and $i_{eff}(r)$ are the convolutions of $o(r)$ with $PSF_{Airy}(r)$ and $PSF_{eff}(r)$, respectively in Eq. 6.4 and $o(r)$ is the radial distribution of the object intensity.

The effects of scattering and absorption from aerosols are included into $PSF_{eff}(r)$ in Eq. 6.4 by applying a discretized scattering theory where particles are assumed to be sparse (compared to the wavelength) in the propagation medium [22]. The optical properties of the propagation medium are described with the volume absorption k_{abs}, scattering k_{sca}, and extinction k_{ext} coefficients related by $k_{ext} = k_{sca} + k_{abs}$. For a polydisperse collection of particles (such as an aerosol laden atmosphere) , k_{ext} is

191

written as

$$k_{ext}(\lambda) = \int_0^\infty \pi\alpha^2[Q_{sca}(\alpha, \lambda) + Q_{abs}(\alpha, \lambda)]n(\alpha)d\alpha, \tag{6.6}$$

where Q_{sca}, Q_{abs} scattering and absorption efficiency factors (related to the extinction efficiency factor as $Q_{ext} = Q_{sca} + Q_{abs}$) and $n(\alpha)$ in the particle size distribution function with radius α. $n(\alpha)$ which can be a multimodal lognormal or modified Gamma distribution depending on the type of aerosol [22].

ACI is implemented into the system by incorporating the selective amplification block (see dashed red box in figure 6.1). Note that the atmospheric propagation from the object to the camera in figure 6.2 is the analogue of the imperfect classical processor stage in figure 6.1. The placement of the selective amplification block requires some consideration. Typical propagation distances through the atmosphere are quite large and can be in the order of kilometers. Therefore, selective amplification block cannot be placed after the object. However, according to Eq. 6.3b, we require an active object spectrum with the form $O_A(k_y, k_z) = O(k_y, k_z) + A_0 G(k_y, k_z)O(k_y, k_z)$ which in the spatial domain can be written as $o_A(y, z) = o(y, z) + o_{Aux}(y, z)$. The second term is the spatial distribution of the auxiliary source which can be written as $E_S(y, z)\rho(y, z)$ where $E_S(y, z)$ is a structured illumination pattern. Therefore, ACI can be implemented by moving the selective amplification block over to the illumination side. The modified illumination incident on the object is written as

$$E_A(y, z) = E(y, z) + E_S(y, z) \tag{6.7}$$

where $E_S(y, z)$ interacts with $\rho(y, z)$ to generate the auxiliary source $A_0 G(k_y, k_z) O(k_y, k_z)$. As an example, the functional form of the required intensity distribution can be written as

$$E_S(y, z)\rho(y, z) = \mathcal{F}^{-1}\{A_0 G(k_y, k_z)[\rho(k_y, k_z) * E(k_y, k_z)]\}, \qquad (6.8)$$

for a specific object where $\rho(k_y, k_z) = \mathcal{F}\{\rho(y, z)\}$. Eq. 6.7 can be readily solved for $\rho(y, z) \neq 0$ to determine the resulting $E_S(y, z)$. However, this would make the process dependent on the object which is undesirable. Therefore, the next challenge would require formulating a general form of the structured field $E_S(y, z)$ which can generate $o_{Aux}(y, z)$ with no prior knowledge of $\rho(y, z)$. Additionally, effect of the scattering medium should be considered during the design of $E_S(y, z)$. According to Eq. 6.5, the overall noise at each radial position on the image plane is dependent on the $i_{eff}(r)$. Since $i_{eff}(r)$ is the total intensity containing a contribution from the scattered field, the auxiliary source will also have a finite contribution to the overall noise similar to Eq. 6.2 and the framework developed in [14]. The additional noise can be described by the convolution between $PSF_{sca}(r)$ in Eq. 6.4 and $O_{Aux}(y, z)$. Therefore, the design process of $E_S(y, z)$ should respect Eq. 6.8 and in order to ensure that the resulting amplification in scattered field is minimized.

6.3.2   THz time domain spectroscopy

Imaging and spectroscopy with THz radiation [25] is a rapidly evolving multidisciplinary field with various practical applications a few of which are industrial environments [26], pharmaceutical [27] and biomedical [28], agriculture and food industry [29], defense and security [30], art conservation [31], material characterization [32] and holography [33]. THz radiation is capable of penetrating most dielectric materials and can probe interior structures with meaningful contrast. The non-ionizing nature of THz light offers unique opportunities of non-destructive imaging [34]. THz time domain spectroscopy (THz-TDS) which is high resolution imaging technique has seen rapid development since its inception. THz-TDS is particularly useful in non-invasive identification of spectral fingerprints of different bio-molecular species [35] many of which have absorption bandwidths for vapour rotational [36] or vibrational modes [37] in the THz domain. However, the maximum spectral resolution of the spectroscopic measurement is limited by noise from three sources [36]. Noise is contributed from the emitting antenna, which manifests itself as random temporal fluctuations in the pulse intensity and is transmitted from the emitter to the detector. The remaining two sources of noise are shot noise and Johnson—Nyquist (electronic) noise. While shot noise imposes a fundamental limit on the maximum resolvable spatial and temporal frequency especially in transmission mode THz-TDS, noise from the source can result in artifacts and obscure the measured spectroscopic data[38] especially for

complex targets with finer structural and spectroscopic signatures. Therefore, an implementation of ACI with THz imaging systems would serve to improve the accuracy in measurement and extend the fundamental noise-limited resolution limit.
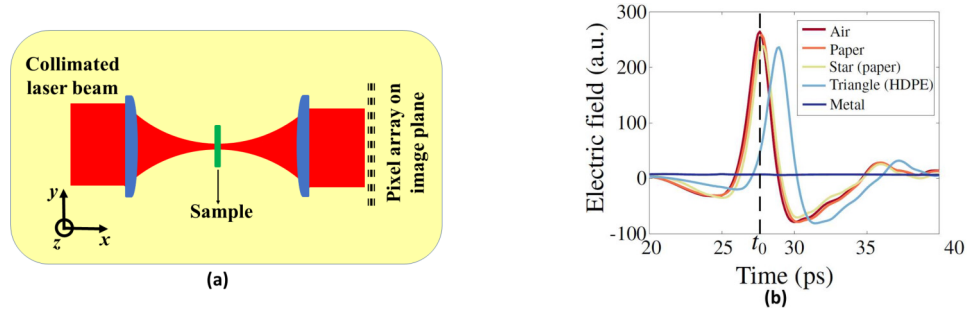

Figure 6.3: (a) General schematic of a THz-TDS setup in transmission mode and (b) trace of the electric field extracted from different positions across an example sample. (a) Adapted and (b) reprinted with permission from [34] ©The Optical Society.

In the subsequent discussion we consider a classic THz-TDS setup in transmission mode and analyze potential ways of implementing ACI. A generalized schematic of the setup is shown in the schematic in figure 6.3(a). A collimated laser pulse is focused on a sample of thickness L and the response is collected on the image plane as a function of time. The sample or the source is mechanically or optically steered to obtain a 2d scan along the yz plane. A reference pulse is propagated with the same configuration without the sample and both measurements are Fourier transformed into the temporal frequency domain. Figure 6.3(b) shows a plot of a reference plot (red line) and other time domain plots of the same pulse after propagation through an example sample. The amplitude and phase of the two spectra are then analyzed

to obtain useful information about the optical properties of the sample. The overall variance of noise in the temporal frequency domain is [36]

$$\sigma^2_{\xi_y, \xi_z, \omega} = T^2(\omega)\sigma^2_E(\omega) + \sigma^2_{shot}(\omega) + \sigma^2_{elec}(\omega) \,, \tag{6.9}$$

were $\sigma^2_{shot}(\omega)$ and $\sigma^2_{elec}(\omega)$ are the variances of the shot and electronic noise, respectively and are the temporal frequency analogues of the second and third terms on the RHS of Eq. 6.1. $T^2(\omega)\sigma^2_E(\omega)$ is the variance of the source noise and $T(\omega)$ is the transfer function of the system.

One possible implementation of ACI for THz-TDS imaging systems in the temporal frequency domain by modifying the source spectrum as

$$E_{A,i}(\omega) = E_{0,i}(\omega) + A_0 G(\omega) \,, \tag{6.10}$$

where $E_{0,i}(\omega)$ is the original pulse, which is superimposed [39] with a band-limited secondary pulse $G(\omega)$. The spectral components of $G(\omega)$ are selectively amplified by a factor A_0. The interaction of the second term with the sample shown in figure 6.3 generates the auxiliary source. For example, consider an example target with a spatially varying refractive index $\tilde{n} = n - i\kappa$. For simplicity, let us assume the THz beam is a plane wave normally incident on the target with spectral components given

by Eq. 6.10. The THz beam transmitted through the sample is [40, 41]

$$E_{A,t}(\omega) = E_{A,i}(\omega)\tau(\tilde{n}, \omega)P(\tilde{n}, \omega, L)\sum_{p=0}^{\infty}[r(\tilde{n}, \omega)P^2(\tilde{n}, \omega, L)]^p \qquad (6.11)$$

where $\tau(\tilde{n}, \omega)$ and $r(\tilde{n}, \omega)$ are the squares of the transmission and reflection coefficients of the sample, respectively. $P(\tilde{n}, \omega, L)$ is a coefficient of propagation through the sample and the summation term accounts for backward and forward reflections similar to the Fabry-Perot effect. Each term of the summation in Eq. 6.11 corresponds to a temporal echo and directly transmitted beam is indicated by $p = 0$. The summation term has been included since the secondary pulse (second term in Eq. 6.10) has a longer temporal duration. Therefore, the corresponding temporal echoes may not be sufficiently separated to allow time windowing. Note that by substituting $E_{A,i}(\omega)$ from Eq. 6.10 into Eq. 6.11, we can obtain an equation of the active image analogous to Eq. 6.3b. Another potential method of implementing ACI can involve structuring the spatial field distribution of the THz source itself similar to the atmospheric imaging implementation. This would permit selective amplification of the higher-spatial frequency features of the target. For example, $G(\omega)$ in Eq. 6.10 can be replaced with $G(y, z; \omega)$ which represents a structured illumination at the frequency ω. In a THz source, such as semiconductor-based dipole antennas operated with femtosecond laser pulses [42], each $E_{0,i}(\omega)$ in Eq. 6.10 has an illumination profile which can be approximated with a Gaussian illumination distribution [42, 43] such as a TEM_{00} mode. Therefore, the THz pulse, shown in figure 6.3(b) can be thought

of as a superposition of multiple Gaussian beams with frequencies ranging form a few 100 GHz to several THz. The spatial structuring of the THz pulse can be done by superimposing $E_{0,i}(\omega)$ in Eq. 6.10 with a secondary beam where a controlled number of temporal frequencies have higher order modes. Since higher spatial frequency features of the target typically have lower transmission [34], and are more susceptible to distortion from shot noise especially in transmission mode THz-TDS. Implementing ACI with the THz pulse in both temporal and spatial domains according to the proposed methods may not only improve measurement accuracy but also potentially extend system operation beyond existing limits. The above implementations of ACI can be incorporated in the recently proposed analytical model of the THz imaging equation [44].

6.3.3   Quantum computing

The working principle of the ACI in the classical picture is recapped in figure 6.4 (left panel) to relate with quantum computing. In the classical picture, the input $O_{in}(\vec{k})$ is first copied to obtain two identical copies, then one of the copies is modified to create an auxiliary input $O_{cr}(\vec{k})$ correlated with the other copy. The both are then sent to imperfect classical processor giving an output $O_{out}(\vec{k})$ with higher fidelity than the otherwise possible with no correlations. In the context of imaging [1, 5, 10, 11, 12], $O_{in}(\vec{k})$, $O_{cr}(\vec{k})$, and $O_{out}(\vec{k})$ correspond to the object, auxiliary source, and the image
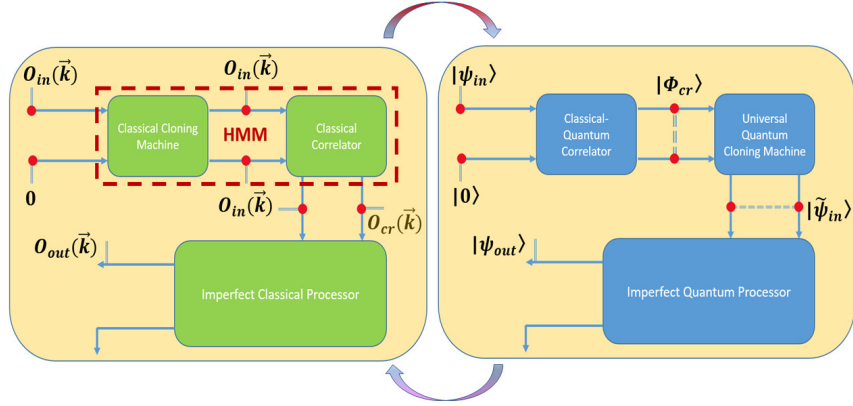
Figure 6.4: The ACI technique (left) using classical correlations is mapped to quantum picture (right). The feedback between classical (left) and quantum (right) pictures may lead to advanced hybrid classical-quantum information processing that optimally employs correlations for the best practical performance (see text).

with enhanced superresolution, respectively, while the imperfect classical processor corresponds to an imperfect imaging system. The steps for cloning and generation of correlations (see dashed rectangle) are performed by using a hyperbolic metamaterial (HMM)[10, 11] in the classical picture.

The classical picture can be mapped to the quantum picture (panel on right in figure 6.4). In the quantum picture, first, a correlated state $|\phi_{cr}\rangle$ is generated from the input state $|\psi_{in}\rangle$, which is next sent to universal quantum cloning machine (Buzek-Hillery) [45] to generate approximate copies in a new correlated state $|\tilde{\psi}_{in}\rangle$. It is this state which is fed into imperfect quantum processor to obtain the desired output state $|\psi_{out}\rangle$ with higher fidelity than the otherwise possible with $|\psi_{in}\rangle \otimes |0\rangle$ alone (i.e., with no correlations and copies) [46, 47].

Suggested by the classical problem [1, 5, 10, 11, 12, 48, 49], where the classical correlations improve the fidelity of a linear system in the presence of noise and loss of information, the idea in the classical domain can be translated to purely quantum or hybrid classical-quantum systems to improve the fidelity of imperfect quantum processes. The classical picture may guide toward a hybrid photonic classical-quantum processing, which may in turn enable the modification of the original classical system for the best possible performance. After multiple iterations of feedback an efficient hybrid information processing [50, 51, 52] may be possible by bringing together the best of two worlds, quantum and classical, on a common platform.

6.4 Conclusion

In conclusion, we provided a brief summary of ACI and discussed its potential implementations and extensions with three different systems involving imaging through scattering and random media, THz-TDS, and quantum computing. The three research directions have commonalities with the system conceptualized shown in figure 6.1 can potentially benefit from the implementation of ACI. Of course, possible future extensions of ACI should not be limited with these three systems presented here. We believe that the analysis presented here is only a glimpse from the tip of an iceberg. The process of implementation of ACI can be diversified to cover many other applications of fundamental and practical interest.

References

[1] Mehdi Sadatgol, Şahin K Özdemir, Lan Yang, and Durdu Ö Güney. Plasmon injection to compensate and control losses in negative index metamaterials. *Phys. Rev. Lett.*, 115(3):035502, 2015.

[2] Costas M Soukoulis and Martin Wegener. Optical metamaterials—more bulky and less lossy. *Science*, 330(6011):1633–1634, 2010.

[3] Mark I Stockman. Criterion for negative refraction with low optical losses from a fundamental principle of causality. *Phys. Rev. Lett.*, 98(17):177404, 2007.

[4] Sudhakar Prasad. Implications of light amplification for astronomical imaging. *J. Opt. Soc. Am. A*, 11(11):2799–2803, 1994.

[5] Wyatt Adams, Mehdi Sadatgol, Xu Zhang, and Durdu Ö Güney. Bringing the 'perfect lens' into focus by near-perfect compensation of losses without gain media. *New J. Phys.*, 18(12):125004, dec 2016.

[6] Wyatt Adams, Anindya Ghoshroy, and Durdu Ö Güney. Plasmonic superlens

image reconstruction using intensity data and equivalence to structured light illumination for compensation of losses. *J. Opt. Soc. Am. B*, 34(10):2161–2168, 2017.

[7] Xu Zhang, Wyatt Adams, Mehdi Sadatgol, and Durdu Ö Güney. Enhancing the resolution of hyperlens by the compensation of losses without gain media. *Prog. Electromagn. Res. C*, 70(1):2161–2168, 2016.

[8] Xu Zhang, Wyatt Adams, Mehdi Sadatgol, and Durdu Ö Güney. Analytical description of inverse filter emulating the plasmon injection loss compensation scheme and implementation for ultrahigh-resolution hyperlens. *J. Opt. Soc. Am. B*, 34(6):1310–1318, Jun 2017.

[9] Anindya Ghoshroy, Wyatt Adams, Xu Zhang, and Durdu Ö Güney. Active plasmon injection scheme for subdiffraction imaging with imperfect negative index flat lens. *J. Opt. Soc. Am. B*, 34(7):1478–1488, 2017.

[10] Anindya Ghoshroy, Wyatt Adams, Xu Zhang, and Durdu Ö Güney. Hyperbolic metamaterial as a tunable near-field spatial filter to implement active plasmon-injection loss compensation. *Phys. Rev. Applied*, 10(2):024018, 2018.

[11] Anindya Ghoshroy, Wyatt Adams, Xu Zhang, and Durdu Ö Güney. Enhanced superlens imaging with loss-compensating hyperbolic near-field spatial filter. *Opt. Lett.*, 43(8):1810–1813, 2018.

[12] Wyatt Adams, Anindya Ghoshroy, and Durdu Ö Güney. Plasmonic superlens

imaging enhanced by incoherent active convolved illumination. *ACS Photonics*, 5(4):1294–1302, 2018.

[13] Xiao-Feng Qian, A Nick Vamivakas, and Joseph H Eberly. Emerging connections: classical and quantum optics. *Optics and Photonics News*, 28(10):34–41, 2017.

[14] Anindya Ghoshroy, Wyatt Adams, and Durdu O Guney. Theory of coherent active convolved illumination for superresolution enhancement. *arXiv preprint arXiv:1905.12114*, 2019.

[15] Larry C Andrews and Ronald L Phillips. *Laser beam propagation through random media*, volume 152. SPIE press Bellingham, WA, 2005.

[16] RL Fante. Wave propagation in random media: A systems approach. *Progress in Optics*, 31:341, 1993.

[17] Akira Ishimaru. *Wave propagation and scattering in random media*, volume 2. Academic press New York, 1978.

[18] Norman S Kopeika and Dan Arbel. Imaging through the atmosphere: an overview. In *Optical Pulse and Beam Propagation*, volume 3609, pages 78–89. International Society for Optics and Photonics, 1999.

[19] I Dror and NS Kopeika. Experimental comparison of turbulence modulation transfer function and aerosol modulation transfer function through the open atmosphere. *J. Opt. Soc. Am. A*, 12(5):970–980, 1995.

[20] B Ben Dor, AD Devir, G Shaviv, P Bruscaglioni, P Donelli, and A Ismaelli. Atmospheric scattering effect on spatial resolution of imaging systems. *J. Opt. Soc. Am. A*, 14(6):1329–1337, 1997.

[21] Luc R Bissonnette. Imaging through fog and rain. *Opt. Eng.*, 31(5):1045–1053, 1992.

[22] Mohamed E Hanafy, Michael C Roggemann, and Durdu O Guney. Detailed effects of scattering and absorption by haze and aerosols in the atmosphere on the average point spread function of an imaging system. *J. Opt. Soc. Am. A*, 31(6):1312–1319, 2014.

[23] Mohamed E Hanafy, Michael C Roggemann, and Durdu O Guney. Estimating the image spectrum signal-to-noise ratio for imaging through scattering media. *Opt. Eng.*, 54(1):013102, 2015.

[24] Mohamed E Hanafy, Michael C Roggemann, and Durdu O Guney. Reconstruction of images degraded by aerosol scattering and measurement noise. *Opt. Eng.*, 54(3):033101, 2015.

[25] Binbin B Hu and Martin C Nuss. Imaging with terahertz waves. *Opt. Lett.*, 20(16):1716–1718, 1995.

[26] Albert Redo-Sanchez, Norman Laman, Brian Schulkin, and Thomas Tongue. Review of terahertz technology readiness assessment and applications. *J. Infrared Millim. Terahertz Waves*, 34(9):500–518, 2013.

[27] Juraj Sibik and J Axel Zeitler. Direct measurement of molecular mobility and crystallisation of amorphous pharmaceuticals using terahertz spectroscopy. *Adv. Drug Deliv. Rev.*, 100:147–157, 2016.

[28] Shuting Fan, Yuezhi He, Benjamin S Ung, and Emma Pickwell-MacPherson. The growth of biomedical terahertz research. *J. Phys. D*, 47(37):374009, 2014.

[29] Jianyuan Qin, Yibin Ying, and Lijuan Xie. The detection of agricultural products and food using terahertz spectroscopy: a review. *Appl. Spectrosc. Rev.*, 48(6):439–457, 2013.

[30] Hai-Bo Liu, Hua Zhong, Nicholas Karpowicz, Yunqing Chen, and Xi Cheng Zhang. Terahertz spectroscopy and imaging for defense and security applications. *Proc. IEEE*, 95(8):1514–1527, 2007.

[31] J Bianca Jackson, John Bowen, Gillian Walker, Julien Labaune, Gerard Mourou, Michel Menu, and Kaori Fukunaga. A survey of terahertz applications in cultural heritage conservation science. *IEEE Trans. Terahertz Sci. Technol.*, 1(1):220–231, 2011.

[32] Byounghwak Lee, Ali Mousavian, Michael J Paul, Zachary J Thompson, Andrew D Stickel, Dalton R McCuen, Eui Yun Jang, Yong Hyup Kim, Jisoo Kyoung, Dai-Sik Kim, et al. Anisotropic high-field terahertz response of free-standing carbon nanotubes. *Appl. Phys. Lett.*, 108(24):241111, 2016.

[33] Nikolay V Petrov, Maxim S Kulya, Anton N Tsypkin, Victor G Bespalov, and

Andrei Gorodetsky. Application of terahertz pulse time-domain holography for phase imaging. *IEEE Trans. Terahertz Sci. Technol.*, 6(3):464–472, 2016.

[34] Hichem Guerboukha, Kathirvel Nallappan, and Maksim Skorobogatiy. Toward real-time terahertz imaging. *Adv. Opt. Photonics*, 10(4):843–938, 2018.

[35] Matthew C. Beard, Gordon M. Turner, and Charles A. Schmuttenmaer. Terahertz spectroscopy. *J. Phys. Chem. B*, 106(29):7146–7159, 2002.

[36] Martin Van Exter and Daniel R Grischkowsky. Characterization of an optoelectronic terahertz beam system. *IEEE Trans. Microw. Theory Tech.*, 38(11):1684–1691, 1990.

[37] M Walther, B Fischer, M Schall, H Helm, and P Uhd Jepsen. Far-infrared vibrational spectra of all-trans, 9-cis and 13-cis retinal measured by thz time-domain spectroscopy. *Chem. Phys. Lett.*, 332(3-4):389–395, 2000.

[38] Peter Uhd Jepsen and Bernd M Fischer. Dynamic range in terahertz time-domain transmission and reflection spectroscopy. *Opt. Lett.*, 30(1):29–31, 2005.

[39] V. A. Alekseev, M. R. Zaripov, and Sitnikova E. A. Efficiency of a laser radiation source with coherent pulse combining. *J. Opt. Technol.*, 86(4):204–208, 2019.

[40] Lionel Duvillaret, Frederic Garet, and J-L Coutaz. A reliable method for extraction of material parameters in terahertz time-domain spectroscopy. *IEEE J. Sel. Top. Quantum Electron.*, 2(3):739–746, 1996.

[41] Lionel Duvillaret, Frédéric Garet, and Jean-Louis Coutaz. Influence of noise on the characterization of materials by terahertz time-domain spectroscopy. *J. Opt. Soc. Am. B*, 17(3):452–461, 2000.

[42] P Uhd Jepsen and SR Keiding. Radiation patterns from lens-coupled terahertz antennas. *Opt. Lett.*, 20(8):807–809, 1995.

[43] ER Brown. Fundamentals of terrestrial millimeter-wave and thz remote sensing. *Int. J. High Speed Electron. Syst.*, 13(04):995–1097, 2003.

[44] Kiarash Ahi and Mehdi Anwar. Developing terahertz imaging equation and enhancement of the resolution of terahertz images using deconvolution. In *Terahertz Physics, Devices, and Systems X: Advanced Applications in Industry and Defense*, volume 9856, page 98560N. International Society for Optics and Photonics, 2016.

[45] V. Buzek and M. Hillery. Quantum copying: beyond the no-cloning theorem. *Phys. Rev. A*, 54:1844–1852, 1996.

[46] A. Gueddana, P. Gholami, and V. Lakshminarayanan. Can a universal quantum cloner be used to design an experimentally feasible near-deterministic cnot gate? *Quantum Inf. Process.*, 18:221, 2019.

[47] Amor Gueddana and Vasudevan Lakshminarayanan. Toward the universal quantum cloner limit for designing compact photonic cnot gate. *arXiv preprint arXiv:1906.06547*, 2019.

[48] Jan Becker, Ronny Forster, and Rainer Heintzmann. Better than a lens – a novel concept to break the snr limit, given by fermat's principle. *arXiv preprint arXiv:1811.08267*, 2018.

[49] E. A. Ingerman, R. A. London, R. Heintzmann, and M. G. L. Gustafsson. Signal, noise and resolution in linear and nonlinear structured-illumination microscopy. *J. Microscopy*, 273:3–25, 2019.

[50] V. Dunjko, Y. Ge, and J. I. Cirac. Computational speedups using small quantum devices. *Phys. Rev. Lett.*, 121:250501, 2018.

[51] J.-S. Lee, J. Bang, S. Hong, C. Lee, K. H. Seol, J. Lee, and K.-G. Lee. Experimental demonstration of quantum learning speedup with classical input data. *Phys. Rev. A*, 99:012313, 2019.

[52] C. Kokail, C. Maier, R. van Bijnen, T. Brydges, M. K. Joshi, P. Jurcevic, C. A. Muschik, P. Silvi, R. Blatt, C. F. Roos, and P. Zoller. Self-verifying variational quantum simulation of lattice models. *Nature*, 569:355–360, 2019.

Appendix A

Letters of Permission

A.1 Permission to reprint the article from *The Optical Society of America*

Michigan Tech   **Anindya Ghoshroy**

Permission for reprinting OSA papers in dissertation
2 messages

Anindya Ghoshroy   Tue, Oct 6, 2020 at 11:37 AM
To: pubscopyright <copyright@osa.org>

Hello,

I sent an email requesting permission to reproduce articles published in OSA journals, but since I haven't received a response yet, I am sending a reminder.

I am a PhD student at Michigan Technological University, and I published the following papers in Optics Materials Express and Journal of the Optical Society of America B , respectively.

[1] Anindya Ghoshroy, Şahin K. Özdemir, and Durdu Ö. Güney, "Loss compensation in metamaterials and plasmonics with virtual gain," Opt. Mater. Express 10, 1862 (2020)

[2] Anindya Ghoshroy, Wyatt Adams, and Durdu Ö. Güney, "Theory of coherent active convolved illumination for superresolution enhancement," J. Opt. Soc. Am. B 37, 2452 (2020)

Could I have permission to reproduce the introduction section of [1] and the full article of [2] in the main body of my dissertation?

Sincerely,
Anindya Ghoshroy

--
PhD Student
Electrical and Computer Engineering Department

---

pubscopyright <copyright@osa.org>   Wed, Oct 7, 2020 at 12:16 PM
To: Anindya Ghoshroy <aghoshro@mtu.edu>, pubscopyright <copyright@osa.org>

Dear Anindya Ghoshroy,

Thank you for contacting The Optical Society (OSA).

For the use of material from Anindya Ghoshroy, Şahin K. Özdemir, and Durdu Ö. Güney, "Loss compensation in metamaterials and plasmonics with virtual gain [Invited]," Opt. Mater. Express 10, 1862-1880 (2020):

Because you are the author of the source paper from which you wish to reproduce material, OSA considers your requested use of its copyrighted materials to be permissible within the author rights granted in the Copyright Transfer Agreement submitted by the requester on acceptance for publication of his/her manuscript. It is requested that a complete citation of the original material be included in any publication. This permission assumes that the material was not reproduced from another source when published in the original publication.

If the entire article is being included, it is permissible to use the **version of record**.

For the use of material from Anindya Ghoshroy, Wyatt Adams, and Durdu Ö. Güney, "Theory of coherent active convolved illumination for superresolution enhancement," J. Opt. Soc. Am. B 37, 2452-2463 (2020):

Because you are the author of the source paper from which you wish to reproduce material, OSA considers your requested use of its copyrighted materials to be permissible within the author rights granted in the Copyright Transfer Agreement submitted by the requester on acceptance for publication of his/her manuscript. If the entire article is being included, it is requested that the **Author Accepted Manuscript** (or preprint) version be the version included within the thesis and that a complete citation of the original material be included in any publication. This permission assumes that the material was not reproduced from another source when published in the original publication.

The **Author Accepted Manuscript** version is the preprint version of the article that was accepted for publication but not yet prepared and/or formatted by The Optical Society or its vendors.

While your publisher should be able to provide additional guidance, OSA prefers the below citation formats:

For citations in figure captions:

[Reprinted/Adapted] with permission from [ref #] © The Optical Society. (Please include the full citation in your reference list)

For images without captions:

Journal Vol. #, first page (year published) An example: Opt. Express 19, 2720 (2011)

Please let me know if you have any questions.

Kind Regards,

██████████████

██████████████

October 7, 2020

Authorized Agent, The Optical Society

The Optical Society (OSA)

2010 Massachusetts Ave., NW

Washington, DC 20036 USA

www.osa.org

Reflecting a Century of Innovation

[Quoted text hidden]

A.2 Permission to reprint the article from *The Optical Society of America*

Michigan Tech

Anindya Ghoshroy <aghoshro@mtu.edu>

Permission for reprinting OSA papers in dissertation

2 messages

Anindya Ghoshroy   Fri, Jan 24, 2020 at 10:03 AM
To: copyright@osa.org

Hello,

I am a PhD student at Michigan Technological University, and I published the following papers in Journal of the Optical Society of America B and Optics Letters, respectively.

Anindya Ghoshroy, Wyatt Adams, Xu Zhang, and Durdu Ö. Güney, "Active plasmon injection scheme for subdiffraction imaging with imperfect negative index flat lens," J. Opt. Soc. Am. B 34, 1478-1488 (2017)

Anindya Ghoshroy, Wyatt Adams, Xu Zhang, and Durdu Ö. Güney, "Enhanced superlens imaging with loss-compensating hyperbolic near-field spatial filter," Opt. Lett. 43, 1810-1813 (2018)

Could I have permission to reprint the above papers in the main body of my dissertation?

Sincerely,
Anindya
--
PhD Student
Electrical and Computer Engineering Department
822 EERC, Michigan Tech. University

pubscopyright <copyright@osa.org>   Fri, Jan 24, 2020 at 3:18 PM
To: Anindya Ghoshroy   , pubscopyright <copyright@osa.org>

Dear Anindya Ghoshroy,

Thank you for contacting The Optical Society.

For the use of material from [1] Anindya Ghoshroy, Wyatt Adams, Xu Zhang, and Durdu Ö. Güney, "Active plasmon injection scheme for subdiffraction imaging with imperfect negative index flat lens," J. Opt. Soc. Am. B 34, 1478-1488 (2017) and [2] Anindya Ghoshroy, Wyatt Adams, Xu Zhang, and Durdu Ö. Güney, "Enhanced superlens imaging with loss-compensating hyperbolic near-field spatial filter," Opt. Lett. 43, 1810-1813 (2018):

Because you are the author of the source paper from which you wish to reproduce material, OSA considers your requested use of its copyrighted materials to be permissible within the author rights granted in the Copyright Transfer Agreement submitted by the requester on acceptance for publication of his/her manuscript. If the entire article is being included, it is requested that the **Author Accepted Manuscript** (or preprint) version be the version included within the thesis and that a complete citation of the original material be included in any publication. This permission assumes that the material was not reproduced from another source when published in the original publication.

The **Author Accepted Manuscript** version is the preprint version of the article that was accepted for publication but not yet prepared and/or formatted by The Optical Society or its vendors.

While your publisher should be able to provide additional guidance, OSA prefers the below citation formats:

For citations in figure captions:

[Reprinted/Adapted] with permission from [ref #] © The Optical Society. (Please include the full citation in your reference list)

For images without captions:

Journal Vol. #, first page (year published) An example: Opt. Lett. 43, 1810 (2018)

Please let me know if you have any questions.

Kind Regards,

████████████

████████████

January 24, 2020

Authorized Agent, The Optical Society

The Optical Society (OSA)

2010 Massachusetts Ave., NW

Washington, DC 20036 USA

www.osa.org

Reflecting a Century of Innovation

[Quoted text hidden]

215

A.3 Permission to reprint the article from *American Physical Society*

Michigan Tech   **Anindya Ghoshroy** <▓▓▓▓▓▓▓▓▓>

SciPris: Thank you for your APS Rights and Permissions Order RNP/20/JAN/022191
1 message

SciPris <no-reply@aptaracorp.com>   Fri, Jan 24, 2020 at 10:26 AM
To: ▓▓▓▓▓▓▓

Dear Anindya Ghoshroy,

Thank you for your order with SciPris.

Your copyright permission for the American Physical Society article "Hyperbolic Metamaterial as a Tunable Near-Field Spatial Filter to Implement Active Plasmon-Injection Loss Compensation" with order identification number RNP/20/JAN/022191 has been approved.

To download your license and review the terms and conditions of reuse, please **Click here**.

Please contact scipris-help@aptaracorp.com for further information, questions, or concerns.

Thank you,
The SciPris Team on behalf of the American Physical Society

📄 **License_RNP_20_JAN_022191.pdf**
47K

American Physical Society
Reuse and Permissions License

24-Jan-2020

This license agreement between the American Physical Society ("APS") and Anindya Ghoshroy ("You") consists of your license details and the terms and conditions provided by the American Physical Society and SciPris.

Licensed Content Information

License Number:	
License date:	24-Jan-2020
DOI:	10.1103/PhysRevApplied.10.024018
Title:	Hyperbolic Metamaterial as a Tunable Near-Field Spatial Filter to Implement Active Plasmon-Injection Loss Compensation
Author:	Anindya Ghoshroy et al.
Publication:	Physical Review Applied
Publisher:	American Physical Society
Cost:	USD $ 0.00

Request Details

Does your reuse require significant modifications: No

Specify intended distribution locations:	United States
Reuse Category:	Reuse in a thesis/dissertation
Requestor Type:	Author of requested content
Items for Reuse:	Whole Article
Format for Reuse:	Electronic

Information about New Publication:

University/Publisher:	Michigan Technological University/ProQuest
Title of dissertation/thesis:	Superresolution enhancement with selective spectral amplification and correlations
Author(s):	Anindya Ghoshroy
Expected completion date:	Apr. 2020

License Requestor Information

Name:	Anindya Ghoshroy
Affiliation:	Individual
Email Id:	
Country:	United States

APS physics American Physical Society
Reuse and Permissions License

TERMS AND CONDITIONS

The American Physical Society (APS) is pleased to grant the Requestor of this license a non-exclusive, non-transferable permission, limited to Electronic format, provided all criteria outlined below are followed.

1. You must also obtain permission from at least one of the lead authors for each separate work, if you haven't done so already. The author's name and affiliation can be found on the first page of the published Article.

2. For electronic format permissions, Requestor agrees to provide a hyperlink from the reprinted APS material using the source material's DOI on the web page where the work appears. The hyperlink should use the standard DOI resolution URL, http://dx.doi.org/{DOI}. The hyperlink may be embedded in the copyright credit line.

3. For print format permissions, Requestor agrees to print the required copyright credit line on the first page where the material appears: "Reprinted (abstract/excerpt/figure) with permission from [(FULL REFERENCE CITATION) as follows: Author's Names, APS Journal Title, Volume Number, Page Number and Year of Publication.] Copyright (YEAR) by the American Physical Society."

4. Permission granted in this license is for a one-time use and does not include permission for any future editions, updates, databases, formats or other matters. Permission must be sought for any additional use.

5. Use of the material does not and must not imply any endorsement by APS.

6. APS does not imply, purport or intend to grant permission to reuse materials to which it does not hold copyright. It is the requestor's sole responsibility to ensure the licensed material is original to APS and does not contain the copyright of another entity, and that the copyright notice of the figure, photograph, cover or table does not indicate it was reprinted by APS with permission from another source.

7. The permission granted herein is personal to the Requestor for the use specified and is not transferable or assignable without express written permission of APS. This license may not be amended except in writing by APS.

8. You may not alter, edit or modify the material in any manner.

9. You may translate the materials only when translation rights have been granted.

10. APS is not responsible for any errors or omissions due to translation.

11. You may not use the material for promotional, sales, advertising or marketing purposes.

12. The foregoing license shall not take effect unless and until APS or its agent, Aptara, receives payment in full in accordance with Aptara Billing and Payment Terms and Conditions, which are incorporated herein by reference.

13. Should the terms of this license be violated at any time, APS or Aptara may revoke the license with no refund to you and seek relief to the fullest extent of the laws of the USA. Official written notice will be made using the contact information provided with the permission request. Failure to receive such notice will not nullify revocation of the permission.

14. APS reserves all rights not specifically granted herein.

15. This document, including the Aptara Billing and Payment Terms and Conditions, shall be the entire agreement between the parties relating to the subject matter hereof.

A.4 Permission to reprint the article from *Society of Photo-Optical Instrumentation Engineers*

Michigan Tech   **Anindya Ghoshroy** ▬▬▬▬▬▬▬▬

Permission for reprinting SPIE paper in dissertation

2 messages

Anindya Ghoshroy ▬▬▬▬▬▬▬▬   Mon, Jan 27, 2020 at 8:31 AM
To: reprint_permission@spie.org

Hello,

I am a PhD student at Michigan Technological University, and I published the following conference paper for the event SPIE Nanoscience + Engineering held in September 2019 at San Diego, California.

D.Ö Güney, W. Adams, and A. Ghoshroy, "Super-resolution enhancement with active convolved illumination and correlations." In *Active Photonic Platforms XI* September 2019 (Vol. 11081, p. 1108128). International Society for Optics and Photonics.

Could I have permission to reprint the above paper in the main body of my dissertation?

Sincerely,
Anindya
--
PhD Student
Electrical and Computer Engineering Department
▬▬▬▬▬▬▬▬▬▬▬▬▬▬

▬▬▬▬▬▬▬@spie.org>   Mon, Jan 27, 2020 at 12:27 PM
To: Anindya Ghoshroy ▬▬▬▬@mtu.edu>

Dear Anindya,

Thank you for seeking permission from SPIE to reprint material from our publications. SPIE shares the copyright with you, so as author you retain the right to reproduce your paper in part or in whole.

Publisher's permission is hereby granted under the following conditions:

        (1) the material to be used has appeared in our publication without credit or acknowledgment to another source; and

        (2) you credit the original SPIE publication. Include the authors' names, title of paper, volume title, SPIE volume number, and year of publication in your credit statement.

Best wishes on your dissertation! Please let me know if I may be of any further assistance.

Best,

▬▬▬▬▬▬

Editorial Assistant, Publications

SPIE

@spie.org

SPIE is the international society for optics and photonics

http://SPIE.org

[Quoted text hidden]

Appendix B

MATLAB code

B.1   Generate figure 5.8

```matlab
%%%%%%%%%%%%%%%%%%%%%%%%%%%%%%%%%%%%%%%%%%%%%%%%%%%%%%%%%%%%%%%%%%%%
%%%%%%
% Program name: Simulation of near-field superresolution enhancement
 with
% Active Convolved Illumination.
% Author: Anindya Ghoshroy
% Creation Date: 05/26/2020
% Most recent update: 08/11/2020
% Function: Simulates the propagation of a magnetic field distribution
% containing four subwavelength Gaussian features though a silver
 plasmonic
% lens at wavelength 365nm. Simulation is conducted with and without
 ACI in
% the presense of signal-dependent shot noise. Final reconstructed
 images after
% deconvolution are generated for the systems with and woithout ACI.
%%%%%%%%%%%%%%%%%%%%%%%%%%%%%%%%%%%%%%%%%%%%%%%%%%%%%%%%%%%%%%%%%%%%
%%%%%%
% IMPORTANT NOTE: ALL units are in SI system an spatial dimentions are
 in
% micrometers.
%%%%%%%%%%%%%%%%%%%%%%%%%%%%%%%%%%%%%%%%%%%%%%%%%%%%%%%%%%%%%%%%%%%%
%%%%%%
% Recent Comments : Added Weiner filter in final reconstruction step
 as
% requested by referee.
%%%%%%%%%%%%%%%%%%%%%%%%%%%%%%%%%%%%%%%%%%%%%%%%%%%%%%%%%%%%%%%%%%%%
%%%%%%
close all
clear all
clc
format long
CRIMSON               = 1/255*[220,20,60];
BLACK                 = 1/255*[0,0,0];
DEEP_PINK             = 1/255*[255,20,147];
HOT_PINK              = 1/255*[255,105,180];
MEDIUM_SLATE_BLUE     = 1/255*[123,104,238];
GREEN                 = 1/255*[0, 255, 114];
MEDIUM_SPRING_GREEN   = 1/255*[0,250,154];
OLIVE                 = 1/255*[128,128,0];
TEAL                  = 1/255*[0,128,128];
DODGER_BLUE           = 1/255*[30,144,255];
DARK_SLATE_GREY       = 1/255*[47,79,79];
PURPLE                = 1/255*[128,0,128];
ORANGE_RED            = 1/255*[255,69,0];
ORANGE                = 1/255*[124,255,124];
DARK_VIOLET           = 1/255*[148,0,211];
BLUE                  = 1/255*[0,0,255];
GOLD                  = 1/255*[255,215,0];
%%%%%%%%%%%%%%%%%%%%%%%%%%%%%%%%%%%%%%%%%%%%%%%%%%%%%%%%%%%%%%%%%%%%
%%%%%%
c = 2.99792458e8;            % Speed of light in free space [m]
```

1

```matlab
Lda = 0.3657*10^-6;          % Wavelength [m]
freq = c /Lda;               % Frequency  [Hz]
k0 = 2*pi*freq/c;            % Free space wavenumber [1/m]
Limit = (Lda*10^6)*80;       % Length of image and object planes [um]
y_step = 0.005;              % Spatial discretization [um]
y = -Limit/2:y_step:Limit/2;
Obj_sep = Lda/20;            % Peak-to-peak separation of objects
y = y * 10^-6;
%%%%%%%%%%%%%%%%%%%%%%%%%%%%%%%%%%%%%%%%%%%%%%%%%%%%%%%%%%%%%%%%%%%%%
%%%%%
% OBJECT FIELD DISTRIBUTION [A/m]
point_source_y = Lda/12;
sigma = point_source_y/12;
FWHM = 2.35482*sigma;
Amplitude = 1;
%4 Aperture object illuminated with a normally incident TM-plane wave.
Object_field =  Amplitude*exp(-((y -  Obj_sep/2).^2)/(2*sigma^2)) +
 Amplitude*exp(-((y+Obj_sep/2).^2)/(2*sigma^2))+Amplitude*exp(-((y -
 3*Obj_sep/2).^2)/(2*sigma^2)) + Amplitude*exp(-((y+3*Obj_sep/2).^2)/
(2*sigma^2));
%%%%%%%%%%%%%%%%%%%%%%%%%%%%%%%%%%%%%%%%%%%%%%%%%%%%%%%%%%%%%%%%%%%%%
%%%%%
% Discretized Fourier transform setup
sampling_space = 1;
sampling_k = 2*pi/sampling_space;
L = length(Object_field);
N_fft = 1*(L);
M=L;
ky_sam = pi/(max(y)*1e-6);
ky_step = 0.5*pi/(y_step*1e-6);                % Delta k_y [1/m]
ky = (2*(0:(N_fft)-1)/N_fft)*(ky_step/k0);     % [1/m]
%%%%%%%%%%%%%%%%%%%%%%%%%%%%%%%%%%%%%%%%%%%%%%%%%%%%%%%%%%%%%%%%%%%%%
%%%%%
% Fourier transform of Object
FFT_Object_field = fft(Object_field, N_fft);  % [A]
%%%%%%%%%%%%%%%%%%%%%%%%%%%%%%%%%%%%%%%%%%%%%%%%%%%%%%%%%%%%%%%%%%%%%
%%%%%
% Transmission coefficient of a 50nm Ag film at 365nm [Dimensionless]
T_dielectric2    = 50*10^-9;
d = 50*10^-9;
T_dielectric1    = T_dielectric2/2;
T_dielectric3    = T_dielectric2/2;
eps_dielectric1  = 2.2752;
eps_dielectric2  = -1.8752 - 1i*0.5947;
eps_dielectric3  = 2.2752;
kx1 = sqrt(eps_dielectric1 - ky.^2).*k0;
kx2 = 1i*sqrt(ky.^2 - eps_dielectric2).*k0;
kx3 = sqrt(eps_dielectric3 - ky.^2).*k0;
r12 = (kx1./eps_dielectric1 - kx2./eps_dielectric2)./(kx1./
eps_dielectric1 + kx2./eps_dielectric2);
r23 = (kx2./eps_dielectric2 - kx3./eps_dielectric3)./(kx2./
eps_dielectric2 + kx3./eps_dielectric3);
t12 = 1 + r12;
t23 = 1 + r23;
```

```matlab
%%%%%%%%%%%%%%%%%%%%%%%%%%%%%%%%%%%%%%%%%%%%%%%%%%%%%%%%%%%%%%%%%%%
%%%%%
% Passive transfer function [Dimensionless]
TF  = (t12.*t23)./(exp(-1i*kx2*d) + r12.*r23.*
 exp(1i*kx2*T_dielectric2)).*exp(1i*kx1*T_dielectric1).*exp(1i*kx1*T_dielectric3);
% ACI filter finction [Dimensionless]
Aux = 1 + 100*exp(-((ky -  7).^2)/(1)) + 10000*exp(-((ky -  8.8).^2)/
(1));
%%%%%%%%%%%%%%%%%%%%%%%%%%%%%%%%%%%%%%%%%%%%%%%%%%%%%%%%%%%%%%%%%%%
%%%%%
% Calculate passive and active image spectrum
FFT_Output_field          = FFT_Object_field.*TF;
FFT_Active_Output_field   = FFT_Object_field.*TF.*Aux;
Output_field              = fftshift(ifft(FFT_Output_field));
Active_Output_field       = fftshift(ifft(FFT_Active_Output_field));
%%%%%%%%%%%%%%%%%%%%%%%%%%%%%%%%%%%%%%%%%%%%%%%%%%%%%%%%%%%%%%%%%%%
%%%%%
% Create noisy fields in the spatial domain
[Passive_Noise_SD, Passive_Noise_SI, Passive_Noise_Total] =
 noiseGen(abs(Output_field),0.001);
[Active_Noise_SD,  Active_Noise_SI,  Active_Noise_Total]  =
 noiseGen(abs(Active_Output_field ),0.001);
% Build noisy images [Only signal-dependent noise is used]
Output_field_noisy                = (abs(Output_field)         +
 Passive_Noise_SD).*exp(1j*angle(Output_field));
Active_Output_field_noisy         = (abs(Active_Output_field) +
 Active_Noise_SD ).*exp(1j*angle(Active_Output_field));
%%%%%%%%%%%%%%%%%%%%%%%%%%%%%%%%%%%%%%%%%%%%%%%%%%%%%%%%%%%%%%%%%%%
%%%%%
FFT_Output_field_noisy            = fft(Output_field_noisy);
FFT_Active_Output_field_noisy     = fft(Active_Output_field_noisy);
FFT_Passive_Noise_SD              = fft(Passive_Noise_SD);
FFT_Active_Noise_SD               = fft(Active_Noise_SD);
FFT_sigma_q_Passive               = FFT_Active_Noise_SD.*0 + sqrt((1/
M)*sum((abs(FFT_Output_field)*0.001).^2));
FFT_sigma_q_Active                = FFT_Active_Noise_SD.*0 + sqrt((1/
M)*sum((abs(FFT_Active_Output_field)*0.001).^2));
%%%%%%%%%%%%%%%%%%%%%%%%%%%%%%%%%%%%%%%%%%%%%%%%%%%%%%%%%%%%%%%%%%%
%%%%%
% Reconstruction
% Passive Weiner Filter
SNR = (FFT_sigma_q_Passive./abs(FFT_Output_field)).^2;
WF                             = 1./(1+SNR);
FFT_Output_field_noisy_rec        = WF.*FFT_Output_field_noisy./(TF);
FFT_Active_Output_field_noisy_rec = FFT_Active_Output_field_noisy./
(TF.*Aux);
%%%%%%%%%%%%%%%%%%%%%%%%%%%%%%%%%%%%%%%%%%%%%%%%%%%%%%%%%%%%%%%%%%%
%%%%%
% Spectral cut-off
delta_k = ky(3)- ky(2);
Cut_off = 11;
ky_trunc1   = 0:delta_k:Cut_off;
FFT_Active_Output_field_noisy_rec_abs   = interp1(ky,
 abs(FFT_Active_Output_field_noisy_rec),    ky_trunc1, 'pchip');
```

3

226

```matlab
FFT_Active_Output_field_noisy_rec_phase = interp1(ky,
 angle(FFT_Active_Output_field_noisy_rec),  ky_trunc1, 'pchip');
FFT_Output_field_noisy_rec_trunc        = FFT_Output_field_noisy_rec;
%FFT_Output_field_noisy_rec_trunc        =
 FFT_Output_field_noisy_rec_abs.*exp(1j*FFT_Output_field_noisy_rec_phase);
FFT_Active_Output_field_noisy_rec_trunc =
 FFT_Active_Output_field_noisy_rec_abs.*exp(1j*FFT_Active_Output_field_noisy_rec_p
%%%%%%%%%%%%%%%%%%%%%%%%%%%%%%%%%%%%%%%%%%%%%%%%%%%%%%%%%%%%%%%%%%%%
%%%%%
Output_field_noisy_rec_trunc            =
 fftshift(ifft(FFT_Output_field_noisy_rec_trunc,          N_fft));
Active_Output_field_noisy_rec_trunc     =
 fftshift(ifft(FFT_Active_Output_field_noisy_rec_trunc,  N_fft));
%%%%%%%%%%%%%%%%%%%%%%%%%%%%%%%%%%%%%%%%%%%%%%%%%%%%%%%%%%%%%%%%%%%%
%%%%%
% Figure 8 published in
% A. Ghoshroy, W. Adams, and D. Ö. Güney, "Theory of coherent active
 convolved
% illumination for superresolution enhancement," J. Opt. Soc. Am. B
 37,
% 2452 (2020).
%%%%%%%%%%%%%%%%%%%%%%%%%%%%%%%%%%%%%%%%%%%%%%%%%%%%%%%%%%%%%%%%%%%%
%%%%%
figure(1);
%subplot(2,1,1)
hold on;
plot(ky, abs(FFT_Object_field),                   'Color',  BLACK,
     'linewidth',   16);
plot(ky, abs(FFT_Output_field_noisy),             'Color',  GREEN,
     'linewidth',   16);
plot(ky, abs(FFT_Output_field_noisy_rec),         'Color',  GOLD ,
     'linewidth',   12) ;
plot(ky, abs(FFT_Active_Output_field_noisy),      'Color',
 DODGER_BLUE,      'linewidth',   8) ;
plot(ky, abs(FFT_Active_Output_field_noisy_rec), 'Color',  CRIMSON,
     'linewidth',   8) ;
grid off;
box on;
set(gca,'TickLabelInterpreter','latex')
set(gca, 'YScale','log');
set(gca, 'YMinorTick','off')
xlabel('$\mathbf{\zeta/
k_0}$','interpreter','latex','fontsize',27,'fontWeight','bold');
ylabel('$\mathbf{Magnitude
 (A)}$','interpreter','latex','fontsize',27,'fontWeight','bold');
set(gca,'fontsize',27,'fontWeight','bold','linewidth',2);
L = legend('$\mathbf{|O(\zeta)|}$','$\mathbf{|I_{n,P}(\zeta)|}$','$
\mathbf{|\tilde{O}_{n,P}(\zeta)|}$','$\mathbf{|I_{n,A}(\zeta)|}$','$
\mathbf{|\tilde{O}_{n,A}(\zeta)|}$ ','Location','southwest');
set(L,'Interpreter','latex')
axis([0 12 1e-14 30000]);
set(gca,'YTick',[1e-12 1e-8 1e-4 1e0 1e4]);
set(gca,'XTick', [0:2:12]);
```

4

227

```matlab
%save('test1.mat','Object_field','Active_Output_field_noisy_rec_trunc','Output_fie
% Previously obtained data from same code was saved and reopened here
 to build the figure as
% reqested by the referee.
Data_1          = open('test1.mat');
Data_2          = open('test.mat');

figure(2);
hold on;
plot(Data_1.y.*1000, (Data_1.Object_field),
                                                'Color',  BLACK,
  'linewidth',   12);
plot(Data_1.y.*1000, abs(Data_1.Output_field_noisy_rec_trunc),
  'Color',  GOLD,  'linewidth',   8);
plot(Data_1.y.*1000,
 abs(Data_1.Active_Output_field_noisy_rec_trunc), 'Color',  CRIMSON,
  'linewidth',   8);
plot(Data_2.y.*1000,
 abs(Data_2.Active_Output_field_noisy_rec_trunc), 'Color',
 MEDIUM_SPRING_GREEN,    'linewidth',   8);
box on;
grid off;
xlabel('$\mathbf{\xi
 (nm)}$','interpreter','latex','fontsize',27,'fontWeight','bold');
ylabel('$\mathbf{|H(\xi)| Am^{-1}}$
 ','interpreter','latex','fontsize',27,'fontWeight','bold');
L = legend('\boldmath{$|O(\xi)|$}','\boldmath{$|\tilde{O}_{n,P}
(\xi)|$}','\boldmath{$|\tilde{O}_{n,A}(\xi)| \ \Delta
 y=0.5$}\textbf{nm}','\boldmath{$|\tilde{O}_{n,A}(\xi)| \ \Delta
 y=5$}\textbf{nm}','Location','northwest');
set(L,'Interpreter','latex')
set(gca,'TickLabelInterpreter','latex')
set(gca,'fontsize',27,'fontWeight','bold','linewidth',2);
set(gca,'YMinorTick','off')
axis([-100 100 0 1.25]);
set(gca,'XTick', [-100:10:100]);
set(gca,'YTick', [0:0.25:1.25]);
```

5